ORNL/TM-12398/R1

ornl

OAK RIDGE NATIONAL LABORATORY

LOCKHEED MARTIN

# Update to Advanced Neutron Source Steady-State Thermal-Hydraulic Report

G. L. Yoder
J. J. Carbajo
D. G. Morris
W. R. Nelson



May 1996

Advanced Neutron Source

MANAGED AND OPERATED BY
LOCKHEED MARTIN ENERGY RESEARCH CORPORATION
FOR THE UNITED STATES
DEPARTMENT OF ENERGY

ORNL/TM-12398/R1

# UPDATE TO ADVANCED NEUTRON SOURCE STEADY-STATE THERMAL-HYDRAULIC REPORT

G. L. Yoder
J. J. Carbajo
D. G. Morris
W. R. Nelson

Completed: September 1995
Published: May 1996

Prepared by
OAK RIDGE NATIONAL LABORATORY
Oak Ridge, TN 37831-6285
managed by
LOCKHEED MARTIN ENERGY RESEARCH CORP.
for the
U.S. DEPARTMENT OF ENERGY
under contract DE-AC05-96OR22464



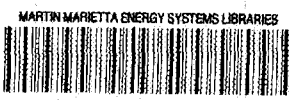

## TABLE OF CONTENTS

## LIST OF FIGURES

## LIST OF TABLES

## ACRONYMS

| | |
|---|---|
| ANS | Advanced Neutron Source |
| CHF | critical heat flux |
| CL | centerline temperature limit |
| CPBT | core pressure boundary tube |
| DT | spallation temperature difference limit |
| FE | flow excursion |
| HFIR | High Flux Isotope Reactor |
| IB | incipient boiling |
| ICR | inner control rods |
| INEL | Idaho National Engineering Laboratory |
| LSSS | limiting safety system set point |
| PDF | probability density function |
| RV | reflector vessel |
| RVT | reflector vessel tank |
| SPF | statistical peaking factor |

## ABSTRACT

This report is intended to be a supplement to ORNL/TM-12398, *Steady-State Thermal-Hydraulic Design Analysis of the Advanced Neutron Source Reactor.*[1] It updates the core thermal-hydraulic design to the latest three-element configuration and also provides the most recent information on the thermal-hydraulic statistical uncertainty analysis. In addition, it includes calculations of beam tube cooling and control rod lift forces, which were not addressed in the initial report. This report describes work that is a snapshot in time as it stood at the end of the project.

The three-element core calculations include a description of changes made to the overall coolant system; however, most of the analysis is focused on fuel loading thermal-hydraulic calculations. This analysis uses updated uncertainty values and indicates that a two-dimensional fuel grading in the three-element core would still be necessary to meet the desired operating and safety criteria. Analysis of cooling in the reflector tank examines various cooling options for the reflector tank components. This work investigated multiple forced convection designs as well as natural convection cooling requirements. Lift forces on the inner control rods caused by the upward coolant flow were also examined. Initial control rod designs were such that a sheared control rod would tend to lift because of flow forces. Design changes were recommended that would eliminate this issue. They included geometry changes to the inner control rod cooling channels, changes to the orificing in the central hole region, and reduction of inner control rod coolant velocity.

# 1. INTRODUCTION

This supplementary report to ORNL/TM-12398, *Steady-State Thermal-Hydraulic Design Analysis of the Advanced Neutron Source Reactor,*[1] is intended to update that report by providing results for a core that contains three separate fuel elements. An updated description of the statistical analysis and additional results for beam tube cooling and control rod hydraulic design are included. Separate reports provide updated information on the thermal-hydraulic correlation development (ORNL/TM-13081),[2] hot spot thermal analysis (ORNL/TM-13072),[3] and fuel manufacturing defect statistical analysis (ORNL/TM-13066),[4] areas that were covered in the original report.

The major change in the design from that discussed in ORNL/TM-12398 is a reduction in the coolant velocity from 25 to 20 m/s and incorporation of a three-element core design and its associated lower power density distribution (Fig. 1.1). Operating power is maintained at 330 $MW_f$ while other major system design features also remain the same (e.g., four coolant loops with three active, features to encourage natural circulation within the coolant system, etc.).

This report describes work that remains a "snapshot" in time. As an example, the calculations discussed in Chap. 2 were performed using two versions of the steady-state thermal-hydraulics code (TASHA), one that analyzed only two elements of the three-element core at one time, and another that had been updated to incorporate simultaneous three-element calculations. In addition, calculations in Chap. 2 were performed for the latest three-element design, while those discussed in Chap. 3 were performed on an earlier two-element design (G693). Chapters 4 and 5 also describe work and designs that were still evolving when the project was canceled.

Chapter 2 of the report discusses the thermal-hydraulic design and thermal limits for the three-element core design. The first section describes changes that were made to the overall coolant loop, while the second outlines the considerations used while designing the fuel loading. The last section in this chapter shows the thermal limits for several three-element core designs that were considered.

Chapter 3 includes updates to the statistical thermal-hydraulic uncertainty analysis used in the project. It covers two types of Monte Carlo–based methodologies in Sect. 3.1, the first based on a peaking-factor methodology and the second on a full Monte Carlo treatment of the uncertainties. Section 3.2 evaluates thermal limits based on worst-case assumptions as was typically used in the past for reactors such as the High Flux Isotope Reactor (HFIR). The last section discusses the importance of truncating the tails of the uncertainty distribution to evaluate very high nonexceedance probability levels effectively.

Chapter 4 presents new analysis of the thermal behavior of components in the reflector vessel (RV) tank. Section 4.2 briefly describes the components in the RV that must be cooled. Section 4.3 describes the different cooling schemes studied and the ones selected for consideration. Section 4.4 calculates decay heat after a scram in the Advanced Neutron Source (ANS) reactor. Section 4.5 studies cooling scheme 1. Section 4.6 covers miscellaneous heat transfer calculations to investigate the feasibility of other cooling schemes. Section 4.7 studies cooling scheme 5. Section 4.8 studies beam tube cooling in the three-element core.

Chapter 5 deals with the issue of hydraulics within the control rods and the control rod lift forces. The four sections in this chapter look at various control rod design options and address methods of reducing control rod lift forces.

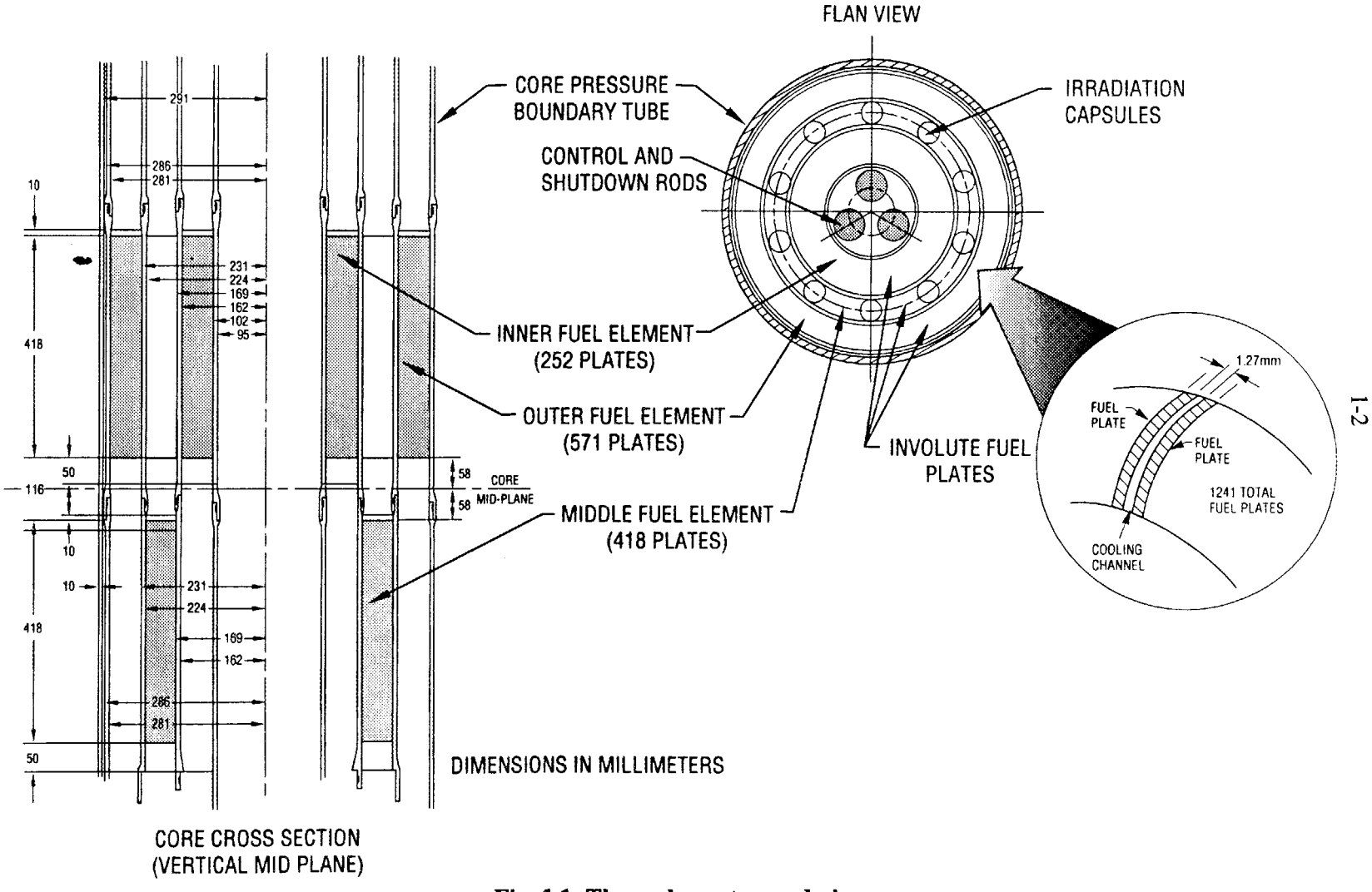


**Fig. 1.1. Three-element core design.**

# 2. SYSTEM AND HYDRAULIC DESIGN

## 2.1 SYSTEM DESIGN

The reactor core geometry shown in Fig. 1.1 was the basis for all of the power limit calculations discussed in this section. This concept has 49% higher coolant flow area than the two-element core design and a 23% increase in surface area. Thus, with the core fission power remaining at 330 $MW_f$, the average heat flux within the core is significantly lower. This allowed a reduction in the coolant velocity from 25 to 20 m/s to improve fuel plate stability behavior. The three-element design also allows the total fuel inventory to be increased, and therefore an increase in the length of the fuel cycle is possible. A comparison of the two core designs is presented in Table 2.1. The remainder of the coolant loop (e.g., piping sizes) was assumed to remain the same as that in the two-element design.

Loop operating conditions, shown in Fig. 2.1, have been altered to accommodate the three-element design changes. Although piping sizes have remained the same, the total coolant flow rate has actually increased, and pressure drops in the piping are somewhat higher than with the two-element design.

## 2.2 FUEL ELEMENT DESIGN

As was done for the two-element design, ideal relative power profiles were generated as a function of axial distance from the core inlet. The ideal radial power distribution would be uniform, because the parameters that influence the ideal distributions (pressure, temperature, etc.) would not change along the span of the fuel plates. These axial profiles, if achievable, would allow the maximum operating margin or the maximum operating power for the three-element design. The profiles are skewed toward the inlet of the core, where the coolant temperature is the lowest and the coolant pressure is the highest. They were calculated by adjusting the local relative power density until every point on the plate was at the selected limit. Ideal power profiles for five separate limits are presented in Fig. 2.2. These profiles are somewhat flatter than those for the two-element design because the core heated length is shorter and the core

**Table 2.1. Comparison of two- and three-element core design**

| | Two-element design | Three-element design |
|---|---|---|
| Core volume, L | 67.6 | 82.6 |
| Thermal power, MW | 303 | 303 |
| Average power density, MW/L | 4.5 | 3.7 |
| Peak heat flux, $MW/m^2$ | 12 | 8.0 |
| Coolant inlet velocity, m/s | 25 | 20 |
| Core inlet pressure, Mpa | 3.2 | 2.7 |
| Core pressure drop, Mpa | 1.4 | 0.8 |
| Inlet coolant temperature, °C | 45 | 45 |
| Exit coolant temperature, °C | 85 | 79 |
| Exit subcooling level, °C | 110 | 130 |

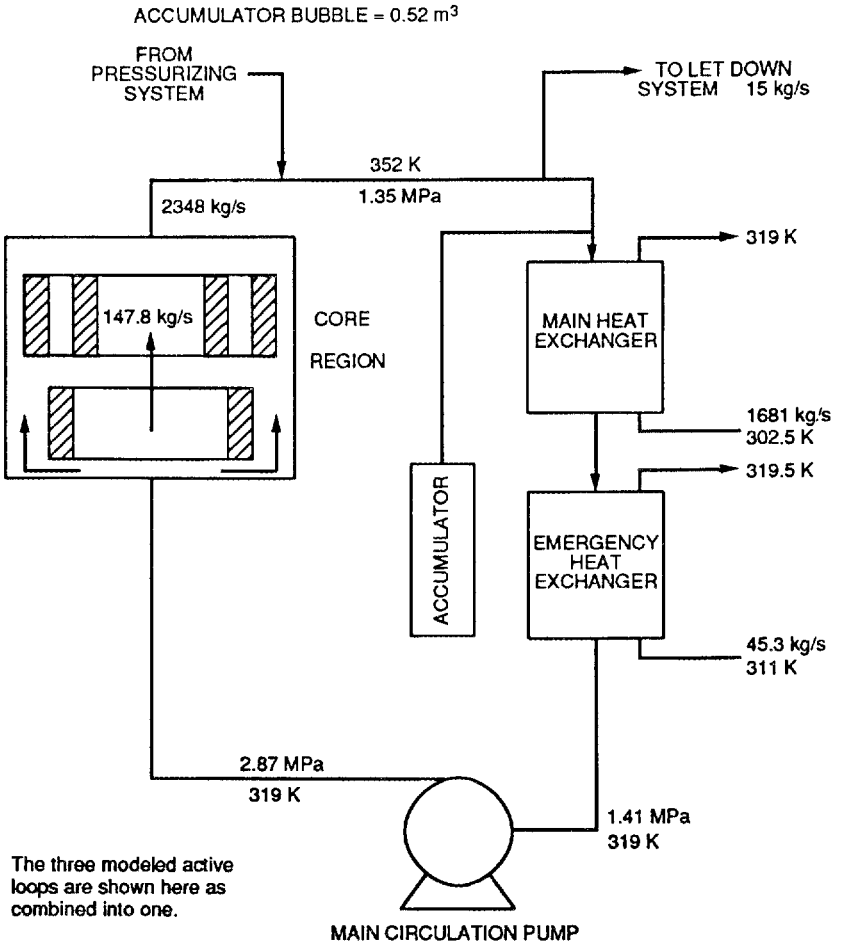


**Fig. 2.1. Loop operating conditions.**

pressure drop is smaller. The critical heat flux (CHF) curve has the most severe profile because the CHF correlation used to generate the curve (Gambill/Weatherhead[5]) is more sensitive to local coolant pressure and temperature than either the incipient boiling (IB) limit or the limit defined by the point where the wall temperature is equal to the saturation temperature ($T_{wall} = T_{sat}$). The oxide-limited profiles, the maximum centerline temperature limit (CL, 400°C), and the spallation limit (DT, defined as when the temperature drop across the oxide film is 119°C) are insensitive to the local pressure and therefore tend to have flatter ideal relative power density profiles than do the other limits. Although the oxide-limited ideal relative power density profiles (CL and DT) are nearly the same, the centerline temperature–limited profile is skewed to the core inlet a bit more than the temperature drop limit.

The ideal profiles were used as a benchmark for developing the fuel loading design via neutronic analyses. They served as a way of judging the quality of the fuel grading in a process that iteratively moved fuel to different locations on the fuel plate, then checked the power density distributions against the ideal profile until the best match was achieved. The actual fuel loadings developed from this process resulted in the relative power density distributions shown in Fig. 2.3. The ideal profiles could not be duplicated exactly because parameters such as fuel burnup and the varying proximity of the fuel to the $D_2O$ reflector influence the time and space dependence of the relative power density distribution. The distributions are biased toward higher fuel loading at the coolant inlet, however.

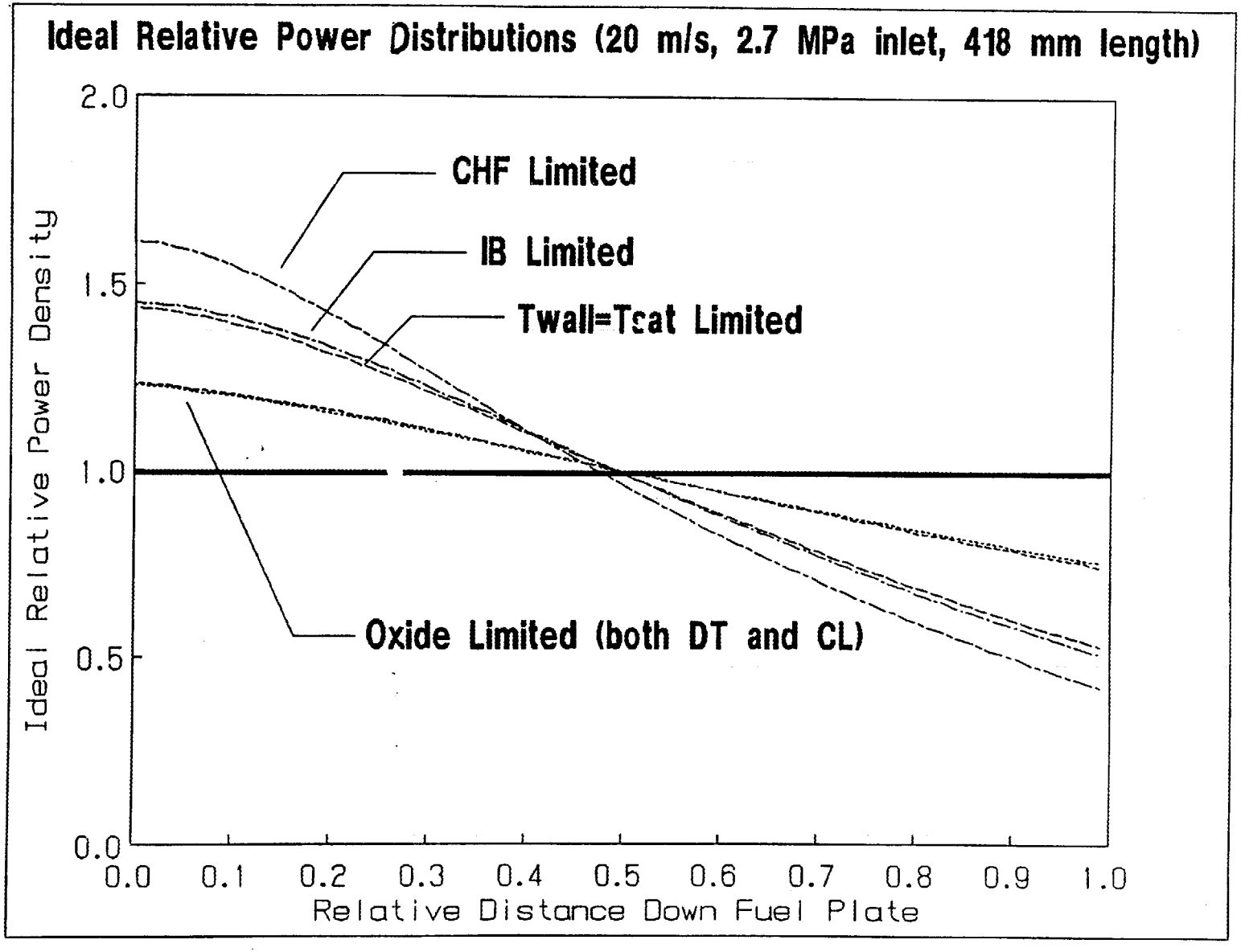


**Fig. 2.2. Ideal relative power profiles for the three-element core.**

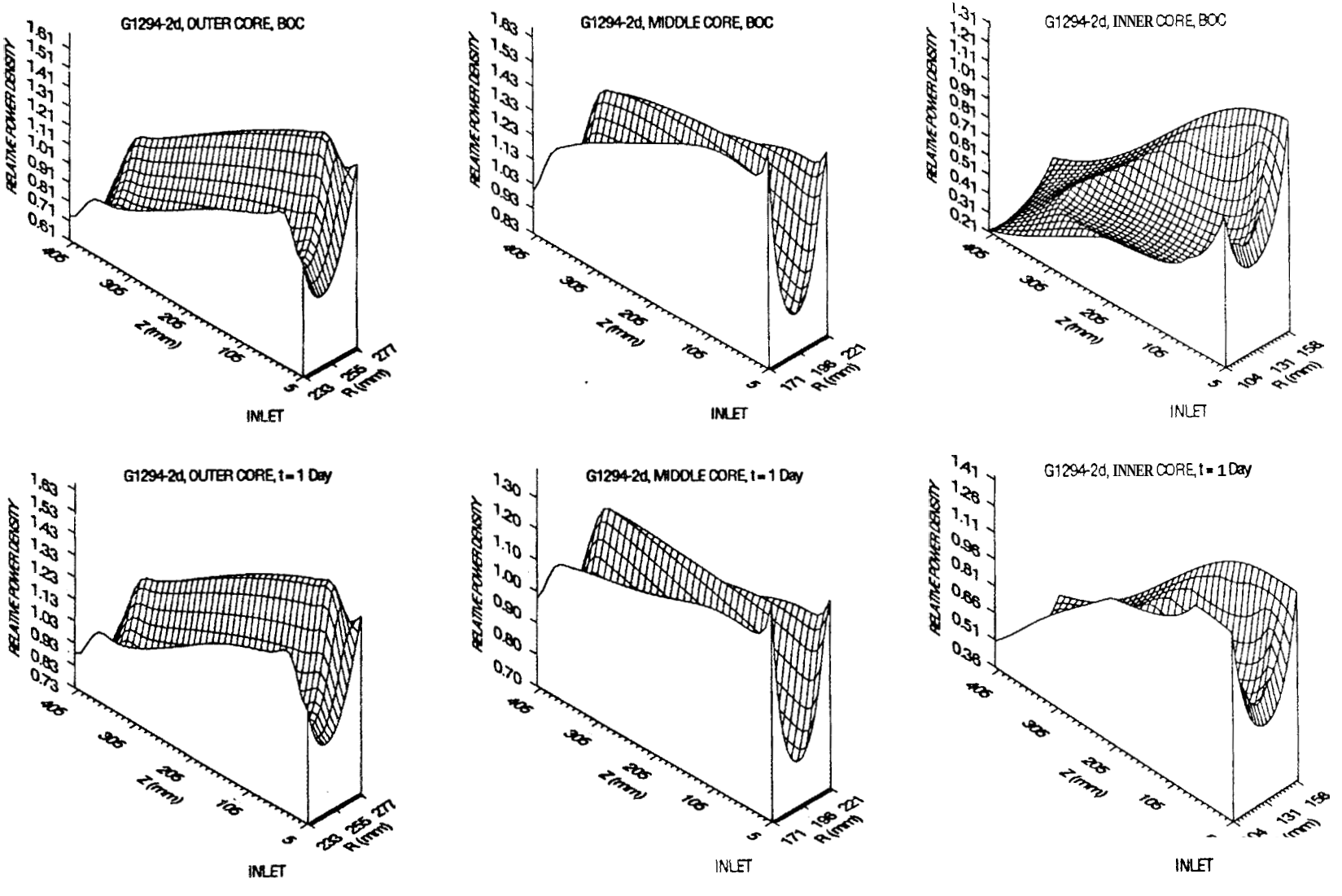


**Fig. 2.3. Actual relative power density profiles for fuel design G1294-2d.**

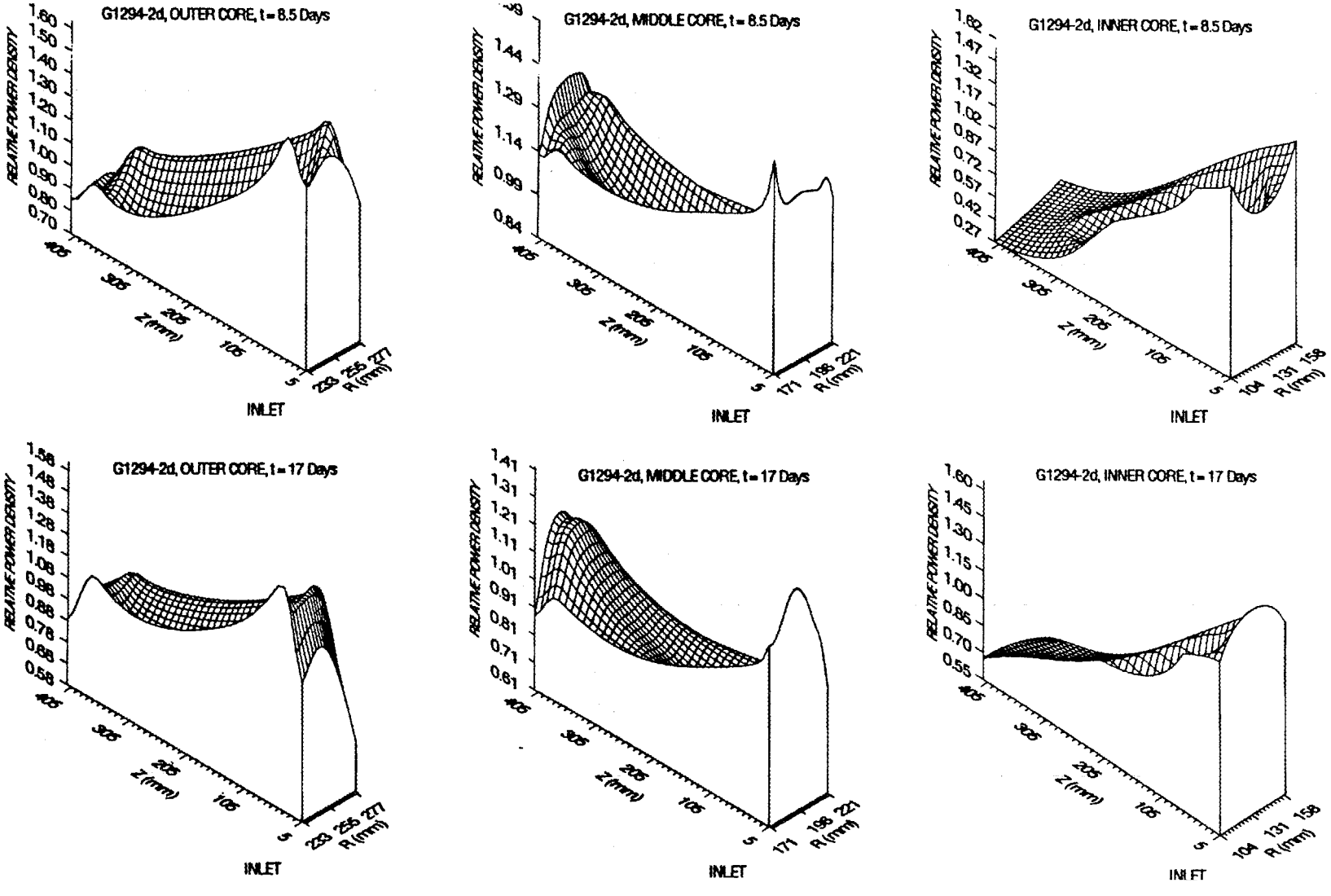


**Fig. 23 (continued)**

A series of calculations was also performed to examine the importance of grading the fuel in both axial and radial (spanwise) directions. Three separate gradings were performed, one with the conventional two-dimensional grading (power density results are shown in Fig. 2.3), one with grading only in the radial direction (as is done with HFIR), and one with uniform grading. These gradings were designated G1294-2d, G1294-1d, and G1294-0d, respectively. Table 2.2 shows a comparison of core power splits for all three three-element core designs. The numbers in the table represent the percentage of total core power in each of the fuel elements at different times in the fuel cycle. The greatest shift in core power over the fuel cycle is in the inner core, where a shift of up to 50% occurs for the no-fuel-grading design. This design shows the most severe shift in power, while the one-dimensional design shows the least. All thermal-hydraulic calculations presented here assume that the fuel is 50% enriched, and conductivities for 3.5-g/cc fuel loading are also assumed.

Table 2.3 shows the peak relative power density and maximum hot streak ratios for the three designs as a function of time in the fuel cycle. In addition, the core is identified where these maximum values occur. The G1294 designs get progressively worse in terms of peak values as the amount of grading decreases. The highest peak relative power density in the two-dimensional design is 1.71, while that in the no-grading design is 2.83. Similarly with the maximum hot streak ratio, the highest value in the two-dimensional design is 1.44, while that in the no-grading design is 2.21.

**Table 2.2. Comparison of core power splits**

| Time (d) | Fuel design | Inner | Middle | Outer |
|---|---|---|---|---|
| 0 | G1294-2d | 0.152 | 0.405 | 0.443 |
| | G1294-1d | 0.185 | 0.296 | 0.519 |
| | G1294-0d | 0.129 | 0.420 | 0.452 |
| 1 | G1294-2d | 0.203 | 0.339 | 0.458 |
| | G1294-1d | 0.164 | 0.385 | 0.451 |
| | G1294-0d | 0.175 | 0.359 | 0.467 |
| 4.25 | G1294-2d | 0.196 | 0.351 | 0.454 |
| | G1294-1d | 0.166 | 0.388 | 0.447 |
| | G1294-0d | 0.167 | 0.373 | 0.461 |
| 8.5 | G1294-2d | 0.184 | 0.373 | 0.443 |
| | G1294-1d | 0.175 | 0.386 | 0.439 |
| | G1294-0d | 0.159 | 0.391 | 0.451 |
| 12.75 | G1294-2d | 0.199 | 0.360 | 0.441 |
| | G1294-1d | 0.200 | 0.362 | 0.438 |
| | G1294-0d | 0.174 | 0.378 | 0.448 |
| 17 | G1294-2d | 0.220 | 0.336 | 0.444 |
| | G1294-1d | 0.235 | 0.321 | 0.444 |
| | G1294-0d | 0.195 | 0.354 | 0.451 |

**Table 2.3. Comparison of peak relative power density and hot streak ratio**

| Time (d) | Fuel design | Peak relative power density[a] | | Hot streak ratio | |
|---|---|---|---|---|---|
| | | Value | Element | Value | Element |
| 0 | G1294-2d | 1.71 | Middle | 1.44 | Middle |
| | G1294-1d | 2.20 | Outer | 1.64 | Outer |
| | G1294-0d | 2.83 | Outer | 2.18 | Outer |
| 1 | G1294-2d | 1.66 | Outer | 1.39 | Outer |
| | G1294-1d | 2.16 | Outer | 1.43 | Outer |
| | G1294-0d | 2.79 | Outer | 2.21 | Outer |
| 4.25 | G1294-2d | 1.66 | Outer | 1.35 | Outer |
| | G1294-1d | 2.29 | Outer | 1.30 | Outer |
| | G1294-0d | 2.66 | Outer | 2.00 | Outer |
| 8.5 | G1294-2d | 1.69 | Outer | 1.27 | Outer |
| | G1294-1d | 2.36 | Outer | 1.16 | Middle |
| | G1294-0d | 2.36 | Outer | 1.74 | Outer |
| 12.75 | G1294-2d | 1.69 | Outer | 1.23 | Outer |
| | G1294-1d | 2.35 | Inner | 1.12 | Outer |
| | G1294-0d | 1.96 | Outer | 1.53 | Outer |
| 17 | G1294-2d | 1.70 | Inner | 1.23 | Outer |
| | G1294-1d | 2.14 | Inner | 1.17 | Outer |
| | G1294-0d | 1.67 | Outer | 1.37 | Outer |

[a]Ratio of local to core average power density.

## 2.3 UNCERTAINTY VALUES

Uncertainty values used in the thermal-hydraulic calculations are presented in Table 2.4. A description of how these values were developed is presented in ORNL/TM-12398. Table 2.5 shows the factors used to establish the parameter values when operating and safety margin calculations are performed. A description of how these values were developed is also discussed in ORNL/TM-12398.

## 2.4 THERMAL POWER LIMITS

Table 2.6 shows the limiting power levels for various thermal limits [at different margins (operating or safety) and probability levels (in parentheses)] for each of the fuel designs. Additionally, the limiting location and time in the fuel cycle are also shown. As indicated in the table, only the two-dimensional grading meets the ANS acceptance criteria[6] for IB and CHF at the safety margin. Also, the middle or outer cores are limiting early in the fuel cycle. An examination of the area in these cores that is limiting (this was done for the two-dimensional grading only) indicates that approximately 15% of the limiting core

**Table 2.4. Uncertainty values used in steady-state thermal-hydraulic**

| | Best estimate[a] | 95% Probability[b] | 99.9% Probability[b] |
|---|---|---|---|
| Hot spot (IB,[c] CHF[d]) | 1.33 | 1.59 | 1.94 |
| Hot spot (FE[e]) | 1.11 | 1.33 | 1.63 |
| Hot spot (oxide) | 1.11 and 1.33 | 1.17 and 1.39 | |
| Hot channel | 1.05 | 1.10 | 1.12 |

[a]Channel gap was assumed to be the nominal valve, 1.27 mm, for the best-estimate calculation.

[b]For both the 95 and 99.9% probability analyses, a minimum channel gap of 1.143 mm was assumed.

[c]IB = incipient boiling.

[d]CHF = critical heat flux.

[e]FE = flow excursion.

**Table 2.5. Values for inlet temperature, exit pressure, and flow[a]**

| | Inlet temperature | Exit pressure | Flow |
|---|---|---|---|
| Best estimate | 1.0 | 1.0 | 1.0 |
| Operating margin | 1.014 | 0.949 | 0.99 |
| Safety margin | 1.217 | 0.789 | 0.99 |

[a]Multiplier relative to nominal.

would have to be regraded in order to improve the limiting power by approximately 10%. Note that the steady-state thermal-hydraulic code does not incorporate any two-phase pressure drop relationships. This means that flow rates in the coolant channels will be reduced over those determined in these calculations. The limits of CHF and flow excursion (FE) presented here are therefore higher than those that would be calculated if two-phase pressure drops were accurately calculated. When the project ended, development of a two-phase pressure drop model was in progress and would have been incorporated into a revised version of the steady-state thermal-hydraulics code.

Table 2.7 shows the power limits established by oxide growth. These are presented as a function of time in the cycle for both the oxide spallation criteria and the centerline temperature limit for each of the core designs. The limiting power for all cases occurs near the end of the fuel cycle. Only the two-dimensional fuel grading is capable of meeting these acceptance criteria.[6] In addition, the table shows the limiting location at each time step and for each fuel design. The middle and outer cores are most limiting.

Figures 2.4 and 2.5 show the results of the limiting power calculations in graphical form. These emphasize the fact that the G1294-2d core is the only design that meets all of the present acceptance criteria.[6] A detailed description of the thermal behavior of this core over the 17-d fuel cycle is presented in Figs. 2.6 to 2.8, which show 95% probability level predictions at nominal operating power. Figure 2.6 shows the oxide thickness on each of the three fuel elements during the cycle for the G1294-2d fuel design. The maximum oxide thickness reached is 12.1 μm. Figure 2.7 shows the resulting maximum centerline temperatures. The maximum centerline temperature of 266°C occurs at the end of the fuel cycle. The location of this maximum is near the entrance of the inner core. A significant amount of margin

**Table 2.6. Limiting thermal power levels, locations, and times at 20 m/s coolant velocity and 2.7 MPa inlet pressure**

| Fuel design | IB (95%) operating margin | CHF (95%) operating margin | FE (95%) operating margin | $T_w = T_{sat}$ (95%) operating margin | CHF (99.9%) safety margin | FE (99.9%) safety margin |
|---|---|---|---|---|---|---|
| | | | **Power level, in $MW_t$** | | | |
| G1294-2d | 398 | 567 | 566 | 366 | 462 | 466 |
| G1294-1d | 263 | 397 | 430 | 239 | 317 | 347 |
| G1294-0d | 213 | 308 | 324 | 195 | 247 | 261 |
| | | | **Limiting location[a] and time** | | | |
| G1294-2d | M, 20, 40 | M, 4, 40 | M, 4, 43 | M, 20, 40 | M, 21, 40 | M, 4, 43 |
| | 1 d | 1 d | 1 d | 1 d | 1 d | 1 d |
| G1294-1d | O, 4, 43 | O, 23, 43 | O, 23, 43 | O, 4, 43 | O, 4, 43 | O, 23, 43 |
| | BOC[b] | BOC | 1 d | BOC | BOC | 1 d |
| G1294-0d | M, 23, 43 | O, 23, 43 | O, 23, 43 | M, 23, 43 | O, 23, 43 | O, 23, 43 |
| | BOC | 4.25 d | 4.25 d | BOC | 4.25 d | 4.25 d |

[a]I = inner element, M = middle element, O = outer element. Numbers designate grid location span and length. Span varies for each element 4–23; length varies 4–43.

[b]BOC = beginning of cycle.

**Table 2.7. Oxide-limiting power levels, operating margin at 20 m/s coolant velocity and 2.7 MPa inlet pressure**

| Time in cycle (d) | Fuel design | ΔT (95%) | | $T_{CL}$ (95%) | |
|---|---|---|---|---|---|
| | | Power ($MW_t$) | Limiting location[a] | Power ($MW_t$) | Limiting location |
| 0 | G1294-2d | | | | |
| | G1294-1d | | | | |
| | G1294-0d | | | | |
| 1 | G1294-2d | 507 | M, 20, 39 | 493 | M, 23, 43 |
| | G1294-1d | 345 | O, 4, 43 | 330 | M, 20, 39 |
| | G1294-0d | 280 | M, 23, 43 | 270 | O, 4, 43 |
| | | | | | M, 23, 43 |
| 4.25 | G1294-2d | 454 | O, 19, 38 | 463 | O, 19, 38 |
| | G1294-1d | 318 | O, 4, 43 | 327 | O, 4, 43 |
| | G1294-0d | 236 | O, 23, 43 | 239 | O, 23, 43 |
| 8.5 | G1294-2d | 415 | M, 20, 40 | 435 | M, 20, 40 |
| | G1294-1d | 299 | O, 4, 43 | 313 | O, 4, 43 |
| | G1294-0d | 222 | O, 23, 43 | 232 | M, 23, 43 |
| 12.75 | G1294-2d | 385 | M, 20, 40 | 402 | M, 19, 43 |
| | G1294-1d | 288 | M, 12, 43 | 298 | M, 12, 43 |
| | G1294-0d | 212 | M, 23, 43 | 225 | M, 23, 43 |
| 17 | G1294-2d | 375 | M, 18, 43 | 397 | M, 18, 43 |
| | G1294-1d | 273 | M, 12, 43 | 287 | M, 12, 43 |
| | G1294-0d | 214 | M, 23, 43 | 232 | M, 23, 43 |

[a]M = middle element, O = outer element. Numbers designate grid location span and length. Span varies for each element 4–23; length varies 4–43.

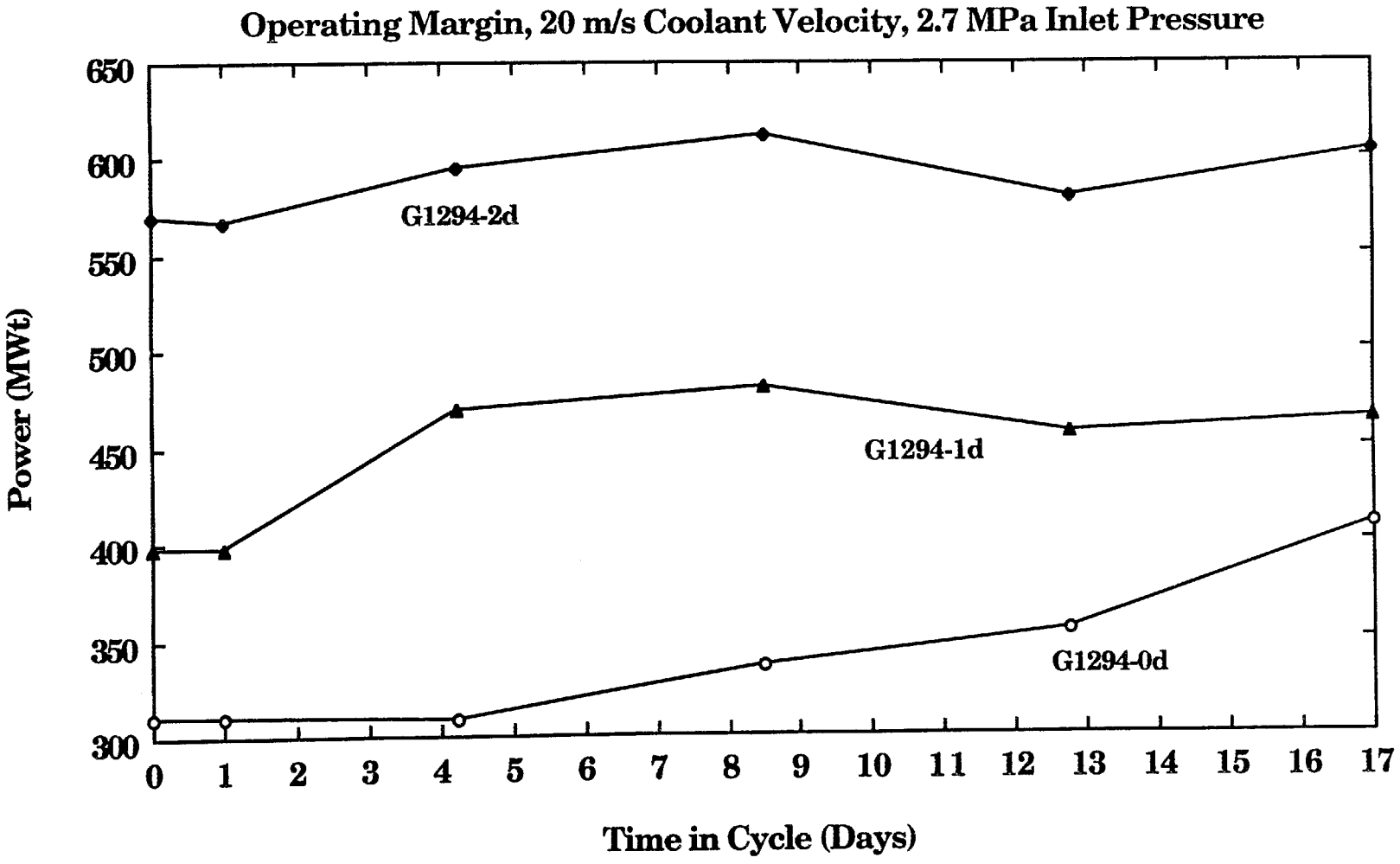


Fig. 2.4. Limiting power levels established by the critical heat flux limit.

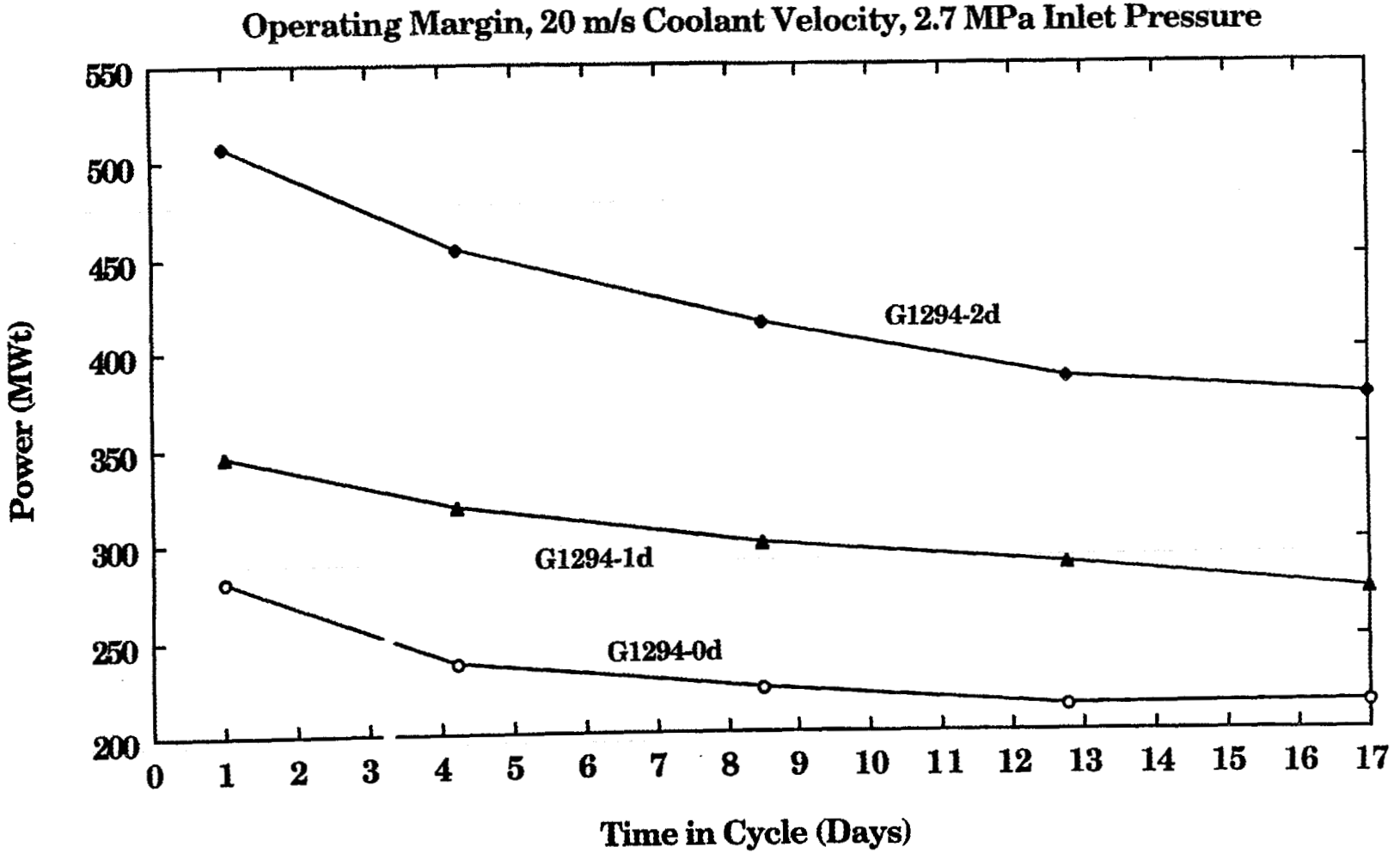


Fig. 2.5. Limiting power levels established by oxide growth.

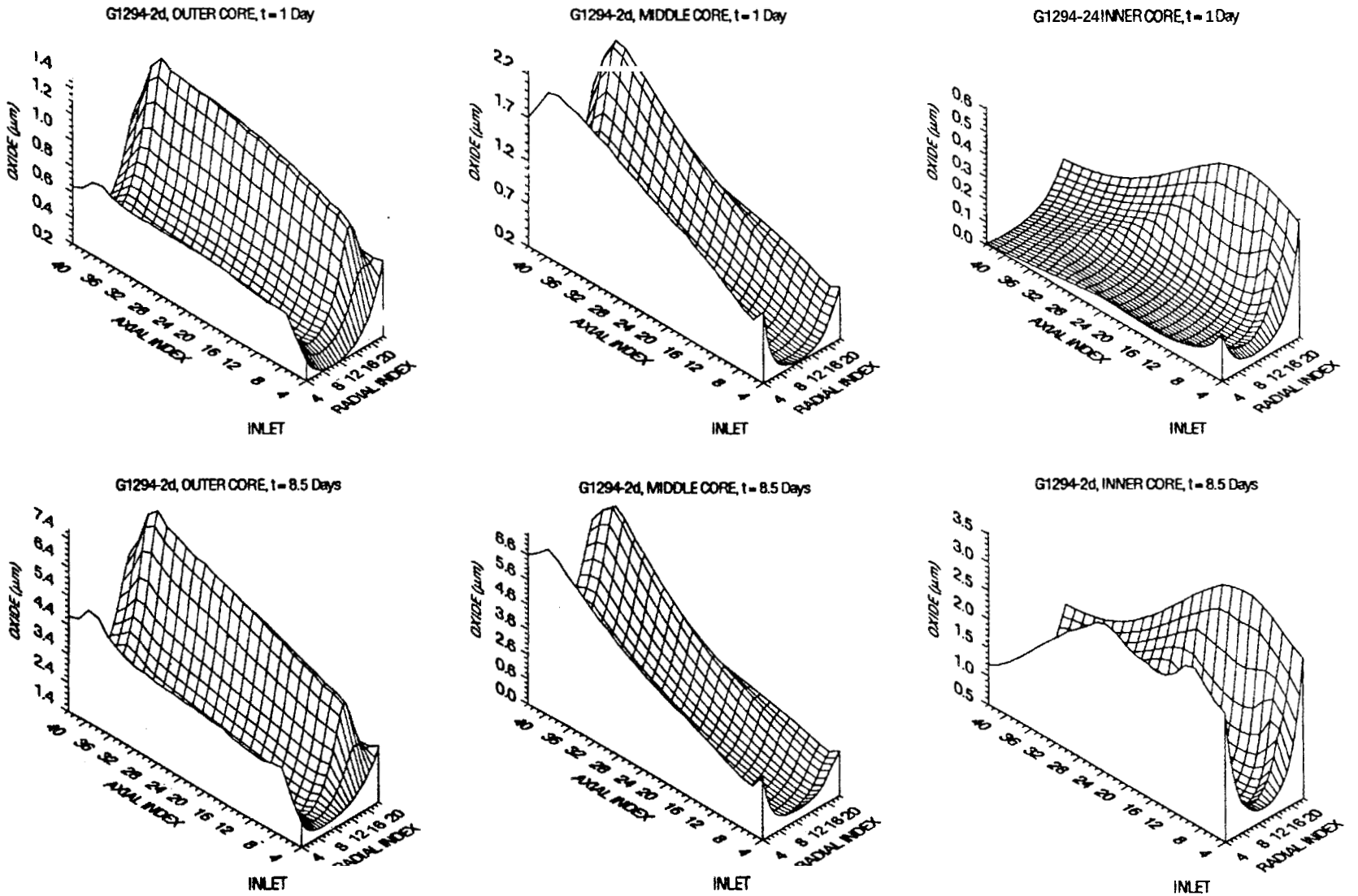


**Fig. 2.6. Oxide thickness as a function of time in the fuel cycle for the G1294-2d fuel design.**

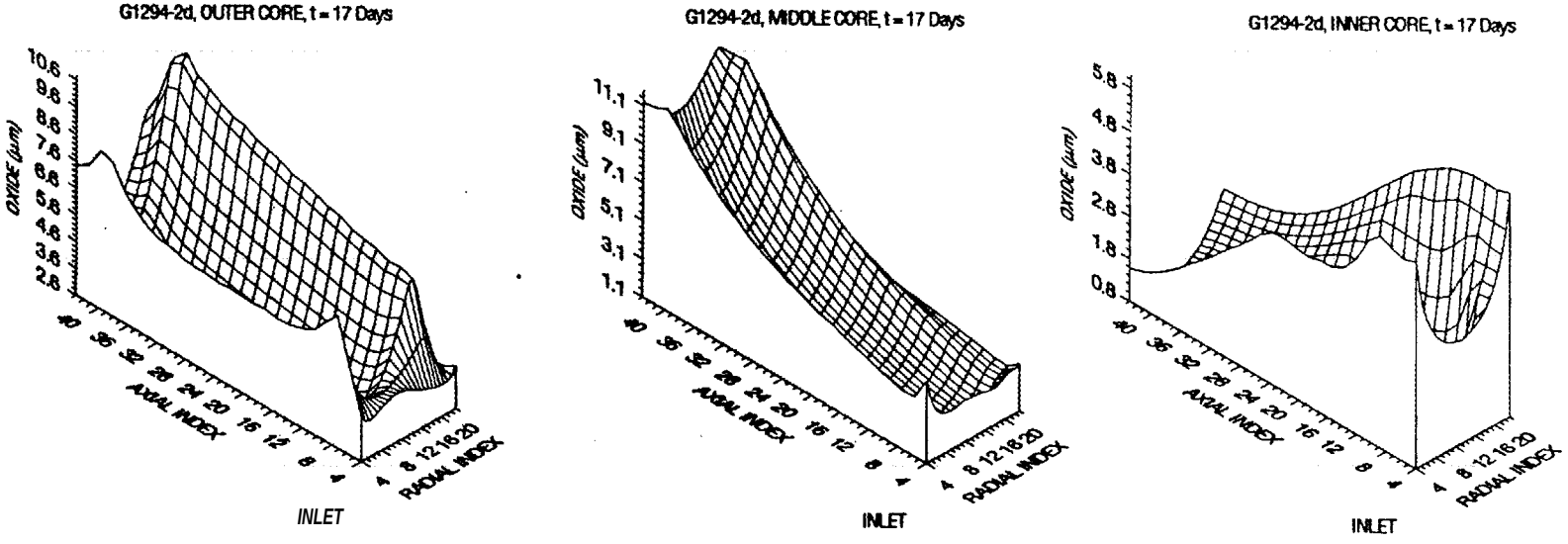


**Fig. 2.6 (continued)**

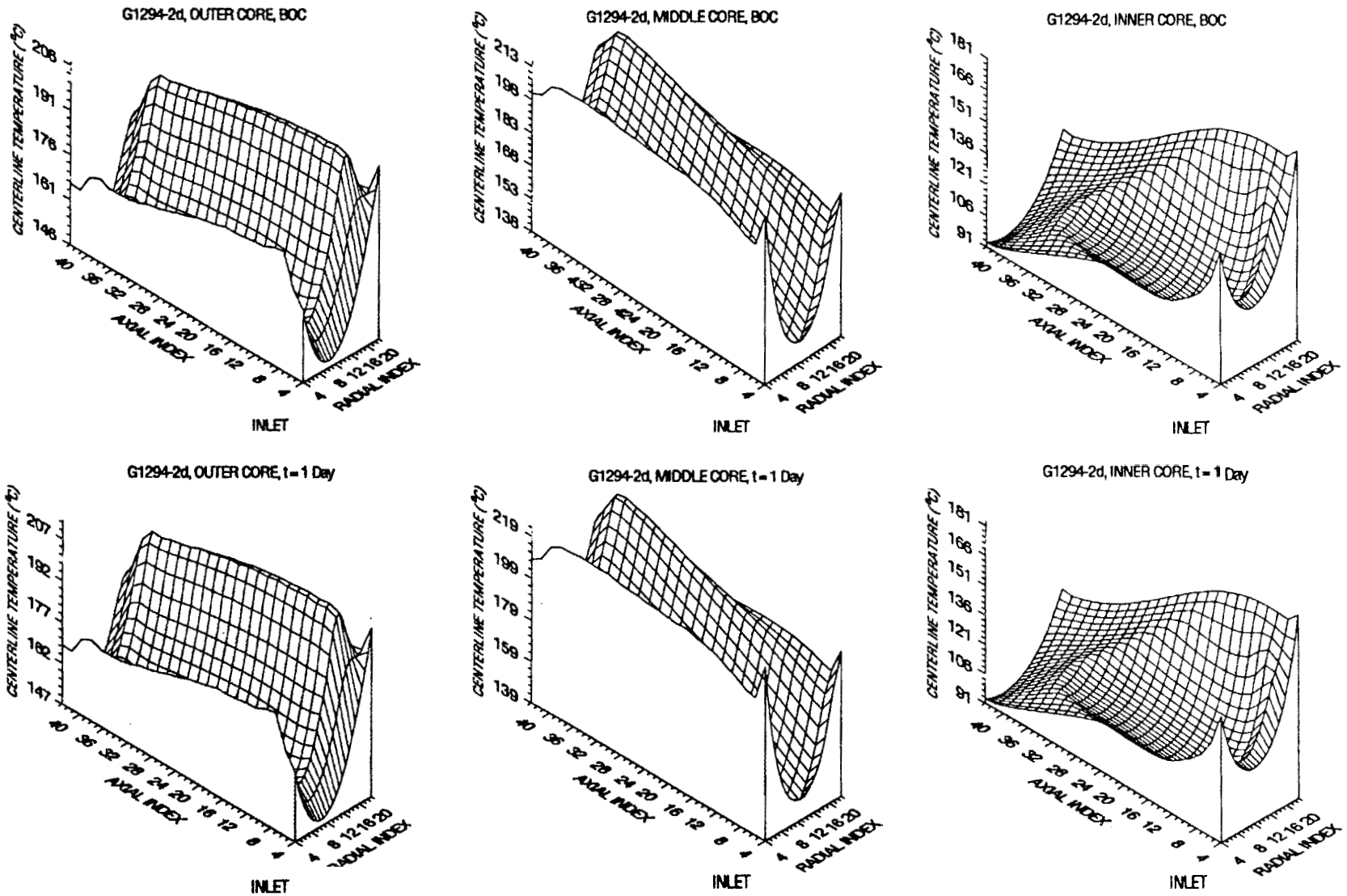


**Fig. 2.7. Centerline temperatures as a function of time in the fuel cycle for the G1294-2d fuel design.**

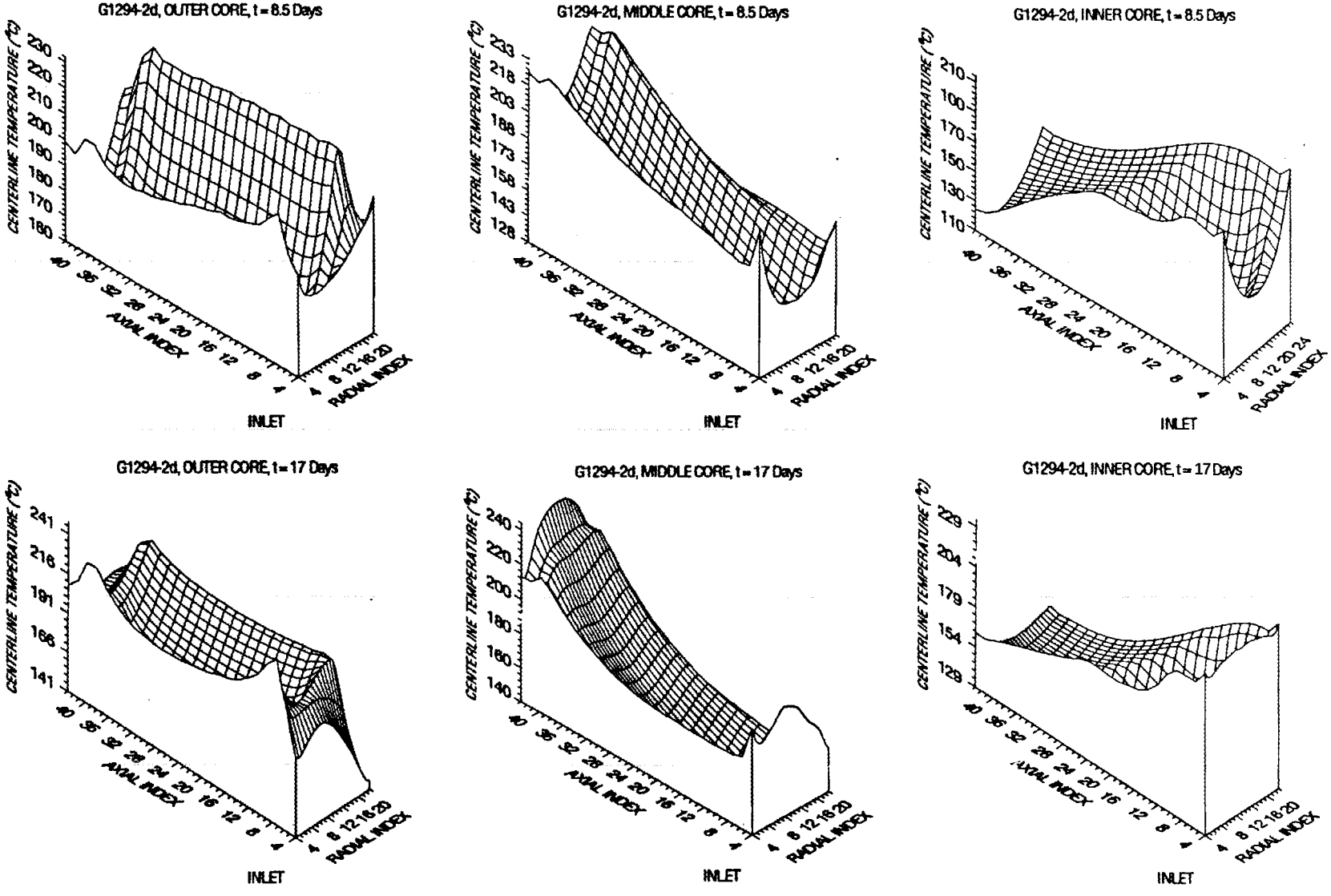


Fig. 27 (continued)

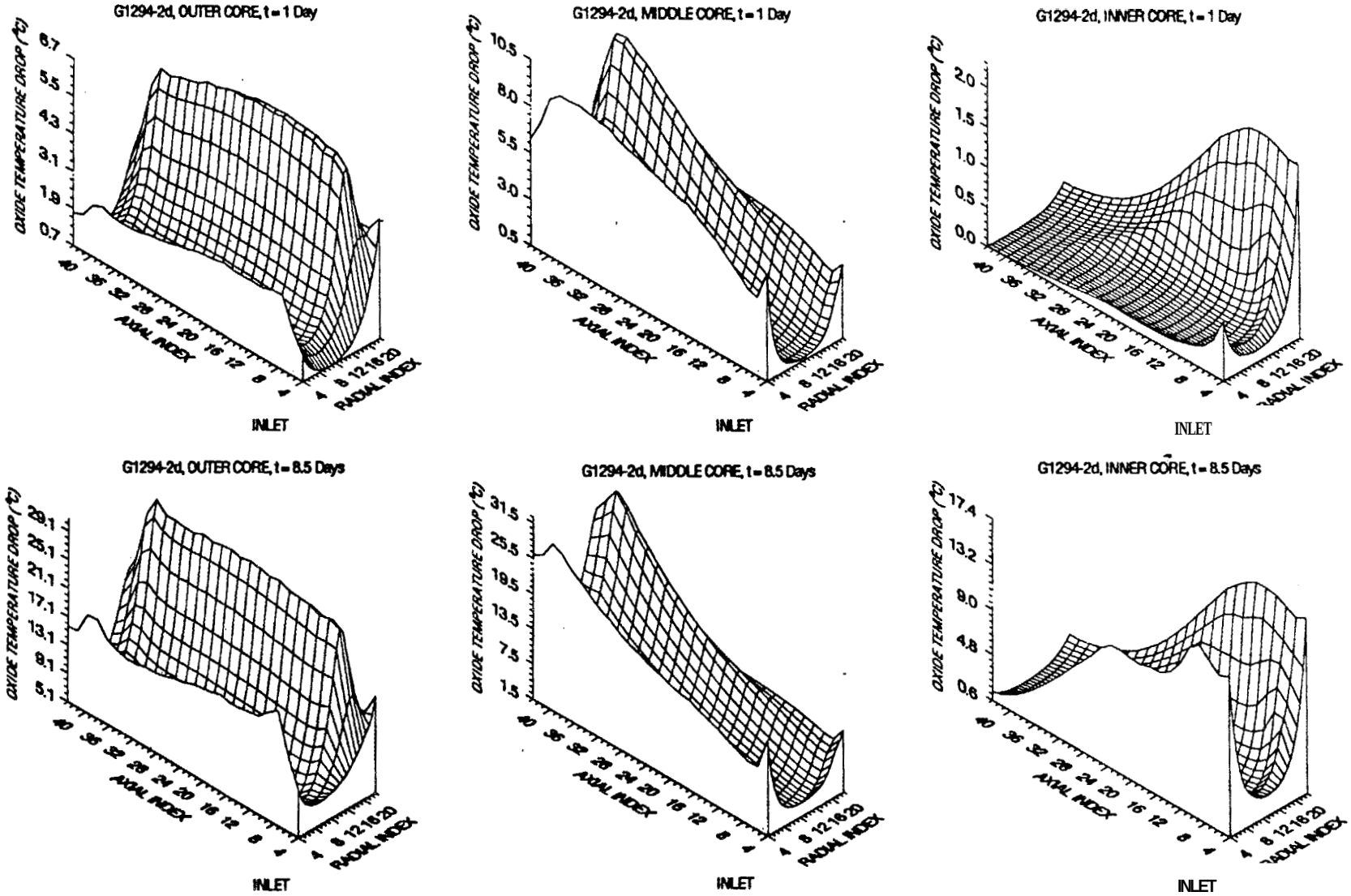


**Fig. 2.8. Temperature drop across the oxide film as a function of time in the fuel cycle for the G1294-2d fuel design.**

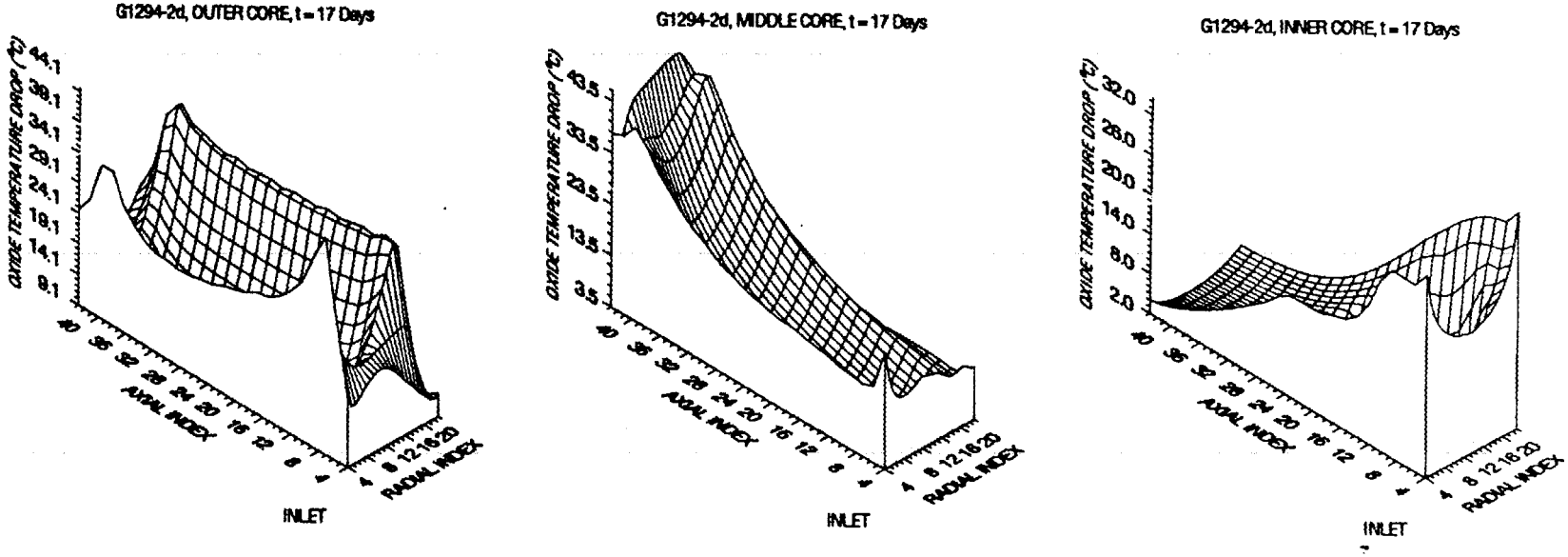


**Fig. 2.8 (continued)**

therefore exists between normal operating conditions and the point where the core could reach the centerline temperature limit of 400°C.[7] The temperature drop across the oxide film is shown in Fig. 2.8. These plots present a measure of how close the core comes to reaching the spallation limit of 119°C temperature drop across the oxide film.[8] The maximum temperature drop is observed at the middle core exit and is only 54°C, indicating that the design has substantial margin to the spallation limit as well. Table 2.8 lists these parameters as a function of time in the cycle for the G1294-2d fuel design.

Calculations to evaluate the three-element core design's susceptibility to a core inlet flow blockage were also performed. These calculations forced 1.5 times the nominal single-channel coolant heat load to be deposited in the coolant channel, simulating the performance of a coolant channel that had a neighboring channel fully blocked. The plate forming one side of the blocked channel was assumed to be insulated on the blocked side of the plate. This plate then experienced twice the nominal surface heat flux on the side that remained cooled. Calculations were performed in order to determine if the cooled side of the plate would undergo a CHF under these conditions. The manner in which the calculations were performed requires that a maximum CHF power comparison be made with two times the nominal operating power, or 606 $MW_t$. This comparison is shown in Table 2.9. As implied by the table, the two-dimensional fuel grading meets this criterion, but the other gradings do not.

Figure 2.9 shows the operating map for the three-element core design using two-dimensional grading. It is constructed to illustrate the relationships between nominal conditions, conditions allowed by the reactor protection system, and accident conditions. The smallest and innermost region is that of normal operation. Throughout this region, there is no boiling at any point in the core. The small square around the nominal operating conditions represents possible instrument errors and minor control variations. Anticipated events might perturb pressure or power in a wide region around the nominal, but are interrupted with little overshoot after the limiting safety system set point (LSSS) is exceeded. The more severe challenges represented by other accidents may push the power-to-flow ratio and/or pressure beyond the LSSSs into the crosshatched region of Fig. 2.9, the region below the 95% probability CHF curve. The results presented in this figure are accurate for steady-state, nonboiling conditions; reasonably accurate in a quasi-steady-state sense to transients in the anticipated event category; and less accurate for accidents beyond that category.

Three accident paths are illustrated on Fig. 2.9. Path X-X′-X″ represents a loss of pressure without change in flux-to-flow ratio. Path Y-Y′-Y″ could be a pump coastdown or another accident involving

**Table 2.8. Maximum conditions over the fuel cycle during normal operation for the G1294-2d fuel grading at 95% probability and 303 $MW_t$**

| Cycle time (d) | Oxide (μm) | | | Oxide temperature drop (°C) | | | Centerline temperature (°C) | | |
|---|---|---|---|---|---|---|---|---|---|
| | I[a] | M | O | I | M | O | I | M | O |
| 1 | 0.53 | 2.24 | 1.48 | 2.25 | 10.7 | 6.46 | 183.8 | 227.4 | 214.3 |
| 4.25 | 2.08 | 4.76 | 4.93 | 9.49 | 20.5 | 20.9 | 200.9 | 220.3 | 227.2 |
| 8.5 | 3.54 | 7.63 | 7.75 | 16.7 | 33.4 | 29.2 | 214.8 | 235.1 | 234.6 |
| 12.75 | 4.80 | 10.4 | 9.55 | 28.6 | 46.3 | 38.3 | 238.4 | 261.4 | 241.9 |
| 17 | 6.14 | 12.1 | 10.9 | 37.8 | 54.2 | 47.4 | 247.5 | 266.1 | 257.2 |

[a]I = inner element, M = middle element, O = outer element.

**Table 2.9. Critical heat flux (95% uncertainty) limiting thermal power levels for blocked channel case at the operating margin**

| Fuel design | CHF limiting thermal power level[a] ($MW_t$) |
|---|---|
| G1294-2d | 651 |
| G1294-1d | 481 |
| G1294-0d | 384 |

[a]CHF limiting power should be compared to twice the nominal operating power.

simultaneous degradation of core outlet pressure and flux-to-flow ratio. Path Z-Z″-Z″ would be typical of a power excursion, with the flux-to-flow ratio increasing without any concomitant loss of core outlet pressure.

Path Y-Y′-Y″ of Fig. 2.9 was chosen hypothetically and is therefore not guaranteed to represent any specific event. Pressure decay with flux-to-flow increase traces a path toward the CHF safety limit curve. When the edge of the 99.9% probability CHF curve is reached, there is a 0.1% chance of CHF at the worst location within the core. At the LSSS point and well before point Y is reached, automatic control action would insert control rods in an attempt to maintain a flux-to-flow ratio of one, and the letdown valves would close in an attempt to maintain a constant core outlet pressure. If these control actions are not effective, continued degradation of the control parameters would result in the set point for flux-to-flow scram being exceeded, and the most likely event at that point would be reactor scram and rapid power reduction with a consequent rapid improvement in the safety margin. Although the ANS scram systems are very fast, a very rapidly developing accident might force the trajectory to point Y′. The probability of hot spot CHF at point Y′ is 0.05. This probability is acceptable when considering the frequency of initiating events capable of causing significant overshoot past the scram settings. Continued degradation of reactor pressure and flux-to-flow ratio would lead to a rapid increase in the probability of FE or CHF until, at point Y″, there would be an even chance of exceeding the FE or CHF limit.

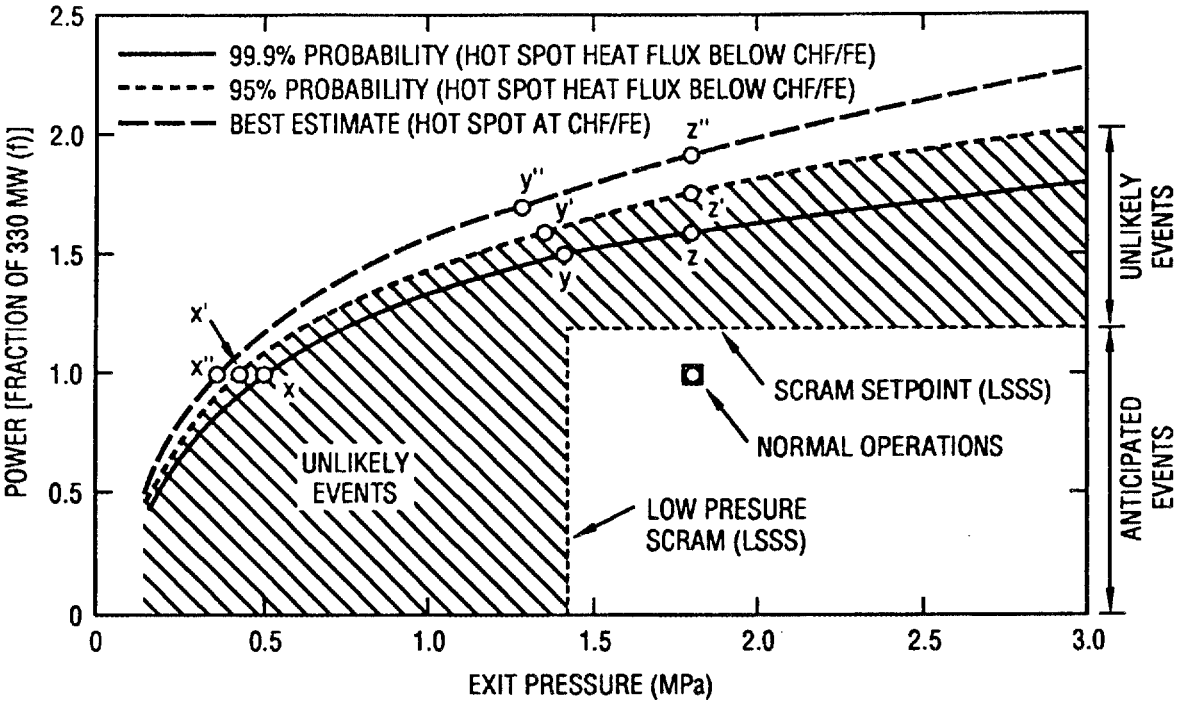


**Fig. 2.9. Operating map for three-element core design.**

# 3. THERMAL-HYDRAULIC UNCERTAINTY ANALYSIS

## 3.1 COMPARISON OF RESULTS FROM SAMPLE/TASHA TO THOSE BASED ON STATISTICAL PEAKING FACTORS

The ANS steady-state statistical thermal analysis code, which is an integrated code consisting of SAMPLE (a statistical analysis code[9]) and TASHA (the ANS steady-state thermal code), was revised from the version used in initial analysis.[1] The revision entailed updating TASHA to include a number of changes made to the code since the original integration of the codes was performed. Using similar input parameter uncertainties, results for the G693 fuel design obtained with the revised statistical thermal analysis code (SAMPLE/TASHA) were compared to those obtained with the statistical peaking factor methodology that was employed for the ANS conceptual safety analysis report. It was found that the maximum operating power levels at a probability of 95% calculated with the two approaches were in close agreement, with the former indicating a slightly higher power level. Results from the comparison are presented in Table 3.1 for three cases: power limited by the centerline temperature ($T_{CL}$), the incipience of boiling, and the critical heat flux. The SAMPLE/TASHA calculations only used 200 ($T_{CL}$, IB) or 600 (CHF) trials for this initial comparison, so the confidence intervals are rather large. Note that the results presented in the table are for only a single time point in the fuel cycle and are *not* the most limiting time points, but for the IB and CHF cases, the selected time point is close to the most limiting one. However, this fact is not important as far as comparing methodologies is concerned. Based on this comparison, it is concluded that the two approaches have been implemented successfully in ANS statistical analysis.

Obviously, additional SAMPLE/TASHA calculations are needed, using more trials, including other time points in the fuel cycle, and treating more parameters probabilistically. Unfortunately, SAMPLE/TASHA calculations require significant amounts of computer time (the IB case with 200 trials required ~18 h on an IBM/RISC 6000), which increases roughly proportionally with the number of trials performed times the number of time points in the fuel cycle evaluated. The statistical peaking factor method requires only the time needed for one TASHA calculation (minutes to a couple of hours) plus that needed to calculate the peaking factors, which is significant but easily manageable (~10h). (This would provide maximum power level at a single probability level. If additional probability level calculations were needed, additional TASHA calculations would be required, one for each probability level.) Thus, as SAMPLE/TASHA calculations proceeded, they would have become more fully "statistical." If the gain in the calculated maximum power based on these calculations versus those with the statistical peaking factor method (which treats parameter uncertainty less fully

**Table 3.1. Comparison of steady-state maximum power levels at 95% probability obtained with SAMPLE/TASHA and the statistical peaking factor method**

| Methodology | Maximum power (MW) | | |
|---|---|---|---|
| | $T_{CL}$ limited | IB limited | CHF limited |
| SAMPLE/TASHA[a] | 484–493 | 375–391 | 497–508 |
| Statistical peaking factor method | 481 | 378 | 495 |

[a]Values for lower and upper 90% confidence bounds.

"statistical") was not very significant, we might have elected to continue using the peaking factor method in the calculations. The same reasoning applies to the treatment of uncertainties in transient analysis (e.g., with RELAP5).

## 3.2 WORST-CASE UNCERTAINTY ANALYSIS

The ANS plant design requirement defines a $10^{-5}$/year core melt probability goal, supplemented with a $10^{-4}$/year melt requirement with a cost/benefit analysis to guide deviations from the goal. For normal, steady-state operation, the associated melt risk should not exceed $10^{-5}$/year. If one assumes that hot spot CHF or FE exceedance leads to melting throughout the fuel element or the rest of the core, then the $10^{-5}$/year melt probability is also the exceedance probability for these phenomena.

ANS safety acceptance criteria dictate a 95% nonexceedance probability for IB to meet these normal operation goals/requirements from the standpoint of heat flux limits. It is obviously important to demonstrate that this criterion does in fact yield the desired core melt frequency. Ideally, this should be done by evaluating CHF/FE limits in normal operation and determining the exceedance probabilities. Because of difficulties in demonstrating such low nonexceedance probabilities using statistical methodologies, it was decided to employ the worst-case style uncertainty analysis to gain insight into the feasibility of meeting ANS goals/requirements. It is recognized that in this style of analysis the nonexceedance probability is not quantified, although the analysis is generally considered to yield very conservative results and was employed in HFIR safety analysis. However, statistical methodologies would not have been abandoned for normal operation analysis with low nonexceedance probabilities and would have been pursued in future analysis. Ultimately, results from both approaches may have been useful in demonstrating that the design meets safety goals/requirements.

Inherent in the worst-case uncertainty approach is the fact that input parameter uncertainties are selected judgmentally, typically at two or three standard deviation values. The set of uncertainty values selected for this analysis are presented in Table 3.2. For comparison, uncertainty values (for parameters treated deterministically) and distributions (for parameters treated statistically) used in ANS statistical peaking factor (spf) based calculations (at 95 and 99.9% nonexceedance probability levels) are provided in Table 3.3. The basis for these parameter uncertainties is provided in ref. 1. Note that more conservative parameter uncertainties have been used in several instances in the worst-case analysis than in the spf analysis. These include the minimum channel gap width, the heat flux peaking factor assumed with the nonbond/fuel segregation fuel plate defect, and the local and streak-average power density distribution uncertainties. The use of a smaller minimum channel gap width reflects the fact that the limiting heat flux locations in the core for the G693 fuel design no longer occur near the sidewalls, where gap width variations are expected to be the smallest. The larger nonbond/fuel segregation peaking factor allows for only partially centering of the fuel meat within the fuel plate (i.e., 50% offset from perfect centering, where 100% would imply no centering). The larger power density distribution uncertainties simply reflect the judgment that these should be allowed to be a bit larger for analysis directed toward the very low $10^{-5}$ nonexceedance probability level.

Based on the parameter uncertainties given in Tables 3.2 and 3.3, hot spot (heat flux) and hot channel (bulk coolant temperature) peaking factors are provided in Table 3.4 for the 95 and 99.9% probability levels and for the worst-case situation. The hot spot peaking factor is the multiplier on the nominal, local heat flux and includes the combined effects of the uncertainties in the fuel loading (and nonbond for the very localized hot spot, i.e., for CHF and IB limits), heat flux limit correlation, the power level, and the local power density distribution. With regard to fuel loading uncertainties, heat flux peaking associated with the 2-mm-diam inspection spot is used for CHF and IB limits, whereas

**Table 3.2. Input parameter uncertainties for worst-case uncertainty analysis**

| Parameter | U factor[a] |
|---|---|
| CHF and FE correlations | 0.70 |
| IB correlation | 0.85 |
| Local power density distribution | 1.15 |
| Streak-average power density distribution | 1.10 |
| Integrated hot streak | 1.10 |
| Forced convection heat transfer correlation | 0.94 |
| Friction factor correlation | 0.90 |
| Fuel plate heated length | 1.01 |
| Channel gap width, mm | 1.016 |
| Local fuel segregation plus nonbond | 1.45 |
| Hot streak fuel segregation | 1.10 |
| Fuel beyond radial boundary | 1.02 |
| Fuel beyond axial boundary | 1.05 |
| Oxide correlation | 1.10 |
| Inlet temperature (normal operating margin) | 1.0141 |
| Inlet temperature (safety margin)[b] | 1.22 |
| Exit pressure (normal operating margin) | 0.949 |
| Exit pressure (safety margin)[b] | 0.79 |
| Power level (normal operating margin) | 1.061 |
| Power level (safety margin) | 1.04 |

[a]TASHA code uncertainty (U) factor. Multiplier on nominal value except for channel gap width, where actual value used is given.

[b]Includes deviation from normal operating point to limiting safety system set point (20%) plus uncertainties.

for the FE limit, the 2-mm-wide × 1.27-cm-long integrated inspection streak is used. This treatment is based on the assumption that exceeding CHF or IB limits can occur in a very localized "spot," whereas to exceed the FE limit, a larger "streak" area is required. The hot channel peaking factor is the multiplier on the nominal bulk coolant temperature rise along the fuel subchannels and includes the combined effects of the uncertainties in the fuel loading (integrated hot streak in Tables 3.2 and 3.3), the power level, the streak-average power density distribution, and the fuel plate heated length.

Calculations of power limits for all three sets of parameter uncertainties discussed above were performed using TASHA. The particular version of TASHA used is the most recently revised version.[10] For the 95% and 99.9% probability level cases presented below, the power limits found are higher by ~1.5 to 6% over those obtained with the previous version of the code. A word of caution is needed with regard to all power limit results where FE or CHF is used as the criterion. TASHA does not account for two-phase flow resistance effects in the calculation of subchannel velocity. Neglecting these effects is nonconservative, and therefore, power levels presented in the tables for CHF and FE will be higher than those predicted using a two-phase model. Identification of appropriate models and their incorporation was in process when the ANS program was canceled.

**Table 3.3. Input parameter uncertainties for statistical peaking factor uncertainty analysis**

| Statistical U factors[a] | | | | | |
|---|---|---|---|---|---|
| Parameter | Probability distribution | Distribution level[b] | Mean | Standard deviation | Maximum value[c] |
| IB, CHF, and FE correlations | Normal | Core | 1.0 | 0.10 | |
| Local power density distribution | Normal | Core | 1.0 | 0.03 | 1.10 |
| Streak-average power density distribution | Normal | Core | 1.0 | 0.02 | 1.05 |
| Integrated hot streak | Log-normal | Plate | 1.030 | 0.00425 | 1.10 |
| Fuel plate heated length | Normal | Plate | 1.0 | 0.0036 | 1.01 |
| Power level | Normal | Core | 1.0 | 0.018 | |

| Deterministic U factors[d] | |
|---|---|
| Parameter | U factor |
| Forced convection heat transfer correlation | 0.94 |
| Friction factor correlation | 0.90 |
| Channel gap width, mm | 1.143 |
| Local fuel segregation plus nonbond | 1.313 |
| Hot streak fuel segregation | 1.10 |
| Fuel beyond radial boundary | 1.02 |
| Fuel beyond axial boundary | 1.05 |
| Oxide correlation | 1.10 |
| Inlet temperature (normal operating margin) | 1.0141 |
| Inlet temperature (safety margin)[e] | 1.22 |
| Exit pressure (normal operating margin) | 0.949 |
| Exit pressure (safety margin)[e] | 0.79 |

[a]Uncertainty (U) factors defined in terms of probability distributions that are used to calculate spf's using Monte Carlo analysis.
[b]Distribution level indicates whether distribution applies on a plate or core-wide basis.
[c]Maximum value is the cut-off value in sampling distributions.
[d]TASHA code U factor. Multiplier on nominal value except for channel gap width, where actual value used is given.
[e]Includes deviation from normal operating point to limiting safety system set point (20%) plus uncertainties.

Tables 3.5 through 3.7 provide results of steady-state, limiting power calculations obtained using TASHA for the G693 fuel design. Power limits are presented for six time points through the cycle for each fuel element (upper and lower). Table 3.5 provides this information for the worst-case treatment of uncertainties at the normal operating margin (control plus measurement uncertainty). For comparison, Table 3.6 provides similar results for the 95% nonexceedance probability level (using the modified TASHA code as discussed previously). The results in Table 3.5 indicate that with the worst-case treatment of uncertainties, the limiting power levels for the normal operating margin, based on CHF and FE as the limits, slightly exceed the ANS design power of 303 $MW_t$. Although a nonexceedance probability cannot be quantified for these results as indicated previously, they do suggest that the ANS core melt goals/requirements with regard to normal operation based on heat flux

**Table 3.4. Hot spot and hot channel peaking factors for 95% and 99.9% probability levels, and the worst-case situation**

| Case | Peaking factor | | | |
|---|---|---|---|---|
| | Hot spot (IB) | Hot spot (CHF) | Hot spot (FE) | Hot channel |
| 95% | 1.59 | 1.59 | 1.33 | 1.10 |
| 99.9% | 1.94 | 1.94 | 1.63 | 1.12 |
| Worst-case (normal operating margin)[a] | 2.08 | 2.53 | 2.11 | 1.29 |
| Worst-case (limiting safety system set point) | 2.04 | 2.48 | 2.07 | 1.26 |

[a]Worst-case values at the normal operating margin are higher than those for the worst case at the limiting safety system set point because of differences in set point and control uncertainties.

**Table 3.5. Limiting power levels ($MW_t$) based on worst-case uncertainties at operating margin for each fuel element**

| Time (d) | Incipient boiling | | Critical heat flux | | Flow excursion | |
|---|---|---|---|---|---|---|
| | Lower | Upper | Lower | Upper | Lower | Upper |
| 0 | 304 | 406 | 367 | 491 | 365 | 484 |
| 1 | **302**[a] | 404 | **365** | 488 | **363** | 480 |
| 4.25 | 305 | 397 | 367 | 477 | 364 | 470 |
| 8.5 | 336 | 412 | 404 | 493 | 392 | 489 |
| 12.75 | 313 | 382 | 382 | 461 | 385 | 455 |
| 17 | 345 | **258** | 420 | **314** | 428 | **319** |

[a]The lowest power level over all time steps is in bold type.

limits may be feasible. However, as conditions (i.e., flux-to-flow, inlet coolant temperature, and core exit pressure) move toward LSSS values, satisfying these goals/requirements will depend on the frequency (probability) of experiencing conditions between the normal operating window and LSSS (or safety margin) values; that is, the core melt probability ≈ probability of event (or exposure to some set of conditions) × the CHF/FE exceedance probability at those conditions (assuming CHF/FE exceedance leads to fuel melting and that it propagates through core and leads to a core melt). Note that at the LSSS conditions, the ANS power requirements/goals (348 $MW_t$) are met at a 99.9% probability level (Table 3.7). Thus, at LSSS conditions, it has been argued that the ANS core melt goals/requirements can be met with a $10^{-3}$ CHF/FE exceedance probability, where it was assumed that the probability of reaching these conditions is sufficiently small.

It is obvious that the parameter uncertainty values used in this analysis were still very preliminary at this stage in the project. In addition, the fuel design was still evolving, as were other aspects of the reactor design. "Uncertainties" in the parameter uncertainty values themselves have been

**Table 3.6. Limiting power levels ($MW_t$) at 95% uncertainty levels at operating margin for each fuel element using the modified TASHA code**

| Time (d) | Incipient boiling | | Critical heat flux | | Flow excursion | |
|---|---|---|---|---|---|---|
| | Lower | Upper | Lower | Upper | Lower | Upper |
| 0 | 413 | 553 | 544 | 725 | 528 | 699 |
| 1 | **412**[a] | 552 | **541** | 721 | **525** | 695 |
| 4.25 | 417 | 544 | 547 | 708 | 530 | 683 |
| 8.5 | 463 | 549 | 598 | 742 | 569 | 708 |
| 12.75 | 431 | 523 | 570 | 683 | 562 | 660 |
| 17 | 474 | **352** | 630 | **468** | 628 | **465** |

[a]The lowest power level over all time steps is in bold type.

**Table 3.7. Limiting power levels ($MW_t$) at 99.9% uncertainty levels for each fuel element using the modified TASHA code**

| Time (d) | Critical heat flux | | | | Flow excursion | | | |
|---|---|---|---|---|---|---|---|---|
| | Operating margin | | Safety margin | | Operating margin | | Safety margin | |
| | Lower | Upper | Lower | Upper | Lower | Upper | Lower | Upper |
| 0 | 504 | 675 | 452 | 604 | 505 | 668 | 439 | 581 |
| 1 | **501**[a] | 671 | **450** | 602 | **501** | 664 | **436** | 578 |
| 4.25 | 506 | 658 | 454 | 590 | 505 | 651 | 440 | 568 |
| 8.5 | 559 | 665 | 500 | 620 | 545 | 678 | 474 | 590 |
| 12.75 | 527 | 636 | 471 | 569 | 534 | 630 | 464 | 548 |
| 17 | 580 | **432** | 519 | **386** | 596 | **443** | 517 | **383** |

[a]The lowest power level over all time steps is in bold type.

addressed in three series of sensitivity calculations; the "base" calculations for the sensitivity calculations are the worst-case analyses at the normal operating margin (Table 3.5). In the first series of sensitivity calculations, the hot spot peaking factor was increased by 20% (selected arbitrarily simply to produce a perturbation; resulting limiting powers can be scaled to produce results at perturbation values other than +20%). Similarly, the hot channel peaking factor was increased by 20% in the second series; for the third series the channel gap width was decreased from 1.016 to 0.889 mm (12.5%). The results of these calculations are presented in Table 3.8 in terms of a percentage drop in the maximum power from the base calculations. Note the significant power penalty (benefit) associated with a decrease (increase) in the channel gap width.

With regard to the evolution of the fuel design, the results in Tables 3.5 through 3.7 indicate that if the most power-limiting time/location could be eliminated (e.g., with further refinement of the fuel grading) and was no longer the most limiting, then the next most limiting time/location typically allows a 15% greater power level. Since the G693 fuel design was optimized to minimize fuel

**Table 3.8. Sensitivity of limiting power levels based on IB, CHF, and FE limits with worst-case uncertainties at operating margin to perturbations in hot spot and channel peaking factors and channel gap width**

| Parameter variation | Percentage power change | | |
|---|---|---|---|
| | Incipient boiling | Critical heat flux | Flow excursion |
| Hot spot (+20%) | −9.3 | −8.6 | −4.3 |
| Hot channel (+20%) | −11 | −11 | −13 |
| Channel gap width (−12.5%) | −14 | −14 | −16 |

centerline temperature and oxide growth and not heat flux limits, some significant improvements may be possible. However, optimal fuel grading to satisfy all constraints would likely be some compromise.

Calculated limiting power margins for ANS at normal, steady-state conditions based on worst-case uncertainties can be compared to those for HFIR (using HFIR uncertainties). The HFIR ratios of the calculated maximum limiting power to the actual normal operating power level are ~1.5 (IB) and 1.6 (CHF), whereas for ANS these ratios are less than 1 and just slightly above 1, respectively. Obviously, there are differences in design between the two reactors and differences in assumed uncertainties, but this comparison indicates what has been recognized for some time: that the design and treatment of uncertainties for the ANS must be done optimally to reach ANS design goals/requirements.

## 3.3 TAILS TRUNCATION OF THERMAL LIMIT UNCERTAINTY PROBABILITY DISTRIBUTIONS

As indicated above, the safety criterion for normal operation is a core melt probability of $10^{-5}$/year. A problem one is faced with in calculating such very low exceedance probabilities for CHF and FE is that the extreme lower tail (e.g., $3\sigma$ or more below the mean) of their uncertainty probability distributions, which are typically extrapolated based on a normal distribution, becomes important. In this extrapolated tail region, calculated values of CHF and FE that are physically impossible can result. For example, for a given set of fluid conditions, a calculated CHF value may lie below the IB heat flux or the heat flux at which the fuel plate surface temperature just equals the saturation temperature ($T_{wall} = T_{sat}$). Unfortunately, there are obviously uncertainties associated with calculation of IB and $T_{wall} = T_{sat}$ limits as well, which complicate the determination of what value of CHF constitutes an impossible value. As explained below, the lower tail of the CHF and FE uncertainty distributions can be revised to incorporate those of IB and $T_{wall} = T_{sat}$ to provide lower bounds to calculated heat fluxes that are based on physical reality to the extent possible.

As already mentioned, the method for truncating the tails of the CHF and FE uncertainty distributions utilizes IB and $T_{wall} = T_{sat}$ limits to provide a lower bound for CHF and FE limits, and doing so incorporates uncertainties in all thermal limit calculations. To begin an explanation of the method, consider the two illustrative uncertainty probability density functions (PDF) or distributions (assumed to be normal) in Fig. 3.1, one for IB and the other for CHF. These could apply for a given set of fluid conditions. Hence, for these conditions, the heat flux limits for IB and CHF at their means and $1\sigma$, $2\sigma$, and $3\sigma$ values from their means are given in Table 3.9 (values selected solely for

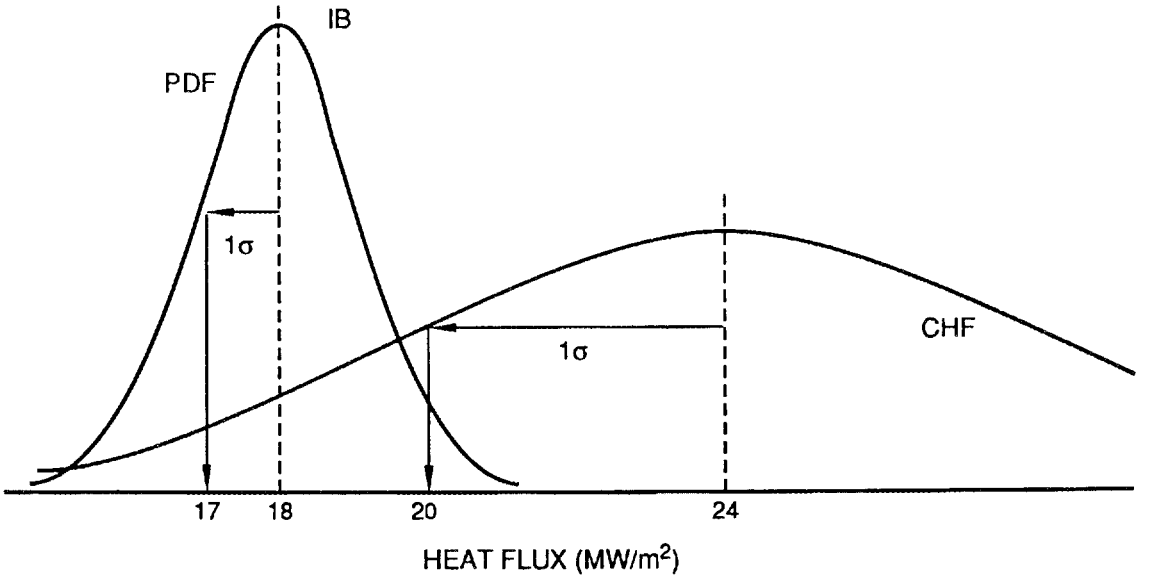


**Fig. 3.1. Illustrative probability density functions for incipient boiling and critical heat flux.**

**Table 3.9. Illustrative heat flux limits for incipient boiling and critical heat flux at their means and 1σ, 2σ, and 3σ values from their means**

| Distribution value | Heat flux limits ($MW/m^2$) | |
|---|---|---|
| | Incipient boiling | Critical heat flux |
| Mean | 18 | 24 |
| Mean–1σ | 17 | 20 |
| Mean–2σ | 16 | 16 |
| Mean–3σ | 15 | 12 |

illustration purposes). Figure 3.1 shows how the values at 1σ from the mean, for example, were determined. Notice in the table that the calculated limit values for CHF for the mean and 1σ are larger than IB values, but at 2σ they become equal, and at 3σ the IB value is larger. Thus, at the 2σ heat flux it can be said that there is a 97.5% probability that CHF will not be exceeded, and the same can be said for IB. Although it is obviously expected that CHF will occur at a significantly higher heat flux than IB, it cannot be said that at 2σ the distributions exhibit impossible behavior based *only* on the fact (or using the conservative criterion) that IB must be exceeded before CHF. However, at 3σ (and in fact above 2σ), the distributions lead one to say that there is a greater probability for exceeding CHF than for IB, which is impossible. Thus, beyond the 2σ value, one can use heat flux limit values obtained from the IB probability distribution instead of those obtained from the CHF distribution. This fact means effectively that a revised, "integrated" CHF probability distribution, as illustrated in Fig. 3.2, can be used.

A number of questions have been raised about this proposed method. First, the true CHF probability distribution would not have an abrupt change in it as the revised one has at the point where the IB distribution is integrated into the CHF distribution. However, at this time a probability distribution quantifying the difference between IB and CHF limits does not exist. The feasibility of developing such a distribution has not been given serious thought, nor have attempts been made to estimate the costs to develop it (e.g., experiments designed specifically for this purpose) along with the

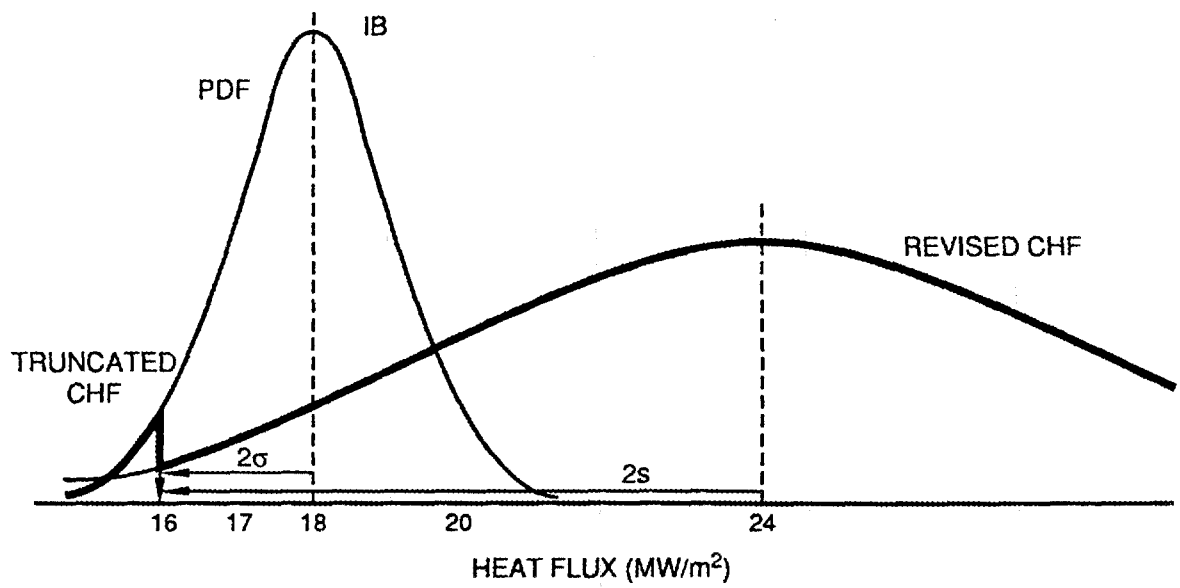


**Fig. 3.2. Illustrative probability density functions for incipient boiling and revised critical heat flux based on incipient boiling.**

potential benefits it could provide over the method proposed here. It should be clear that the mean difference between IB and CHF limits changes as the fluid conditions change. Thus, the point at which the CHF distribution is revised with the IB distribution (i.e., $2\sigma$ in the example above) changes. A second question one can raise concerns the fact that we are assuming that the IB probability distribution is "correct" in the lower tails region and that the CHF distribution is incorrect. It can be simply argued that the anomaly of the predicted IB heat flux being greater than the CHF heat flux arises because of the (assumed) inability to model CHF limits as well as IB limits. Neither distribution is "wrong"; they just reflect how well one is modeling CHF and IB limits. However, it must be remembered that extrapolated values (i.e., beyond the range of existing data) are being used in the extreme lower tail of these distributions, which obviously elicits questions of accuracy.

Another question that was not directed specifically to this proposed method but that must be addressed is the supposition that the CHF probability distribution is really the CHF given IB (or CHF/IB) distribution. Although it is clear that for a given set of fluid conditions IB must occur before CHF does, this fact does not imply that the CHF uncertainty probability distribution, as defined here, is really the CHF given IB distribution. To understand this, refer to Fig. 3.3, which shows illustrative IB and CHF PDFs. Assume that these PDFs taken together do not exhibit anomalous behavior in terms of the probability of exceeding CHF being greater than that for IB (or, that the CHF distribution has been appropriately revised if they did originally exhibit this anomalous behavior). Thus, for these distributions the exceedance probability for IB will always be greater than (or equal to) that for CHF. In Fig. 3.3 at the mean of the IB distribution, $\overline{q''_{IB}}$, there is a 50% probability that IB will be exceeded and a 20% probability for CHF (the mean of the CHF distribution is denoted as $\overline{q''_{CHF}}$ in Fig. 3.3). Note that at $\overline{q''_{IB}}$, there is a 50% probability that IB is *not* exceeded, while at the same time the probability that CHF is exceeded is 20%. Since IB must be exceeded for CHF to be exceeded, IB is exceeded with a 100% probability in the 20% probability fraction that CHF is exceeded. In the 80% probability fraction that CHF is not exceeded, IB is exceeded with a 37.5% probability; that is, using the rule of Bayes:[11]

$$\begin{aligned} P_{IB} = 0.5 &= P_{IB/CHF} \times P_{CHF} + P_{IB/CHF'} \times P_{CHF'} , \\ 0.5 &= 1 \times 0.2 + P_{IB/CHF'} \times 0.8 , \\ P_{IB/CHF'} &= 37.5\% , \end{aligned} \tag{1}$$

where CHF′ ≡ complement of CHF (i.e., CHF not exceeded).

These results can be illustrated in a Venn diagram by considering a given sample size. Figure 3.4 presents a Venn diagram containing expected results for a sample size of 100. From the diagram one can determine $P_{IB/CHF'}$ as:

$$\begin{aligned} P_{IB/CHF'} &= 30/(100 - 20) , \\ P_{IB/CHF'} &= 37.5\% . \end{aligned} \tag{2}$$

One can also determine $P_{CHF/IB}$ from the diagram as:

$$P_{CHF/IB} = 20/50 = 40\% . \tag{3}$$

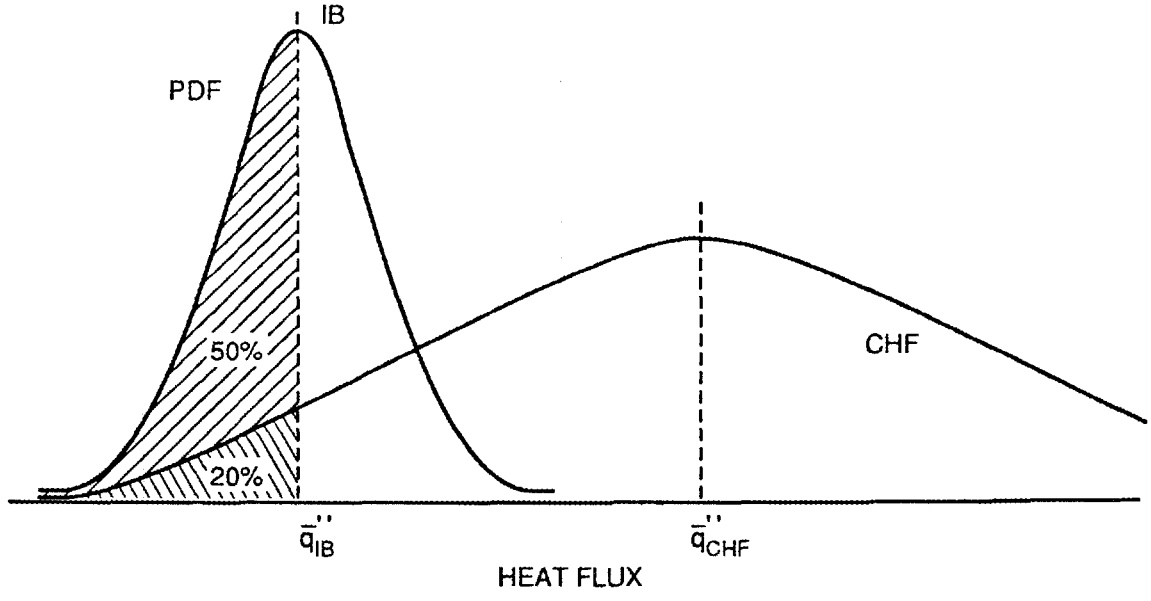


**Fig. 3.3. Illustrative probability density functions for incipient boiling and critical heat flux, showing a 20% exceedance probability for critical heat flux at $\bar{q}''_{IB}$.**

It is clear that because this value is different from the 20% value obtained from the CHF uncertainty probability distribution, the CHF distribution does not represent the CHF/IB distribution. From the Venn diagram and using the rule of Bayes, one can write (with IB′ denoting IB not exceeded):

$$P_{CHF} = P_{CHF/IB} \times P_{IB} + P_{CHF/IB'} \times P_{IB'} ,$$

$$P_{CHF} = 20/50 \times 50/100 + 0/100 \times 50/100 , \qquad (4)$$

$$P_{CHF} = 20/100 \text{ or } 20\% .$$

This result checks with the result from our CHF distribution.

Implementation of this method for tails truncation in Monte Carlo–based uncertainty analysis can be accomplished only when performing "full" Monte Carlo analysis, that is, when sampled values from the input parameter uncertainty probability distributions are used directly in the thermal analysis code. This method cannot be applied when Monte Carlo analysis is used to calculate statistical peaking factors, which is done independent of the thermal code. The reason for this is that to truncate the tails of the thermal limit correlations, one must know at what heat flux the nonexceedance probability of the bounding limit correlation (e.g., IB) exceeds that of the "primary" limit correlation (e.g., CHF). However, when using statistical peaking factors, one can at least use the limit (e.g., CHF or IB) with its associated peaking factor at the probability level of interest that gives the highest heat flux (i.e., largest margin to a limit violation).

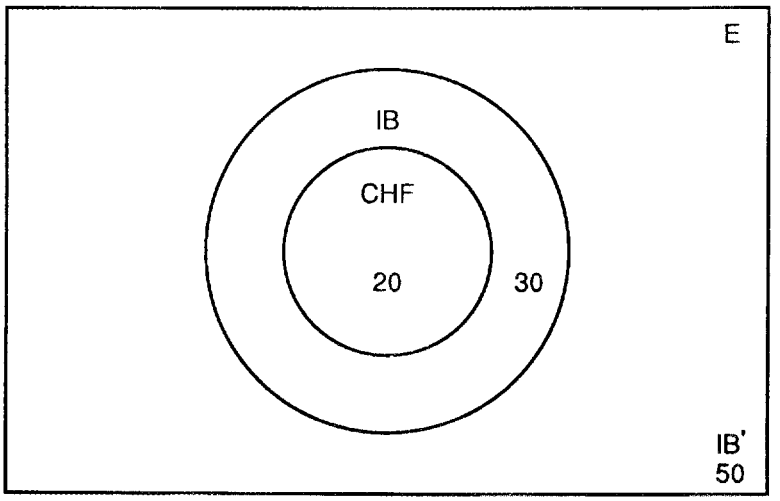


**Fig. 3.4. Illustrative Venn diagram consistent with results in Fig. 3.3, showing expected sample results for incipient boiling, critical heat flux, and no boiling.** E denotes the entire event space.

In performing "full" Monte Carlo analysis, for each trial in the simulation, thermal limit distributions would be sampled using the same random value, thereby providing the same probability level on each. The resulting heat fluxes would then be compared, and the highest flux would be used in the trial. The process would result effectively in the use of a revised primary limit (e.g., CHF) correlation uncertainty probability distribution as shown previously in Fig. 3.2.

Although this method has been presented assuming CHF to be the primary limit distribution and IB the bounding distribution, other combinations of limit correlations can be used. That is, IB and/or $T_{wall} = T_{sat}$ could serve as bounding correlations to either CHF or FE; or $T_{wall} = T_{sat}$ could be used to bound IB. The procedure to be used is the same and would be done twice, for example, when $T_{wall} = T_{sat}$ is used to bound IB, which is used to bound CHF. Other, independent checks on the fuel centerline temperature and oxide temperature drop would have to be performed to ensure that their appropriate limits are not exceeded; this is no problem to do.

The actual benefit of employing tails truncation in terms of maximum power limit gain will depend on several factors: the difference between the mean limits based on CHF or FE versus IB and $T_{wall} = T_{sat}$ (the smaller the difference, the greater the possible truncation), the difference between the uncertainties ($\sigma$), and the nonexceedance probability level considered (as the level increases, truncation becomes more significant). Of course, if one did develop thermal limit uncertainty probability distributions through the ANS thermal-hydraulic experimental and analytical efforts that do not exhibit the anomalous behavior described above, no truncation would be required. No effort to implement this method has been undertaken; it would be implemented in the integrated SAMPLE/TASHA code (ANS statistical, steady-state thermal, fuel element model).

# 4. REFLECTOR VESSEL COMPONENT COOLING

## 4.1 REFLECTOR VESSEL

The reflector vessel tank (RVT) of the ANS reactor surrounds the core pressure boundary tube (CPBT) and contains heavy water coolant and RV components. These components are the experimental facilities that collect or utilize the neutrons produced in the reactor for research and other applications. They consist of seven beam tubes, one through-tube, one hot source, two cold sources, one slant beam tube, two slant cold guide tubes, and several irradiation facilities. Figure 4.1 is a horizontal cross-sectional view of the RV two-element core design, showing the beam tubes, the cold sources, the hot source, and the through-tube. The RV is submerged in a light water pool, also shown in Fig. 4.1.

Heavy water is pumped into the RV for cooling. This flow, however, is not enough to induce sufficient forced convection cooling over the RV components. Forced convection cooling is required for the two-element core design of the ANS reactor to cool portions of the components that are near the reactor core. In particular, the beam tubes are the closest components to the reactor core, have the highest cooling requirements, and need forced convection cooling.

This section describes these components, analyzes their cooling requirements, and describes the different cooling alternatives considered and the selection process of a cooling scheme.

Most of these calculations are for the two-element core design of the ANS reactor, which uses highly enriched uranium (HEU) with 93% enrichment. This core has an active core volume of 67.6 L and an outside radius of 253 mm. One of the latest design changes of the ANS reactor was to change the fuel from HEU to a reduced enrichment of 50%. This reduced enrichment core comprises three concentric core elements (Fig. 1.1) with an active volume of 83 L and outside radius of 300 mm, both larger than the two-element core. Figure 4.2 shows a cross-sectional view of the RV and components for the three-element core. The outside diameter of the RV is 1.75 m for both the two- and the three-element core.

Heat deposition rates on the RV components and, therefore, cooling requirements are higher for the two-element core. The portions of the beam tubes closest to the core have the largest heating rates, about 16 W/g in the two-element core versus 7.3 W/g in the three-element core with fuel overlap and 5.4 W/g in the three-element core without overlap. (The three-element core design with overlap is that presented in Fig. 1.1. A second three-element design did not allow the upper and middle elements to overlap, as shown in Fig. 4.3.) Forced convection cooling is required for the components of the two-element core as will be shown in the following sections.

## 4.2 REFLECTOR VESSEL COMPONENTS

The components inside the reflector vessel that require cooling are seven beam tubes, two cold sources, one hot source, one through-tube, one slant beam tube, two slant cold guide tubes, and several irradiation facilities. The dimensions of the first eleven components (four different types of components) are given in Table 4.1. They are shown in Fig. 4.1.

As the components closest to the reactor core, the beam tubes have the highest heat deposition rates and, therefore, the highest cooling requirements. Consequently, most of the calculations have been performed for the beam tubes. If satisfactory cooling of the beam tubes can be achieved, the remaining components can be cooled also.

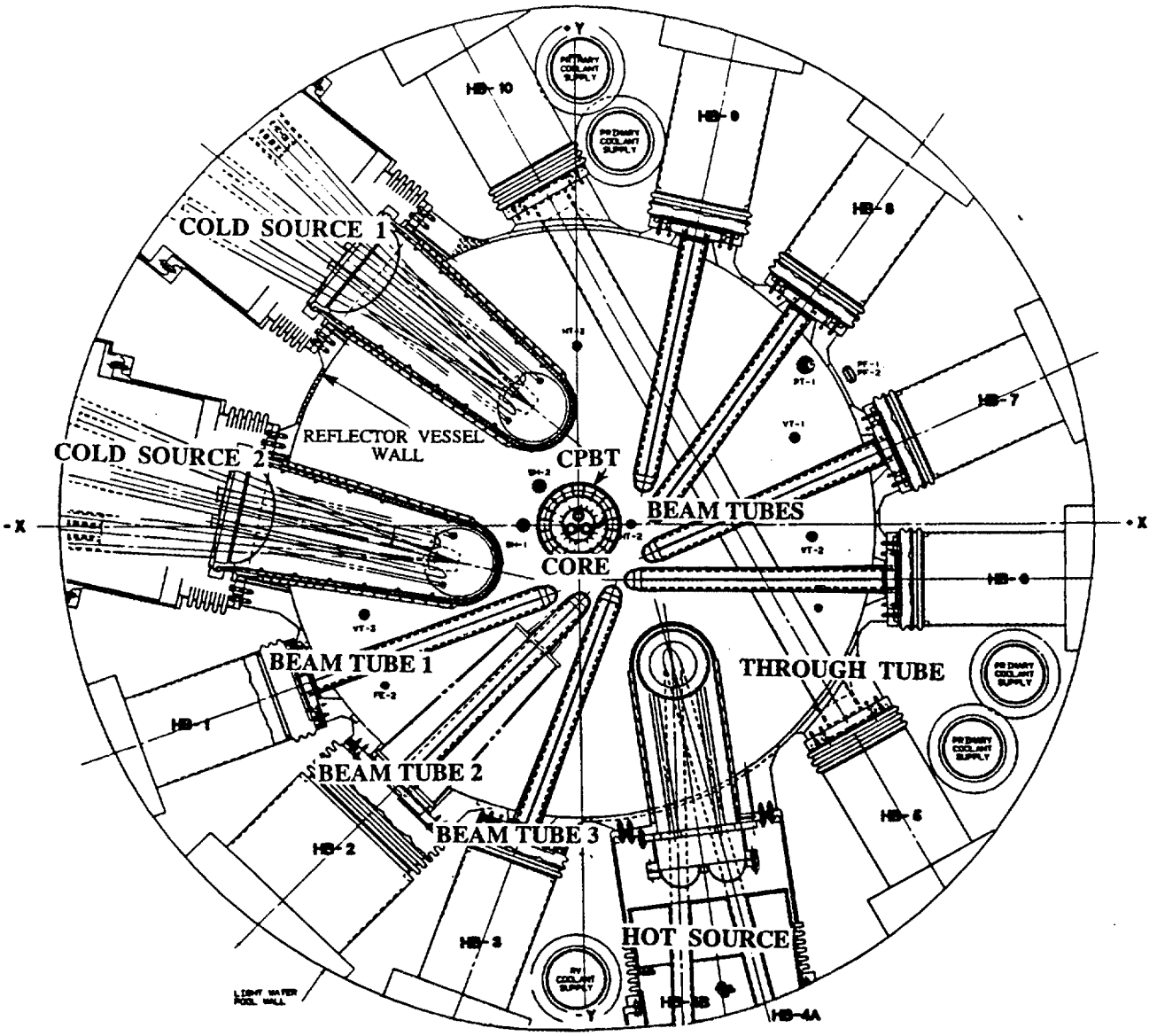


**Fig. 4.1. Horizontal cross-sectional view of the reflector vessel (two-element core).**

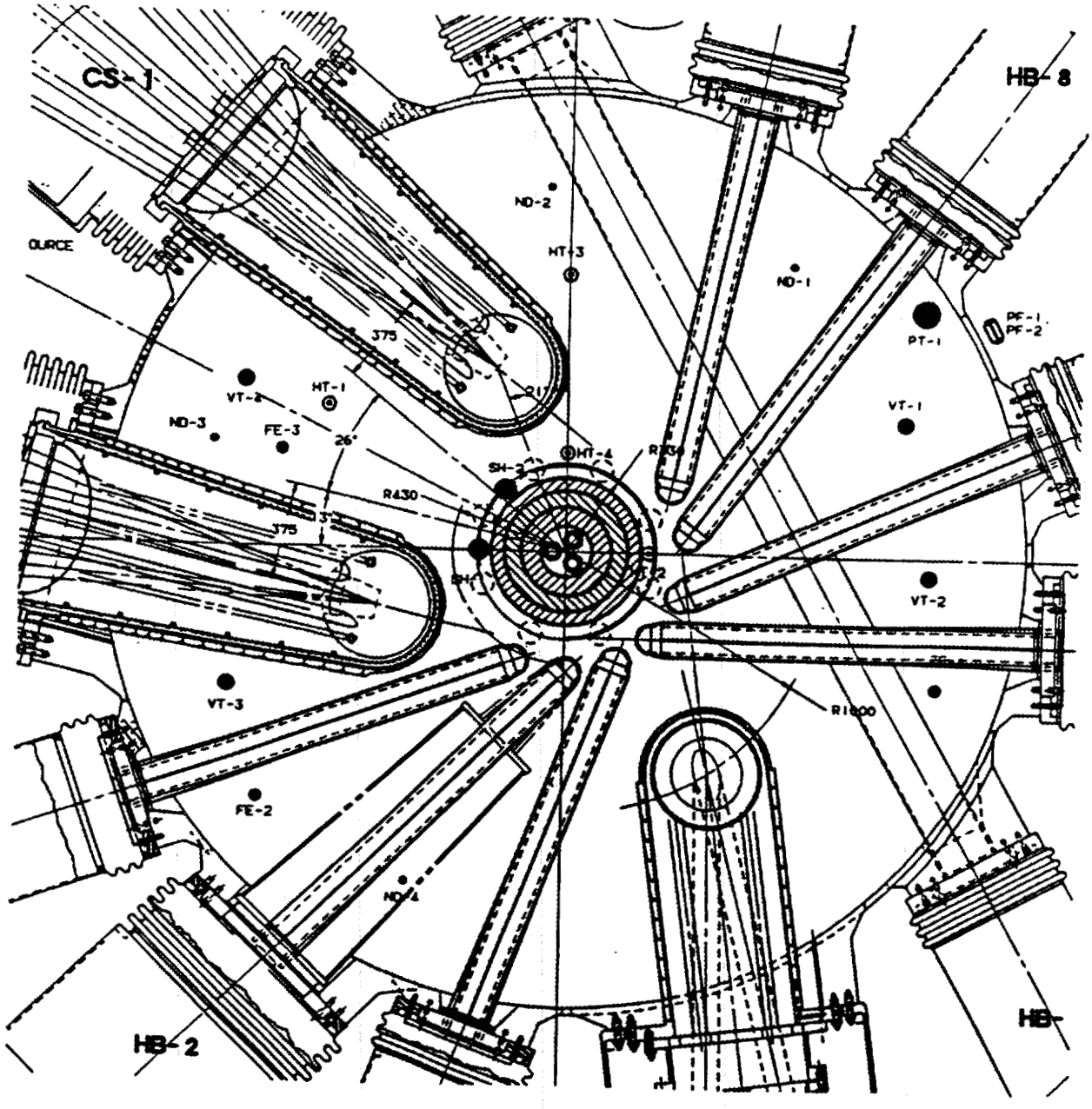


**Fig. 4.2. Horizontal cross-sectional view of the reflector vessel (three-element core).**

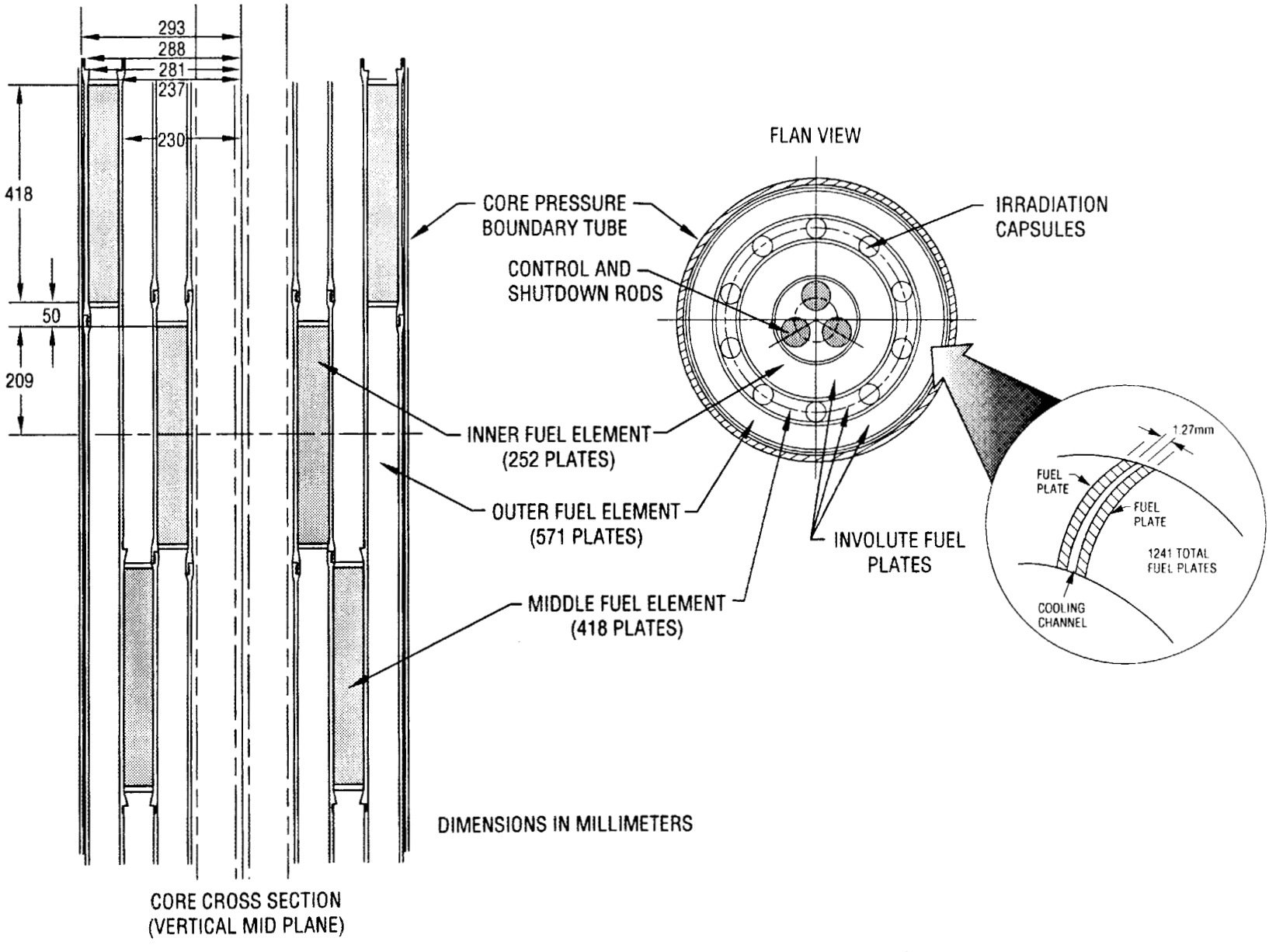


**Fig. 4.3. Three-element core design without overlap.**

**Table 4.1. Dimensions of the components in the reactor vessel**

| Component | Inside diameter (mm) | Thickness (mm) | | | Gap thimble/ shroud (mm) | | Total length (m) |
|---|---|---|---|---|---|---|---|
| | | Thimble | Tip | Shroud | Min. | Max. | |
| Beam tubes (7) | 100 and 200 | 14.1 | 3.5 | 3 | 3.3 | 3.18 | 1.542 |
| Through-tube | 196 | 8 | | 3 | 3 | 15 | 3.469 |
| Hot source | 455 | 6 | 6 | 3 | 16.5 | 16.5 | 1.100 |
| Cold source (2) | 498–659 | 9.5 | 6.3 | 0.8 | 25.4 | 28.7 | 1.478 |

All of the components are made of aluminum. Other materials, like Zircaloy, have been considered and studied but were not selected for final consideration. Both materials, aluminum and Zircaloy, have low neutron-absorbing characteristics, an essential condition because these components need to collect as many neutrons as possible for use in the experimental facilities of the ANS reactor.

## 4.3 COOLING SCHEMES

A total of 15 cooling schemes were investigated, and they are summarized in Fig. 4.4. Scheme 15 includes 6 different subschemes, for a total of 20 different cooling schemes. All the concepts have been applied to a beam tube in Fig. 4.4, but they apply to the other components as well.

A brief description of each cooling scheme follows. The first three schemes and scheme 13 are variations of the same concept, consisting of a shroud or a jacket surrounding the component to be cooled. Heavy water flow is pumped into the space between the shroud and the component. The first two schemes have open shrouds at the tip of the beam tube, while scheme 3 has a closed shroud. In scheme 1, flow from the RV is pumped into the gap between the shroud and the component, exiting the RV at the base of the tube. In scheme 2 flow from outside the RV is pumped into the shroud/component gap and is discharged into the RV. In scheme 3 the shroud/component gap is divided into two interconnected parts, and flow from outside the RV is pumped into one of these two parts and leaves through the second part. This coolant is independent of the coolant inside the RV. Schemes 1 and 2 require a piping system either to collect coolant from the gap (scheme 1) or to pump coolant into the gap (scheme 2). Scheme 3 requires two piping systems: one to pump coolant in, the other to collect the coolant. Scheme 13 is like scheme 1 but uses helium inside the beam tube, providing some cooling through this helium and reducing the cooling required by the forced heavy water flow into the shroud/component gap.

Schemes 4 and 5, variations of a similar concept, consist of shrouds around each component like the previously described schemes, but with all the shrouds interconnected with an internal minishroud. This minishroud could be close to the core (scheme 4) or close to the RV wall (scheme 5). The coolant is pumped into the minishroud and from there into each component's shroud. This scheme eliminates the need for a separate piping system into each component's shroud. (The same RV pumps will be used for these schemes).

Schemes 6 and 10 are similar. Scheme 6 employs piping, and scheme 10 employs sprinklers that will force coolant into the components or portions of the component that require forced convection cooling.

Scheme 7 requires a large flow of coolant pumped into the RV so that a constant coolant bulk velocity of 1 m/s is achieved everywhere inside the RV.

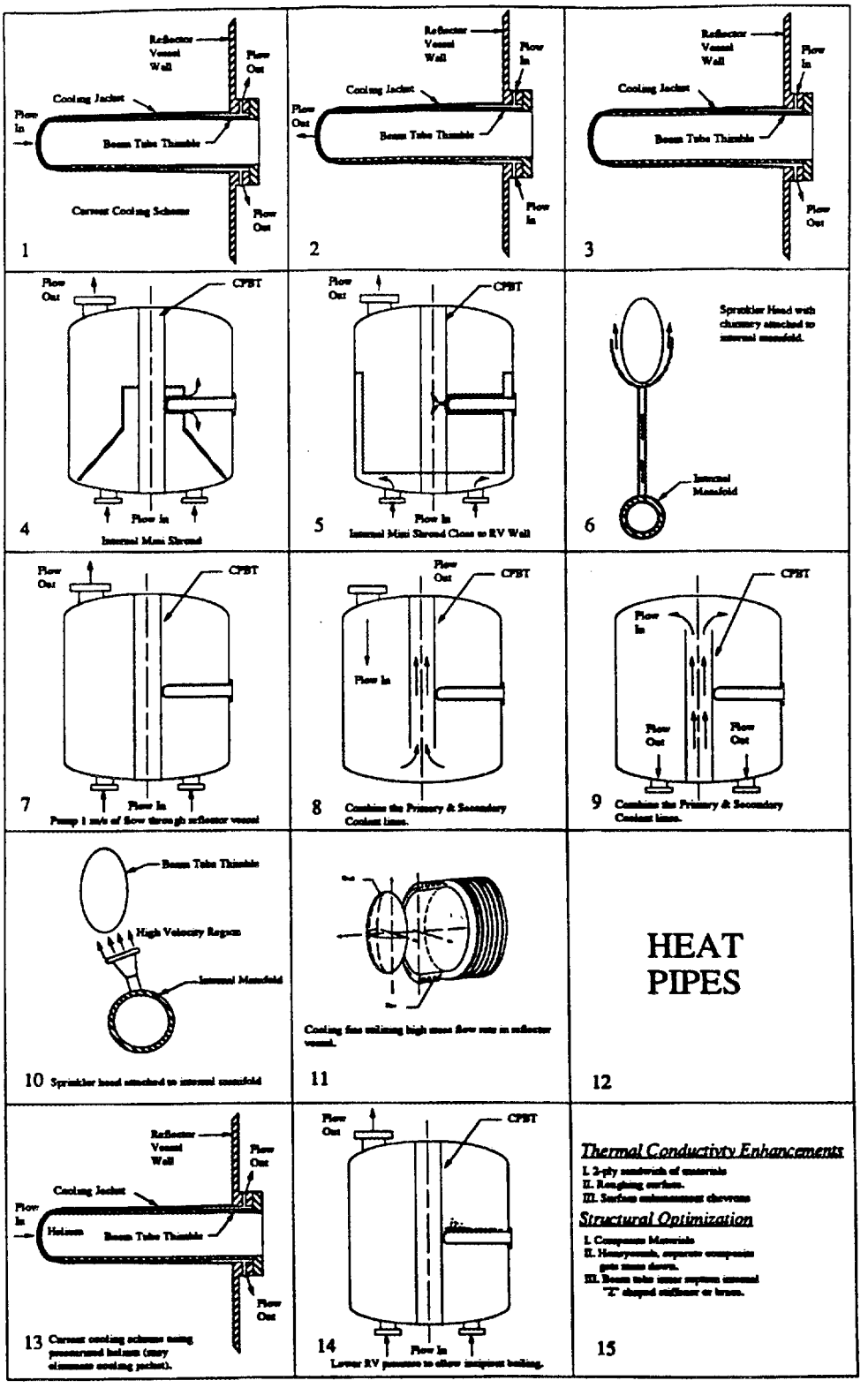


**Fig. 4.4. Components cooling schemes.**

Schemes 8 and 9 are variations of the same concept, both connecting the primary (reactor core) and secondary (RV) coolant systems. Normally the ANS reactor has separate core and RV coolant systems with two different sets of pumps: the primary for the reactor core and the secondary for the RV. In scheme 8 the coolant enters the RV first and the core afterwards. In scheme 9 the coolant enters the core first and the RV afterwards.

Schemes 11 (fins), 12 (heat pipes), 14 (nucleate boiling), and 15 (several enhancements and optimizations) are self-explanatory.

Based on thermal-hydraulic, safety, and design considerations, schemes 1, 2, 3, and 5 were selected for further consideration. A final selection of one of these four schemes has not been completed. The other schemes were eliminated for different reasons. Scheme 4 was eliminated because this minishroud is too close to the core, would be heated extensively, and would have to be replaced often. Scheme 5 (minishroud near the RV) offers the same features as scheme 4 and is a better concept because it is far away from the core. Schemes 6 and 10 complicate RV intervals and introduce additional heating because of the extra material of these concepts. This extra material is very close to the core also, increasing the overall cooling requirements.

Scheme 7 (1-m/s bulk velocity in the RV) was eliminated because it is difficult to achieve such large flow rates in the RV. Furthermore, it was determined that 1-m/s bulk flow inside the RV is not sufficient to cool all the components. In particular, the beam tubes require higher velocities.

Schemes 8 and 9 were eliminated for the following reasons: (a) the RV would have to be listed as a class I pressure vessel, (b) scheme 8 introduces a higher pressure in the RV, requiring the thickness of the beam tubes to be increased, increasing their heat deposition rates and cooling requirements, (c) scheme 9 introduces a higher bulk temperature in the RV, and (d) the components would became part of the primary pressure boundary, which could reduce the availability of the reactor (because of required component testing, etc.).

Scheme 11 (cooling fins) was eliminated because fins are less effective when heat is generated internally.

Scheme 12 (heat pipes) was eliminated because it complicates the experimental system and introduces concerns about safety and reliability. The heat pipe concept introduces a foreign substance into the reactor vessel that could leak or get activated.

Scheme 14 (nucleate boiling) was eliminated because it requires a reduction in the pressure, thus introducing a larger $\Delta P$ with respect to the primary system. Also, nucleate boiling introduces neutron flux variations that may not be acceptable for some experiments.

Scheme 15 variations were not studied in detail because they introduce unacceptable complications to the RV components.

## 4.4 DECAY HEAT AFTER A SCRAM IN THE REFLECTOR VESSEL TANK COMPONENTS

A preliminary determination of the amount of decay heat generated after a scram in the RVT components (beam tubes, cold sources, etc.) has been completed. The decay heat after a scram determines the flow rates required to cool these components after reactor shutdown.

Heat loads taken from two ANS progress reports[12,13] were used for this purpose (more recent heat loads are presented in ref. 14 but were not available at the time these calculations were performed). The total heat load for each component at full reactor power was split into three different contributions: (a) prompt neutrons and gammas, (b) fission products, and (c) activated Al-28 decay. Table 4.2 shows these contributions (in % of the total heat load at full power) for five different components in the RVT. More than half of the total heat load is produced by the prompt neutrons and

**Table 4.2. Heat load by contribution (in %) for different RVT components at full power**

| Component | Prompt neutron and gamma | Fission products | Al-28 decay | Total | Observations |
|---|---|---|---|---|---|
| Beam tube | 51 | 7 | 42 | 100 | |
| Cold sources | 33 | 6 | 61 | 100 | Largest Al-28 contribution |
| Large slant beam tube | 50 | 3 | 47 | 100 | |
| Cold source guides | 52 | 2 | 46 | 100 | |
| Reflector tank | 67.6 | 0.4 | 32 | 100 | Smallest fission product and Al-28 contribution |

*Source:* ref. 12.

gammas. After the scram, this contribution disappears almost instantly, and the other two contributions (fission products and Al-28) provide the decay heat load. Of these two contributions, the Al-28 decay is more significant, with up to 61% of the total heat load produced in the cold sources. Of the components listed in Table 4.2, the RVT appears to have the lowest contributions from both fission products and Al-28 decay.

Table 4.3 shows the heat load at full power for beam tube 1 (HB-1) by contribution and as a function of the distance from the front cap of the beam tube. These distances are proportional to the distance to the core. This table was generated from the data provided in the Idaho National Engineering Laboratory (INEL) section of ref. 13. Table 4.3 shows that about half of the total heat load is produced by the prompt neutrons and gammas, with the highest value (55.7%) at the end of the beam tube and the lowest (46.8%) in the segment between 1.026 and 1.164 m from the front cap. No clear trend of the variation of this contribution with position can be observed from the data. For the second contribution, fission products, there is a clear trend with distance to the core: the closer to the core, the higher this contribution. The largest value of this contribution is 14% at the front cap, and the lowest, 0.4%, at the end of the beam tube. Finally, the third contribution, Al-28 decay, appears to increase with distance, but decreases again in the last two segments of the beam tube. The lowest value of this contribution is at the front cap with 34.65%, and the highest in the segment 1.026 to 1.164 m with a value of 52.7%.

The variation with time of the two contributions to the decay heat after a scram is well known, and it is given in Table 4.4. The decay heat from the fission products drops faster during the first seconds after a scram than the decay heat from the activated aluminum-28, which decays with a half-life of 2.25 min (135 s).

Two specific cases were studied. The first was for the front cap of the beam tube (Table 4.3). This point has the highest fission product contribution to the total heat load with a value of 14%. Table 4.5 shows the amount of decay heat generated after a scram for this case. At 1 s after the scram, the decay heat is about 35% of the full power before the scram. At 1 min after the scram, the decay heat is about 26% of the full power before the scram. At 5 min after the scram, the decay heat is about 8%, and at 10 min only 2%.

The second case studied was for the cold sources (Table 4.2). The cold sources have the highest contribution to the heat load from the activated aluminum-28 with a value of 61%. Table 4.6 shows

**Table 4.3. Full power heat load by contribution (in %) as a function of position for beam tube HB-1**

| Position (mm) | Prompt neutron and gamma | Fission products | Al-28 decay | Total | Observations |
|---|---|---|---|---|---|
| Front cap | 51.4 | 14.0 | 34.6 | 100 | Largest fission products contribution; lowest Al-28 contribution |
| 0–50 | 53.2 | 12.0 | 34.8 | 100 | |
| 50–150 | 53.6 | 9.4 | 37.0 | 100 | |
| 150–250 | 53.4 | 6.6 | 40.0 | 100 | |
| 250–350 | 51.8 | 5.2 | 43.0 | 100 | |
| 350–450 | 50.3 | 4.0 | 45.7 | 100 | |
| 450–550 | 50.7 | 3.0 | 46.3 | 100 | |
| 550–650 | 48.9 | 2.4 | 48.7 | 100 | |
| 650–750 | 47.3 | 1.8 | 50.9 | 100 | |
| 750–888 | 48.2 | 1.3 | 50.5 | 100 | |
| 1026–1164 | 46.8 | 0.5 | 52.7 | 100 | Lowest prompt n and $\gamma$ contribution; largest Al-28 contribution |
| 1164–1302 | 50.2 | 0.5 | 49.0 | 100 | |
| Remainder (end) | 55.7 | 0.4 | 43.9 | 100 | Lowest fission product contribution; largest prompt n and $\gamma$ contribution |
| Overall | 51.7 | 7.8 | 40.5 | 100 | |

*Source:* ref. 13.

the amount of decay heat after scram for this case. The decay heat of this case is larger than for the previous case shown in Table 4.5. At 1 s after the scram, the decay heat is about 61% of the full power before the scram; at 1 min, 45%; at 5 min, 13%; and at 10 min, 3%.

The results from Tables 4.5 and 4.6 indicate that more decay heat is produced in those components with the largest contribution to the total heat load from the activated aluminum-28. From the data investigated, the cold sources appear to have the largest contribution to the total heat load from the Al-28. If overheating of the cold sources needs to be prevented after a scram, the pumping system should be designed to provide enough flow (or pressure) to remove the decay heat given in Table 4.6.

**Table 4.4. Fraction of the initial power as a function of time after scram**

| Time | | Fission products | Al-28 decay |
|---|---|---|---|
| (s) | (min) | | |
| 0 | | 1.0 | 1.0 |
| 1 | | 0.06 | 0.995 |
| 10 | | 0.0571 | 0.95 |
| 20 | | 0.05437 | 0.903 |
| 30 | 0.5 | 0.052 | 0.857 |
| 60 | 1 | 0.048 | 0.735 |
| 90 | 1.5 | 0.046 | 0.63 |
| 120 | 2 | 0.044 | 0.54 |
| 150 | 2.5 | 0.042 | 0.463 |
| 180 | 3 | 0.041 | 0.397 |
| 240 | 4 | 0.026 | 0.292 |
| 300 | 5 | 0.0243 | 0.214 |
| 600 | 10 | 0.021 | 0.046 |

**Table 4.5. Decay heat as a function of time for the end cap (tip) of beam tube HB-1**

| Time | | Prompt n and γ (%) | Fission products (%) | Al-28 decay (%) | Total (%) |
|---|---|---|---|---|---|
| (s) | (min) | | | | |
| 0 | 0 | 51.4 | 14.0 | 34.6 | 100.0 |
| 1 | | | 0.84 | 34.48 | 35.32 |
| 10 | | | 0.8 | 32.92 | 33.72 |
| 20 | | | 0.76 | 31.3 | 32.06 |
| 30 | 0.5 | | 0.73 | 29.7 | 30.43 |
| 60 | 1 | | 0.67 | 25.47 | 26.14 |
| 90 | 1.5 | | 0.64 | 21.83 | 22.47 |
| 120 | 2 | | 0.62 | 18.71 | 19.33 |
| 150 | 2.5 | | 0.59 | 16.04 | 16.63 |
| 180 | 3 | | 0.57 | 13.76 | 14.33 |
| 240 | 4 | | 0.36 | 10.12 | 10.48 |
| 300 | 5 | | 0.34 | 7.42 | 7.76 |
| 600 | 10 | | 0.29 | 1.6 | 1.89 |

**Table 4.6. Decay heat as a function of time for the cold sources**

| Time (s) | Time (min) | Prompt n and γ (%) | Fission products (%) | Al-28 decay (%) | Total (%) |
|---|---|---|---|---|---|
| 0 | | 33 | 6 | 61 | 100.0 |
| 1 | | | 0.4 | 60.7 | 61.1 |
| 10 | | | 0.34 | 57.95 | 58.29 |
| 20 | | | 0.32 | 55.1 | 55.42 |
| 30 | 0.5 | | 0.31 | 52.3 | 52.61 |
| 60 | 1 | | 0.29 | 44.84 | 45.13 |
| 90 | 1.5 | | 0.28 | 38.43 | 38.71 |
| 120 | 2 | | 0.26 | 32.94 | 33.20 |
| 150 | 2.5 | | 0.25 | 28.24 | 28.49 |
| 180 | 3 | | 0.25 | 24.22 | 24.47 |
| 240 | 4 | | 0.16 | 17.81 | 17.97 |
| 300 | 5 | | 0.15 | 13.05 | 13.20 |
| 600 | 10 | | 0.13 | 2.81 | 2.94 |

## 4.5 COOLING SCHEME 1—OPEN SHROUD AROUND THE BEAM TUBE

### 4.5.1 Feasibility

The beam tubes can be cooled using scheme 1, an open shroud with pressure differentials of less than 30 kPa between the reflector tank and the shroud exit. These calculations assumed a maximum heat generation of 16.82 W/g for the tip, transition region, and beginning of the thick portion of the beam tube. The calculations used a beam tube thickness of 14.1 mm, a tip thickness of 3.5 mm, a transition region 38 mm long, and a cooling jacket thickness of 3 mm. The total length of the beam tube is 1.555 m (Fig. 4.5). The maximum allowed temperature for the aluminum was assumed to be 120°C.

Two options were investigated and found feasible. For the first option, a cooling flow rate of 7.08 kg/s per beam tube is required, resulting in a total pressure drop of 17.2 kPa. The following geometry is used: a cooling jacket with an elliptical entrance orifice of semiaxes 34.4 and 68.8 mm, an initial gap between the tip and the entrance orifice of 22 mm, a gap between the jacket and the transition region varying from 13.8 mm at the entrance to 3.25 mm at the exit, and a gap between the beam tube body and the jacket increasing uniformly from 3.25 to 31.3 mm at the beam tube exit. The water increases its temperature by 5.75°C through the beam tube.

In the second option, the pressure drop through the cooling jacket is increased to 28.3 kPa, the elliptical entrance orifice semiaxes are reduced to 30 and 60 mm, the initial gap between the tip and the entrance orifice is reduced to 19.5 mm, the gap between the jacket and the transition region varies between 13.6 and 3 mm, and the gap between the jacket and beam tube body is kept constant at 3 mm for the first 884 mm of the tube and increased uniformly to 15 mm for the last 580 mm of the beam

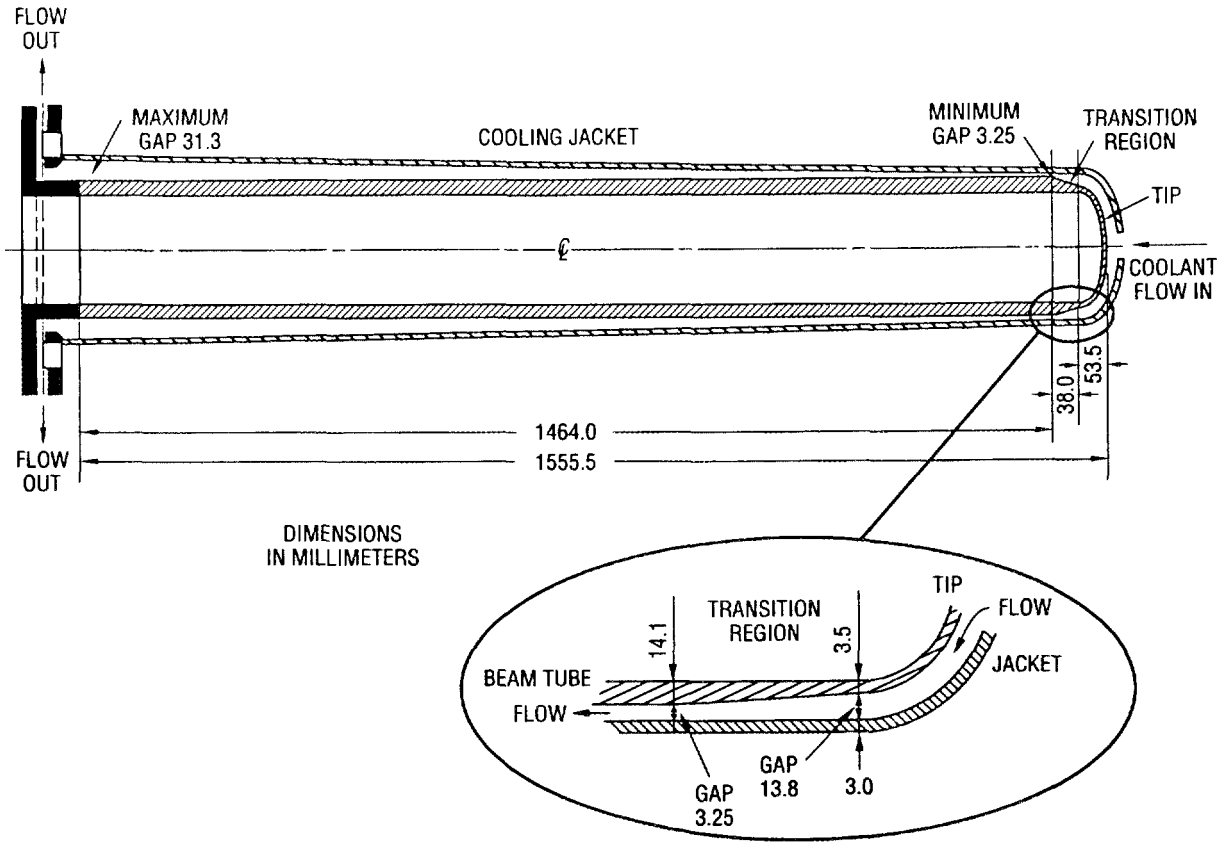


**Fig. 4.5. Sectional view of the beam tube and cooling jacket and detail of the transition region.**

tube. In this case, the water mass flow rate required is 6.52 kg/s, and the water temperature increases by 6.25°C.

### 4.5.2 Maximum Cooling Capability of the Beam Tube with Shroud Under Natural Convection Conditions

Calculations were performed to quantify the maximum amount of heat that can be removed from the beam tube with shroud when the pressure in the reflector tank is lost and only natural convection applies to the outside and inside surfaces of the cooling shroud. When the reflector tank pressure is lost, the forced water flow through the gap between the cooling shroud and the beam tube is also lost.

It is very important to avoid vaporization of the water inside the water gap because if this occurs, the heat transfer between the beam tube and the cooling shroud will be significantly reduced.

#### Assumptions

The pressure in the reflector tank was assumed to be 0.360 MPa, which is the pressure at the cooling shroud exit. The boiling temperature of the heavy water at this pressure is 140.96°C.

The calculations were performed for the initial, thick portion of the beam tube, where the maximum heat is generated. The thickness of the beam tube is 14.1 mm, and both the water gap and the cooling shroud thickness are assumed to be 3 mm.

These calculations assumed that *no heat is generated in the water* between the shroud and the beam tube. The heat generated in the beam tube wall is transferred to the water gap. From the water gap, this heat is transferred to the inside surface of the cooling shroud, and the heat from there, together with the heat generated in the cooling shroud wall, is transferred to the water outside of the cooling shroud by natural convection. The heat is transferred from the beam tube surface to the inside surface of the cooling shroud by natural convection through the water in the 3-mm gap.

Of the total heat generated in the beam tube, 81% is generated in the beam tube wall, and the remaining 19% in the cooling shroud. At full reactor power, the maximum heat generation rate in this region (front of the beam tube) is $q''' = 16.82$ W/g, resulting in heat fluxes of $q'' = 578$ kW/m$^2$ for the beam tube surface and $q'' = 136$ kW/m$^2$ for the cooling shroud surface.

**Calculational Method**

The outside dimensions of the cooling shroud are 140.2 mm wide (horizontal) and 240.2 mm long (vertical). The outside diameter of the shroud used in the calculations is the horizontal width (140.2 mm) or an equivalent dimension obtained by the equation (ref. 15, p. 392):

$$1/\text{Lequiv} = 1/\text{Lhor} + 1/\text{Lvert} \quad . \tag{5}$$

For the average heat transfer coefficient outside horizontal cylinders, with the Grashof number between $10^3$ and $10^9$ and the Prandtl number >0.5, Eq. (7-25) from ref. 15 is used:

$$\text{Nu} = 0.53(\text{GrPr})^{0.25} \quad , \tag{6}$$

where

Nu = Nusselt number,
Gr = Grashof number,
Pr = Prandtl number.

Alternatively, for vertical plates, with GrPr > $10^9$, the following equation (taken from ref. 15, p. 393) is used with the equivalent dimension:

$$\text{Nu} = 0.021\ (\text{GrPr})^{0.4} \quad . \tag{7}$$

For free convection in enclosed spaces, with GrPr between $3 \times 10^5$ and $7 \times 10^9$, Eq. (7-35) from ref. 15 is used:

$$\text{Nu} = 0.069\ \text{Gr}^{1/3}\text{Pr}^{0.407} \quad . \tag{8}$$

Because the Grashof number is dependent on the $\Delta T$, several iterations are required to obtain a solution.

**Results**

If the limiting condition is the boiling temperature of the water (140.96°C) inside the water gap, and if the temperature of the water in the RVT is 66°C, natural convection can remove a total heat flux outside the shroud of $q'' = 42$ kW/m$^2$, or 5.87% of the value at full power.

If the limiting condition is the temperature of the aluminum (120°C), and the RVT water is 66°C, the maximum heat flux that can be removed by natural convection outside the shroud is $q'' = 21.4\ kW/m^2$, or 3% of the value at full power.

If the temperature of the RVT water increases to 88°C, the maximum heat flux outside the shroud that can be removed by natural convection without boiling the water inside the cooling shroud is $17.2\ kW/m^2$, or 2.42% of the value at full power.

## 4.6 MISCELLANEOUS COOLING CALCULATIONS

This section discusses heat transfer calculations along unshrouded components in order to evaluate the feasibility of other cooling schemes (like schemes 6 and 10) and the possibility of cooling by natural convection.

### 4.6.1 Heat Transfer Coefficients Needed for Cooling Unshrouded Beam Tubes (Aluminum Temperature Limit 120°C)

Heat fluxes and heat transfer coefficients have been calculated along the beam tube length without a shroud to study the different cooling needs of different portions of the beam tube. Calculations performed in Sect. 4.5.1 indicate that the beam tube can be cooled using an annular forced flow with the shroud around the beam tube (scheme 1).

The following assumptions were used in the following calculations:

1. No heat is removed from inside the beam tubes (vacuum inside).
2. The beam tube material is aluminum.
3. The thickness of the beam tube is 14.1 mm.
4. The thickness of the beam tube tip is 3.5 mm.
5. The maximum temperature allowed for aluminum is 120°C.
6. The coolant temperature is 66°C.
7. The maximum heat generation (at the front of the beam tube) is 16.82 W/g.

In these calculations, the total length of the beam tube was divided into segments (slices) 2 mm long. For each segment, the distance to the core center and the heat generation rate $q'''$ (W/g) was calculated. Then, the total heat generated in the volume of each segment, the heat flux $q''$ through the outside surface of the segment, and the temperature drop across the tube wall were calculated. The $\Delta T_h$ available for heat transfer is calculated by subtracting the $\Delta T$ across the wall from the total available $\Delta T$, which is 54°C (120° – 66°). Finally the heat transfer coefficient, h, is calculated by dividing the heat flux $q''$ by the $\Delta T_h$. The results of these calculations are given in Table 4.7.

Table 4.7 shows that at about 370 mm from the tip of the beam tube, an h of 5 $kW/(m^2 \cdot °C)$ is required for cooling, a value that can be obtained by cross-flow forced convection at a velocity of 1 m/s. At a distance of 722 mm from the tip, the h required is 1.5 $kW/(m^2 \cdot °C)$, a value that can be obtained by natural convection. Therefore, about half of the beam tube (from 722 mm to the end) can be cooled by natural convection. The remaining length of the beam tube, including the beam tube tip, requires forced convection. The largest heat transfer coefficient calculated was 20.5 $kW/(m^2 \cdot °C)$ at the front of the beam tube.

Since the largest cooling requirements are at the front of the beam tube, two additional calculations were performed for that region by varying some input parameters. These calculations are shown in Table 4.8. In one calculation, the maximum temperature allowed for the Al was increased to 140°C,

**Table 4.7. Calculation of convective heat transfer coefficients along unshrouded beam tube length**

| | Distance to core center, in mm | | | | |
|---|---|---|---|---|---|
| | 0 (Tip) | 0 (Front) | 370 | 722 | 1464 (End) |
| $q'''$, W/g | 16.82 | 16.82 | 6.43 | 2.2 | 0.16 |
| $q''$, kW/m$^2$ | 159 | 578 | 221.2 | 76.3 | 5.6 |
| $\Delta T_h$, °C | 52.5 | 28.2 | 44.1 | 50.6 | 53.75 |
| h, kW/(m$^2$ · °C) | 3 | 20.5 | 5 | 1.5 | 0.103 |
| Convection needed | Forced <1-m/s cross-flow | Forced 3.5-m/s annular | Forced 1-m/s cross-flow | Natural | Natural |

**Table 4.8. Heat transfer coefficients at the front of the beam tube for different conditions**

| | | | |
|---|---|---|---|
| Maximum aluminum temperature, °C | 120 | 140 | 140 |
| Coolant temperature, °C | 66 | 50 | 50 |
| $q'''$, W/g | 16.82 | 16.82 | 11.0 |
| $q''$, kW/m$^2$ | 578 | 578 | 378 |
| $\Delta T_h$, °C | 28.2 | 64.2 | 71.5 |
| h, kW/(m$^2$ · °C) | 20.5 | 9 | 5.3 |
| Convection needed | Forced 3.5-m/s annular | Annular | Forced 1.1-m/s cross-flow |

and the coolant temperature decreased to 50°C. The resulting h with these conditions is 9 kW/(m$^2$ · °C), a value large enough to require forced annular flow. The second calculation used the same temperatures of the preceding calculation and a heat generation rate $q'''$ of only 11 W/g. The resulting h is 5.3 kW/(m$^2$ · °C), a value that can be obtained by forced cross-flow convection at a velocity of 1.1 m/s.

Again, all these calculations are one dimensional, with variation of the heat transfer coefficients *only* along the length of the beam tube. However, there are variations in other directions (radial or azimuthal) because of other factors not considered here. These factors are different distances to the core center for points of the same segment or slice (resulting in different heat generation rates), different curvature of the beam tube along the perimeter, and azimuthal variation of the natural convection and cross-flow forced convection heat transfer coefficients. These factors need to be considered in future calculations.

There is one important point to be made about the enhanced cooling capabilities of the beam tube without the shroud under decay heat conditions. Assuming that natural convection will be the only method of removing decay heat after scram, Table 4.7 shows that a heat flux of 76.3 kW/m$^2$ can be removed under natural convection. Comparing this heat flux with the heat flux at the front of the beam

tube at full power (578 kW/m$^2$), the first value is 13% of the value at full power of the reactor. Under the same conditions (maximum temperature of the aluminum 120°C) but with the shroud around the beam tube, natural convection could only remove 3% of the value at full power (Sect. 4.5.2).

### 4.6.2 Unshrouded Cold Source Heat Transfer Coefficients

Calculations of the heat transfer coefficients required for cooling along the surface of the cold source without the shroud have been completed. All of these calculations used small surface elements and assumed 120°C maximum aluminum temperature and a 66°C bulk coolant temperature. The closest point to the reactor core center (at a distance of 500 mm) is at the tip of the cold source thimble (which is 6.4 mm thick) and has a $q''' = 11$ W/g and a heat flux of $q'' = 184$ kW/m$^2$ and requires an h of 3.65 kW/(m$^2$ · °C), which can be obtained by cross-flow forced convection at 1 m/s. The maximum required h was calculated to be h = 3.7 kW/(m$^2$ · °C) on the thick (9.53-mm) wall of the thimble, where $q''' = 7$ W/g and $q'' = 180$ kW/(m$^2$ · °C). Natural convection with h = 650 W/(m$^2$ · °C) or less can be achieved at points situated 1.4 m or more from the core center. Axial conduction was found to be important at the junction of the 6.4- and 9.35-mm-thick walls.

The cooling requirements of the cold source are lower than the cooling requirements of the beam tube.

### 4.6.3 Unshrouded Hot Source Heat Transfer Coefficients

Calculations of the heat transfer coefficients required for cooling along the surface of the hot source thimble without the shroud are presented. All of these calculations used small surface elements and assumed a maximum temperature of the aluminum of 120°C and a bulk temperature of the water of 66°C.

The closest point to the reactor core center at a distance of 767 mm has the highest $q'''$ (5.67 W/g), the highest $q''$ (90 kW/m$^2$), and the highest required h with a value of 1.7 kW/(m$^2$ · °C). Cross-flow forced convection at 0.35 m/s is required to achieve this heat transfer coefficient.

Natural convection with h = 670 W/(m$^2$ · °C) or less is required for points 1.05 m or more from the core center.

The cooling requirements of the hot source are lower than those of the cold source.

### 4.6.4 Heat Transfer Coefficient Needed for Cooling the Reflector Vessel Components (Aluminum Temperature Limit 149°C)

Heat transfer coefficients have been recalculated for the beam tube, cold source, and hot source thimbles with new temperature limits for the aluminum. The maximum aluminum temperature has been raised to 149°C with the additional limitation that the aluminum surface temperature in contact with the coolant is 130°C or below. This limitation is needed to avoid boiling of the water in contact with the aluminum surface. The temperature of 130°C is the saturation temperature of $D_2O$ at 0.26 MPa.

These new calculations include a coolant temperature reduced from 66 to 50°C and heat generation rates for the beam tube HB-1[13] multiplied by a factor of 1.3. The correction factor of 1.3 includes conversion from beginning of cycle to end of cycle and other uncertainties in the calculated values of ref. 13. The maximum heat generation rate now at the tip and front of the beam tube is 12.3 × 1.3 = 16 W/g, slightly less than the value of 16.82 W/g used in previous calculations. The heat generation rates of ref. 13, corrected with the 1.3 factor, appear to be smaller than the values previously used for the beginning portion of the beam tube and larger for the rest of the beam tube. For instance, at the

end of the beam tube, the heat generation rate used previously was only 0.16 W/g. The new value (including the 1.3 factor) is 0.63 W/g, four times higher.

Values of the heat transfer coefficients along the beam tube using the new calculational assumptions are given in Table 4.9. Values calculated previously, using $T_{MAX,AL}$ = 120°C, $T_{D_2O}$ = 66°C, and a different $q'''$ (higher at the front of the beam tube and lower for the rest) are given in Table 4.7. In comparing the tables, it can be seen that the required heat transfer coefficient at the beam tube tip is reduced from 3.0 to 1.9 kW/(m$^2$ · °C). Also, the required heat transfer coefficient at the front of the beam tube (thick wall next to the tip) gets reduced from 20.5 to 7.4 k/(m$^2$ · °C). The front of the beam tube is the point with the highest cooling requirements, and it requires forced convection with a velocity higher than 1 m/s (either annular or cross-flow). Forced convection cross-flow at 1 m/s is calculated to be needed at a point 150 mm from the tube front (before it was required at a point 370 mm farther down the beam tube). Similarly, natural convection starts at a point 650 mm, while before it started at a point 722 mm from the front (Table 4.7).

The maximum thickness of the beam tube with a heat generation rate of $q'''$ = 16 W/g, which can be cooled using natural convection with the new temperature limits, is now about 3 mm (with the previous assumptions this thickness was 1.8 mm). Also, the maximum thickness of the beam tube with a heat generation rate of $q'''$ = 16 W/g, which can be cooled using forced convection cross-flow at 1 m/s, is now 10.2 mm (with the previous assumptions this thickness was 5.5 mm).

Heat transfer coefficients have also been recalculated for the cold source and the hot source using the new maximum temperatures for the Al (149°C, 130°C at the surface) and the colder $D_2O$ temperature (50°C). The same values of the heat generation rates used previously have been employed. The required heat transfer coefficient for the beam tube, the cold source, and the hot source are given in Table 4.10 for the point with the highest cooling requirements (highest required heat transfer coefficient). The new calculational assumptions reduced the highest heat transfer coefficient considerably for the beam tube. The reduction was not as large for the cold or hot sources (only 35%). Forced convection is still required at these points for either the beam tubes, cold sources, or hot source.

Heat transfer coefficients required for cooling the through-tube have also been calculated. The hottest point was assumed to have a heat generation rate of $q'''$ = 14 W/g with a resulting heat flux of $q''$ = 300 kW/m$^2$. The temperature gradient across the 8-mm-thick wall for this heat flux is only 7.1°C; therefore, the limiting temperature of 130°C at the aluminum surface applies. With coolant at 50°C, the $\Delta T$ available for heat transfer is 80°C, and the resulting heat transfer coefficient is h = 3.7 kW/(m$^2$ · °C). This heat transfer coefficient can be obtained with forced convection at less than 1 m/s. If annular flow (cooling jacket) is used with a gap of 3 mm, the Dittus-Boelter correlation[16] yields a flow velocity of 0.47 m/s, equivalent to a mass flow rate of 1.04 kg/s of $D_2O$ at 50°C.

### 4.6.5 Summary of Cooling Requirements for Unshrouded Components

Even using the higher aluminum temperature of 149°C (with 130°C at surfaces in contact with coolant) and the lower coolant temperature of 50°C, forced convection is still required for some portions (the closest to the reactor core) of the RV components.

### 4.6.6 Three-Dimensional Factors in Beam Tube Cooling

Most of the heat transfer coefficient calculations along the thermal beam tube without the shroud were one-dimensional, with the axial distance along the tube being the only independent variable considered. Also, all of these calculations considered only radial heat conduction. In principle, these assumptions are reasonable because the beam tube has a large length (about 1.555 m) compared to its

**Table 4.9. Convective heat transfer coefficients along unshrouded beam tube using the new calculational assumptions**

| | Distance to beam tube tip, in mm | | | | |
|---|---|---|---|---|---|
| | 0 (Tip) | 0 (Front) | 150 | 650 | 1464 (End) |
| $q'''$, W/g | 16 | 16 | 11.6 | 3.5 | 0.63 |
| $q''$, kW/m$^2$ | 151 | 550 | 400 | 120 | 21.6 |
| $\Delta T_{wall}$, °C | 1.5 | 24.5 | 18.8 | 5.5 | 1.0 |
| $T_{max}$, °C | 131.5 | 149.0 | 148.8 | 135.5 | 131.0 |
| $T_{surf}$, °C | 130 | 124.5 | 130 | 130 | 130 |
| $\Delta T_h$, °C | 80 | 74.5 | 80 | 80 | 80 |
| h, kW/(m$^2$ · °C) | 1.9 | 7.4 | 5 | 1.5 | 0.270 |
| Convection needed | Forced cross-flow | Forced annular or cross-flow | Forced 1- m/s cross-flow | Natural | Natural |

[a]Maximum temperature of Al 149°C with maximum limit of 130°C at boiling surfaces.

axes (64 and 114 mm). Nevertheless, these assumptions need to be checked. Therefore, more detailed calculations considering three-dimensional factors were completed. The factors investigated are different curvatures of the beam tube, different distances to the core center for points of the same axial segment, azimuthal dependence of the heat transfer coefficient, and the possibility of axial conduction.

The effect of different curvatures around the beam tube periphery was quantified to be less than 10%. The effect of different distances to the core center for points of the same axial segment is negligible. The azimuthal dependence of the local heat transfer coefficient is very important. The ratio of the maximum heat transfer coefficient to the minimum can be as high as 5 under natural convection conditions and around 2.5 for cross-flow forced convection. These ratios are dependent on the Reynolds number, the Grashof number, and other variables like the roughness of the surface and the level of turbulence. Finally, axial conduction is important only if two regions with very different thicknesses or different thermal conductivities are in close contact together. This is not the case for the beam tubes. In conclusion, the only important three-dimensional factor is the azimuthal variation of the heat transfer coefficient. Further studies in this area are warranted.

### 4.6.7 Beam Tube Maximum Wall Thickness for Natural Convection Cooling

The maximum wall thickness that can be cooled by natural convection or by cross-flow forced convection at 1 m/s has been calculated. Under natural convection conditions [h = 1.5 kW/(m$^2$ · °C)], the maximum wall thickness of the beam tube with $q''' = 16.82$ W/g is 1.8 mm (using 120°C maximum Al temperature and 66°C coolant temperature). Under cross-flow forced convection conditions with 1-m/s velocity [h = 5 kW/(m$^2$ · °C)], the maximum wall thickness is 5.5 mm (using the same $q''' = 16.82$ W/g, the same maximum temperature for the Al of 120°C, and coolant temperature of 66°C).

**Table 4.10. Highest required heat transfer coefficients calculated for the beam tubes, cold sources, and hot source using different calculational assumptions**

| Temperatures | | Beam tubes | | | Cold sources | | | Hot source | | |
|---|---|---|---|---|---|---|---|---|---|---|
| $T_{MAX,AL}$ (°C) | $T_{D_2O}$ (°C) | $q'''$ (W/g) | $q''$ (kW/m$^2$) | h [kW/(m$^2$ · °C)] | $q'''$ (W/g) | $q''$ (kW/m$^2$) | h [kW/(m$^2$ · °C)] | $q'''$ (W/g) | $q''$ (kW/m$^2$) | h [kW/(m$^2$ · °C)] |
| 120 | 66 | 16.82 | 578 | 20.5 | 7 | 181 | 3.7 | 5.67 | 90 | 1.7 |
| 149 (130 at surface) | 50 | 16 | 550 | 7.4 | 7 | 181 | 2.2 | 5.67 | 90 | 1.1 |

### 4.6.8 Zircaloy Beam Tube Cooling

Cooling requirements for Zircaloy beam tubes have been evaluated based on a thimble wall 10.5 mm thick and a tip wall 2.5 mm thick. The Al beam tubes required a thimble wall 14.1 mm thick and a tip wall 3.5 mm thick. Zircaloy heat generation rates from ref. 16 were used in these calculations. All of the heat generation rates have been multiplied by a correction factor of 1.3 to account for end-of-life conditions and other uncertainties. For the front portion of the thimble wall, the heat generation rate was taken from HB-1, which is the beam tube with the highest heat generation in this region, with a value of $q''' = 7.20 \times 1.3 = 9.37$ W/g. For the beam tube tip, the heat generation rate used was from HB-8 (which is the beam tube with the largest $q'''$ for the tip region) with a $q''' = 10.47 \times 1.3 = 13.61$ W/g. A value of 6.64 Mg/m$^3$ was used for the Zr density and a value of 17.1 W/(m · °C) for the Zr thermal conductivity. The calculated heat fluxes for the Zr thimble and tip are 599 and 226 kW/m$^2$ respectively. Using a temperature difference between the surface wall (at 130°C) and coolant (at 50°C) of 80°C, the resulting heat transfer coefficients are 7.5 and 2.8 kW/(m$^2$ · °C) at the thimble and tip, respectively. Both the heat fluxes and the heat transfer coefficients for the Zr beam tube are a little higher than the values previously calculated for the aluminum beam tube using a $q'' = 16$ W/g. Consequently, the Zr beam tubes with these thicknesses have higher cooling requirements than the Al beam tubes.

The temperature gradient across the thimble wall is 201°C, resulting in a maximum temperature of the Zircaloy of 331°C. The temperature gradient across the tip wall is 17°C, resulting in a maximum temperature of 147°C. The 331°C temperature value is below the maximum acceptable temperature for Zircaloy of 371°C. These calculations were repeated using a lower Zr density of 6.477 Mg/m$^3$ and a higher thermal conductivity of 20.77 W/(m · °C). (These values vary depending on the Zircaloy used.) The resulting heat fluxes were 585 kW/m$^2$ and 220.4 kW/m$^2$ at the thimble and tip, respectively. The resulting heat transfer coefficients are 7.3 and 2.755 kW/(m$^2$ · °C) at the thimble front and tip, respectively. The new heat transfer coefficient at the thimble front is slightly smaller than the value obtained for the Al beam tube with a value of 7.4 kW/(m$^2$ · °C). The new heat transfer coefficient at the tip of the Zr beam tube is still larger than the value of 1.9 kW/(m$^2$ · °C) obtained in Sect. 4.6.4 for the Al beam tube. The temperature gradient across the thimble is now 165°C, resulting in a maximum Zr temperature of 295°C.

The total heat generated in the Zr beam tube HB-1 is 124 kW. This value is for the thimble only (no shroud) and using the higher density of Zr (6.6 Mg/m$^3$) and the $q'''$ from ref. 17 multiplied by the 1.3 factor. For comparison, the Al beam tube HB-1 generates 147 kW (using the value for $q'''$ for Al multiplied also by 1.3). Total heat generation varies from tube to tube. Beam tube HB-1 appears to have the largest total heat generation. Beam tube HB-8 appears to have the lowest heat generation, with a value of 114 kW for the Zr tube and 140 kW for the Al tube. The total heat generated in the Zr beam tubes is less than that in the Al beam tubes.

### 4.6.9 Cooling the Beam Tube by Nucleate Boiling

An evaluation of heat removal by boiling on the beam tube surface (without shroud) has been completed. For Al beam tubes with a thickness of 14.1 mm, a $\Delta T$ across the beam tube wall of 24.5°C, and the Al maximum temperature of 149°C, the corresponding surface temperature is 124.5°C. For stable boiling, the surface temperature of the beam tube should be around 10°C higher than the saturation temperature of the boiling fluid. Thus, a saturation temperature of 114.5°C should be used, which corresponds to a saturation pressure of only 160 kPa (1.58 atm). This pressure in the reflector tank vessel is too low, well below the design pressure of 300 kPa, and not practical to obtain.

Therefore, from the thermal/pressure point of view, boiling on the surface of the Al beam tubes is not a practical alternative.

If Zr beam tubes are used with a maximum temperature of 371°C inside, the maximum surface temperature is 170°C. If a saturation temperature of 160°C is used, the saturation pressure is 606 kPa (6 atm). Pressures lower than 606 kPa will enhance boiling. The current design RVT pressure of 300 kPa could be used with a saturation temperature of 135°C.

Therefore, Zircaloy beam tubes can be used under boiling conditions within thermal and pressure limits.

## 4.7 COOLING SCHEME 5—INTERNAL MINISHROUD NEAR THE REACTOR VESSEL TANK WALL

Two calculations were performed for scheme 5 using two maximum temperatures for the aluminum.

### 4.7.1 Analysis of Beam Tube Cooling Scheme 5—Internal Minishroud near the Reflector Vessel Tank Wall (Maximum Aluminum Temperature of 149°C)

This section describes the thermal hydraulic analysis of cooling scheme 5 (internal minishroud or skirt near the RVT wall). In this scheme, as shown in Fig. 4.6, half of the water flow entering the RVT gets diverted into the space between the minishroud and the RVT wall. This minishroud goes up to half the height of the RVT, where it gets connected to the shrouds of the following 11 components: 7 beam tubes, 1 through-tube, 1 hot source, and 2 cold sources. The water flows into the minishroud and from there into the shrouds of these 11 components, cooling them by forced convection. The water exits the components' shrouds and mixes with the water in the RVT. About half of the water flow enters directly into the RVT through orifices at the bottom of the minishroud (Fig. 4.6).

This analysis demonstrates that cooling scheme 5 is feasible with a minishroud 5 mm thick, separated 25 mm from the RVT wall, using the available coolant $\Delta P$ of 35 kPa and a total coolant flow of 122.6 kg/s. The $\Delta P$ of 35 kPa is the difference between 0.3 MPa, the coolant pressure available at the entrance to the RVT, and 0.265 MPa, the static head of $D_2O$ inside the RVT. Of the total 122.6 kg/s of required coolant flow, 62.6 kg/s flows up into the minishroud to cool by forced convection the 11 components described and the minishroud itself. The remaining 60 kg/s flows directly into the RVT through 10 orifices located in the lower portion of the minishroud (Fig. 4.6).

The temperature of the water entering the RVT is 45°C. The maximum temperature allowed for the water in the RVT is 95°C. The maximum temperatures used for the aluminum in these calculations are 149°C at any internal point and 130°C at the Al surface in contact with water. The dimensions used for the components to be cooled are given in Table 4.1.

Table 4.11 shows the cooling requirements as well as the calculated $\Delta P$ for each of the components' shrouds to be cooled in the RVT. The largest $\Delta P$ occurs through the cold source shroud (33.7 kPa), a value very close to the available 35 kPa. Most of this $\Delta P$ occurs when the water flows through the perforated stiffeners between the shroud and the outer thimble. Only heat removal from the outer thimble of the cold source was considered in this calculation. If the heat from the inner thimble has to be removed also, a larger coolant flow will be required, resulting in a higher $\Delta P$, above the 35 kPa currently available.

As shown in Table 4.11, the $\Delta P$ through each of the components' shrouds varies from 600 Pa for the hot source to 33.7 kPa for the cold source. To obtain the flow needed for each component, orifices

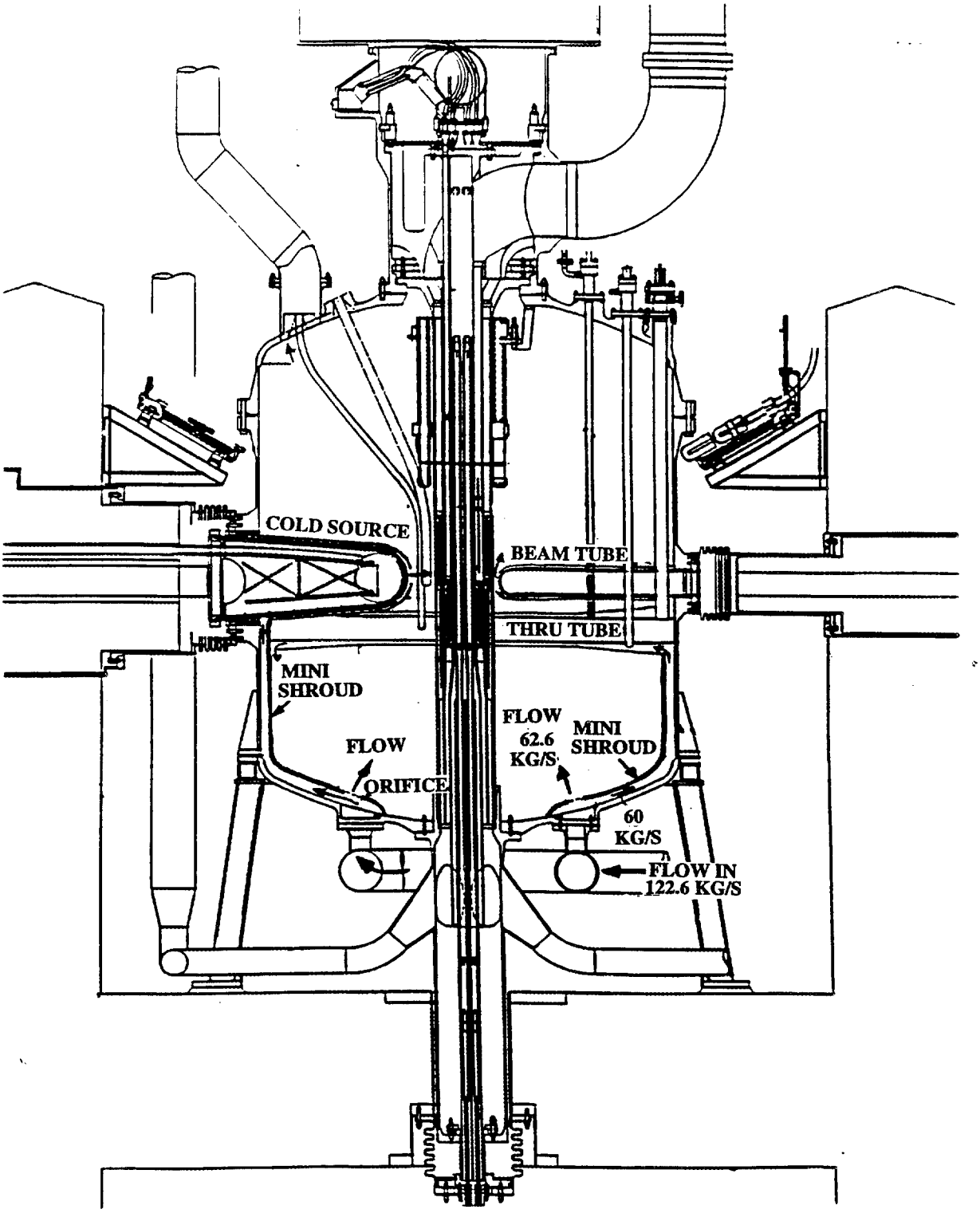


**Fig. 4.6. Cooling scheme 5, internal minishroud with Al maximum temperature of 149°C.**

**Table 4.11. Cooling requirements for the RVT components in scheme 5 with maximum aluminum temperature of 149°C**

| Component | $q'''_{max}$ (W/g) | $q''_{max}$ (kW/m$^2$) | $T_{in}$[a] (°C) | $T_{out}$ (°C) | $\Delta T$ (°C) | $h_{max}$ [kW/(m$^2$ · °C)] | $V_{max}$ (m/s) | Gap (mm) | Flow (kg/s) | $\Delta P$ (kPa) |
|---|---|---|---|---|---|---|---|---|---|---|
| Beam tubes (7) | 16 | 550 | 50 | 67 | 58 | 9.5 | 1.524 | 3.3 | 3.143 × 7 = 22.0 | 6.0 |
| Through-tube[b] | 14 | 300 | 50 | 94 | 57 | 5.3 | 0.7 | 3 | 1.6 | 4.2 |
| Hot source[c] | 5.7 | 90 | 50 | 55 | 75 | 1.2 | 0.16 | 16.5 | 4.4 | 0.6 |
| Cold sources (2)[c,d] | 7 | 181 | 50 | 54 | 76 | 2.4 | 0.37 | 25.4 | 17.3 × 2 = 34.6 | 33.7 |
| Components | | | | | | | | | 62.6 | |
| Minishroud/skirt | | | 45[a] | 50[a] | | | 0.208 | 25 | 62.6 | 0.1 |
| RVT (bulk) | | | 45 | 83 | | | | | 60.0 | 35.0 |
| GRAND TOTAL | | | | | | | | | 122.6 | 35.0 |

[a]The cooling water enters the RVT at 45°C. By the time the water reaches the components to be cooled, its temperature has increased to 50°C because of the heat removed from the minishroud, the RVT lower head, and the lower half of the RVT side wall.

[b]In the through-tube, water enters one end at 50°C and exits the other end at 94°C. The temperature of the water at the midpoint, where $q''_{max}$ and $h_{max}$ occur, is 73°C. The $\Delta T$ available for heat transfer at midpoint is 130 − 73 = 57°C.

[c]The hot and cold sources require low coolant velocities (0.16 and 0.37 m/s, respectively) but rather large mass flow rates (4.4 and 17.3 kg/s) because they have large gaps between the shroud and the thimble (16.5 and 25.4 mm).

[d]The heat produced in the inner thimble of the cold source is not removed by this cooling system.

are required at the entrance and/or exit of the shroud of each component to equalize ΔPs. The hot source requires the smallest orifice size because its coolant channel produces the smallest ΔP.

In these calculations, the through-tube shroud has been assumed to be connected to the minishroud at one end and to be open to the RVT at the other end. It is also possible to connect both ends of the through-tube shroud to the minishroud and to allow the flow to leave through an opening at the midpoint of the shroud.

Table 4.12 shows that the total heat generated inside the RVT that needs to be removed by cooling scheme 5 is 19.2 MW. The RVT components not considered in the heat generation tabulation (irradiation facilities, large slant tube, slant cold guides, and outer control rods) are assumed to have their own independent coolant systems; therefore, the heat generated in these components is not removed by cooling scheme 5. The total coolant flow into the RVT of 122.6 kg/s removes this total heat with an increase in temperature from 45°C to 83°C, a value below the maximum desired value of 95°C.

The most difficult part of the design of this concept is in achieving the proper flows and pressure drops through each component's shroud. Appropriate orifices at the connections between the minishroud and each component's shroud are required, but these may be difficult to design. By contrast, schemes 1, 2, and 3 have valves at the entrance to each component's shroud that are easier to adjust to achieve the required flows and pressure drops.

### 4.7.2 Analysis of Cooling Scheme 5—Internal Minishroud with the Maximum Aluminum Temperature Reduced to 125°C

Cooling scheme 5 (internal minishroud or skirt near the RVT wall) has been reanalyzed using a maximum temperature for the aluminum of 125°C. This value is lower than the value used in the previous analysis, where the maximum allowable temperature of the aluminum was 149°C at any internal point. An additional limitation of a maximum temperature of 130°C at any aluminum surface in contact with water prevented boiling at any aluminum surface.

This lower maximum temperature of the aluminum reduces the available ΔT between the Al surface and the water for heat transfer. Consequently, for the same heat loads and heat fluxes, which are unchanged, higher heat transfer coefficients are required, requiring in turn higher coolant flows and resulting in higher ΔPs. Component dimensions (Table 4.1) and heat loads (Table 4.12) are identical to those presented in the previous section, where the analysis used a higher maximum temperature for the aluminum. The new required coolant flows and the calculated ΔP for each component are given in Table 4.13. The most significant difference from the previous analysis is that the calculated ΔP for the cold source is 53 kPa (previously, it was 33.7 kPa), a value above the available design pressure in the RVT of 35 kPa. Therefore, for this concept to be feasible, the available ΔP in the RVT has to be increased to a value above 53 kPa. Table 4.13 shows an assumed value of 55 kPa for this RVT ΔP.

As in the previous analysis, the heat produced in the inner thimble of the cold source is *not* removed by this cooling concept. Also, the through-tube shroud is connected at one end to the minishroud (coolant inlet) and open at the other end for coolant exit.

The total flow through the minishroud is 85.6 kg/s, with additional 40 kg/s flowing directly into the RVT through orifices at the bottom of the minishroud (Fig 4.7) compared to 62.6 kg/s into the minishroud and 60 kg/s directly into the RVT (as discussed in Sect. 4.7.1 and depicted in Fig. 4.6). The total coolant flow required is 125.6 kg/s, similar to the value calculated in the previous analysis (122.6 kg/s) using higher temperature limits for the aluminum. Because the total heat load to be removed is the same in both analyses, the total coolant flow does not need to be very different. The coolant temperature enters the RVT at 45°C and leaves it (after cooling the total heat load of

**Table 4.12. Total heat generated in the reflector vessel tank, in kW**

| Component | Thimble | Shroud | Flange | Total | Estimated error |
|---|---|---|---|---|---|
| Beam tube 1 | 147 | 41 | 15 | 203 | Small (<10%) |
| Beam tube 2 | 140 | 39 | 43 | 222 | Small (<10%) |
| Beam tube 3 | 142 | 40 | 15 | 197 | Small (<10%) |
| Beam tube 6 | 141 | 40 | 15 | 196 | Small (<10%) |
| Beam tube 7 | 135 | 38 | 15 | 188 | Small (<10%) |
| Beam tube 8 | 139 | 39 | 15 | 193 | Small (<10%) |
| Beam tube 9 | 135 | 38 | 15 | 188 | Small (<10%) |
| BEAM TUBE TOTAL | | | | 1,387 | Small (<10%) |
| Through-tube 5-10 | 200 | 80 | 2 × 15 | 310 | Large (>30%) |
| Hot source | 38.8 | 22.3 | 30 | 90.6 | Moderate (10–20%) |
| Cold source 1 | 177 | 50 | 50 | 277 | Small (10%) |
| (Inner thimble) | (53.5) | | | (330.5) | Small (10%) |
| Cold source 2 | 177 | 50 | 50 | 277 | Small (10%) |
| RVT sidewall | 402 | | | | Moderate (10–20%) |
| RVT upper head | 297 | | | | Moderate (10–20%) |
| RVT lower head | 1,013 | | | | Moderate (10–20%) |
| RVT TOTAL | | | | 1,712 | Moderate (10–20%) |
| CPBT top | 66.3 | | | | Small (10%) |
| CPBT bottom | 60.7 | | | | Small (10%) |
| CPBT TOTAL | | | | 127 | Small (10%) |
| $D_2O$ Coolant | | | | 14,654 | Moderate (10–20%) |
| TOTAL | | | | 18,834.6 | |
| Minishroud/skirt (5 mm) | 100 | | | 100 | Moderate (20%) |
| Large slant beam tube | | | | | |
| Slant cold guide tubes (2) | | | | | |
| Outer control rods | | | | 265.4 | Large (>30%) |
| Experimental facilities | | | | | |
| Other flanges and structures | | | | | |
| GRAND TOTAL | | | | 19,200.0 | |

**Table 4.13. Cooling requirements for the RVT components, scheme 5 with maximum aluminum temperature of 125°C**

| Component | $q'''_{max}$ (W/g) | $q''_{max}$ (kW/m$^2$) | $T_{in}$[a] (°C) | $T_{out}$ (°C) | $\Delta T$ (°C) | $h_{max}$ [kW/(m$^2$ · °C)] | $V_{max}$ (m/s) | Gap (mm) | Flow (kg/s) | $\Delta P$ (kPa) |
|---|---|---|---|---|---|---|---|---|---|---|
| Beam tubes (7) | 16 | 550 | 50[a] | 60 | 40 | 13.7 | 2.43 | 3.3 | 5 × 7 = 22.0 | 15.2 |
| Through-tube[b] | 14 | 300 | 50 | 86 | 48 | 6.2 | 0.87 | 3 | 1.9 | 6.5 |
| Hot source | 5.7 | 90 | 50 | 54 | 68 | 1.3 | 0.2 | 16.5 | 5.3 | 0.9 |
| Cold sources (2)[c] | 7 | 181 | 50 | 53 | 67 | 2.7 | 0.47 | 25.4 | 21.7 × 2 = 43.4 | 53.0 |
| Components | | | | | | | | | 85.6 | |
| Minishroud/skirt | | | 45 | 50 | | | 0.29 | 25 | 85.6 | 0.19 |
| RVT (bulk) | | | 45 | 81 | | | | | 40.0 | 55.0 |
| GRAND TOTAL | | | | | | | | | 125.6 | 55.0 |

[a]The cooling water enters the RVT at 45°C. By the time the water reaches the components to be cooled, its temperature has increased to 50°C because of the heat removed from the minishroud, the RVT lower head, and the lower half of the RVT side wall.

[b]In the through-tube, water enters one end at 50°C and exits the other end at 86°C. The temperature of the water at the midpoint, where $q''_{max}$ and $h_{max}$ occur, is 70°C. At the midpoint, the $\Delta T$ through the thimble wall is 7°C; therefore, the $\Delta T$ available for heat transfer is 125 − 7 − 70 = 48°C.

[c]The heat produced in the inner thimble of the cold source is not removed by this cooling system.

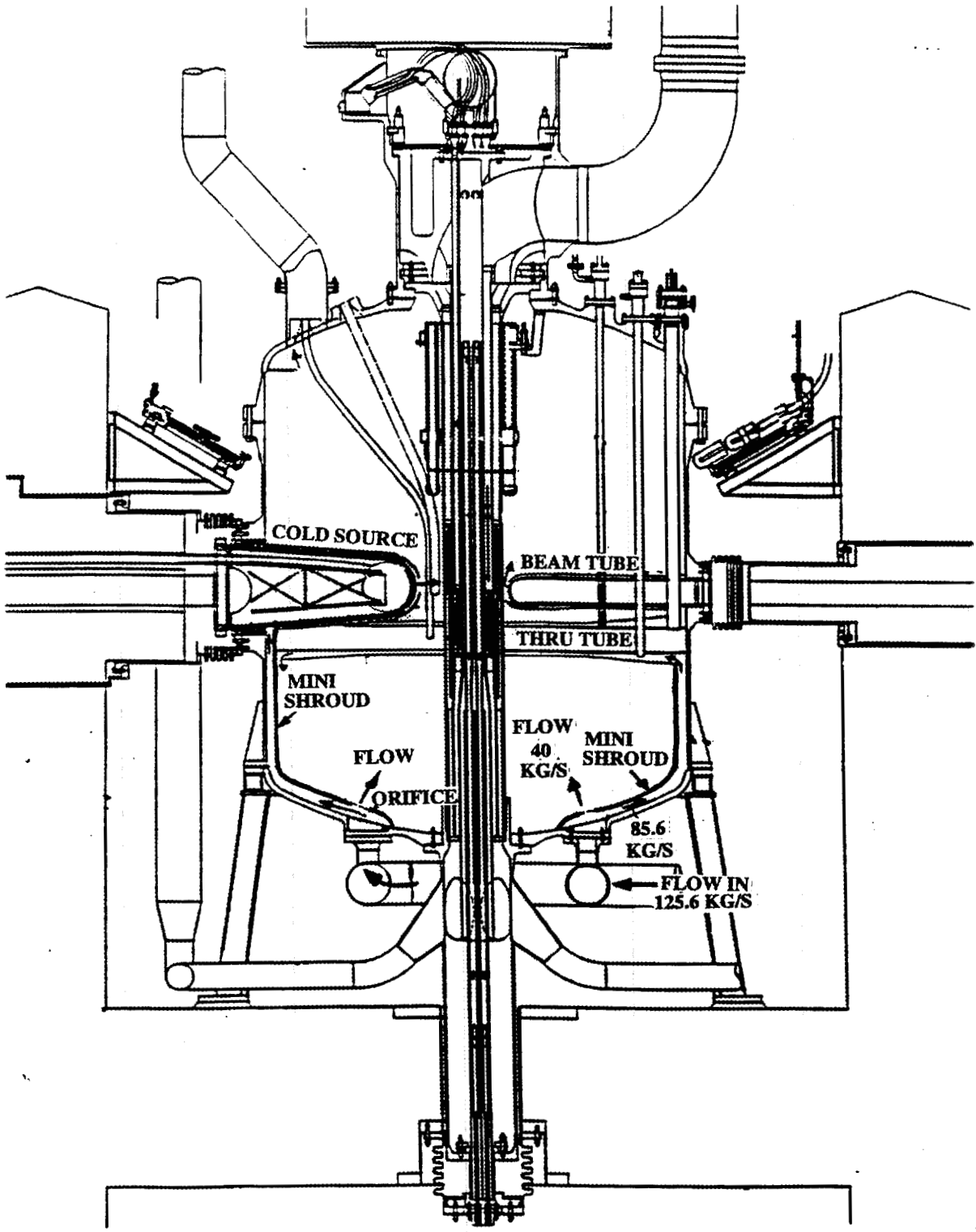


**Fig. 4.7. Cooling scheme 5, internal minishroud with Al maximum temperature of 125°C.**

19.2 MW) at a temperature of 81°C, a value well below the maximum desired temperature of 95°C for the bulk coolant temperature leaving the RVT.

## 4.8 BEAM TUBE COOLING WITHOUT SHROUD BY NATURAL CONVECTION IN THE THREE-ELEMENT ANS CORE

The maximum heating rates that can be cooled by natural convection outside unshrouded beam tubes have been calculated for beam tubes with two different cross sections. A circular cross section (100-mm inside diameter, 4-mm body thickness, and 3.5-mm tip thickness) and an elliptical cross section (100- × 200-mm inside diameters, 14.1-mm body thickness, and 3.5-mm tip thickness) have been considered.

A natural convection heat transfer coefficient of 1.5 kW/(m$^2$ · °C) and a coolant temperature of 50°C were used in these calculations. Three different maximum temperatures for the aluminum were considered: 149°C, 100°C anywhere in the aluminum, and 130°C at the coolant surface. The results of these calculations are shown in Tables 4.14 and 4.15. The calculated heating rate of the tip of the circular beam tube is slightly higher (by 6%) than the tip of the elliptical beam tube because the circular one has a larger surface-to-volume ratio than the elliptical one. Both tips have the same thickness. When the aluminum maximum temperature of 149°C is used, the surface temperature is around 147°C for the circular beam tube and 144°C for the elliptical beam tube. These temperatures are above the boiling temperature of the coolant in the reflector tank. A maximum temperature of 130°C at the Al surface has been used for the calculational results presented in the middle row of the tables.

It should be noted that the value of the natural convection heat transfer coefficient used, 1.5 kW/(m$^2$ · °C), although achievable, is optimistic. If a more realistic value of 1.0 kW/(m$^2$ · °C) is used, the values of Tables 4.14 and 4.15 should be reduced by 1/3, as shown in Tables 4.16 and 4.17.

Preliminary estimations of maximum heating rates generated in the three-element core are 7.3 W/g with full overlap and 5.4 W/g without overlap. These values are larger than the maximum heat generation rates that can be removed by natural convection from the body of an elliptical beam tube (Tables 4.15 and 4.17) even considering the maximum aluminum temperature of 149°C. Therefore, natural convection cannot cool elliptical cross-section beam tubes in the three-element core, and forced convection is required. However, circular beam tubes can be cooled by natural convection in the three-element core. In the three-element core with overlap, cooling by natural convection can be accomplished if the maximum temperature of the aluminum is 132°C or higher (Tables 4.14 and 4.16). In the three-element core without overlap, the body of circular beam tubes can be cooled without exceeding the 100°C maximum temperature of the aluminum if the natural convection heat transfer coefficient of 1.5 kw/m$^2$ is achieved (Table 4.14).

**Table 4.14. Maximum heat generation rates that can be removed with a natural convection heat transfer coefficient of 1.5 kW/(m² · °C) for circular beam tubes (100 × 4 mm)**

| Maximum aluminum temperature (°C) | Tip (3.5 mm thick) | | | Body (4 mm thick) | | |
|---|---|---|---|---|---|---|
| | Surface temperature (°C) | Heat flux (kW/m²) | q‴ (W/g) | Surface temperature (°C) | Heat flux (kW/m²) | q‴ (W/g) |
| 149 | 148 | 145.5 | 16.5 | 147 | 144 | 14.0 |
| 132 | 130 | 118.5 | 13.4 | 130 | 118.5 | 11.5 |
| 100 | 99 | 75.0 | 8.5 | 98 | 73.5 | 7.2 |

**Table 4.15. Maximum heat generation rates that can be removed with a natural convection heat transfer coefficient of 1.5 kW/(m² · °C) for elliptical beam tubes (200 × 100 × 14.1 mm)**

| Maximum aluminum temperature (°C) | Tip (3.5 mm thick) | | | Body (14.1 mm thick) | | |
|---|---|---|---|---|---|---|
| | Surface temperature (°C) | Heat flux (kW/m²) | q‴ (W/g) | Surface temperature (°C) | Heat flux (kW/m²) | q‴ (W/g) |
| 149 | 148 | 145.5 | 15.5 | 144 | 139.5 | 4.1 |
| 132 | 130 | 118.5 | 12.6 | 130 | 118.5 | 3.5 |
| 100 | 99 | 75.0 | 8.0 | 95 | 69.0 | 2.1 |

**Table 4.16. Maximum heat generation rates that can be removed with a natural convection heat transfer coefficient of 1.0 kW/(m² · °C) for circular beam tubes (100 × 4 mm)**

| Maximum aluminum temperature (°C) | Tip (3.5 mm thick) | | | Body (4 mm thick) | | |
|---|---|---|---|---|---|---|
| | Surface temperature (°C) | Heat flux (kW/m²) | q‴ (W/g) | Surface temperature (°C) | Heat flux (kW/m²) | q‴ (W/g) |
| 149 | 148 | 97.0 | 11.0 | 144 | 96 | 9.3 |
| 132 | 130 | 79.0 | 8.9 | 130 | 79 | 7.7 |
| 100 | 99 | 50.0 | 5.7 | 95 | 49 | 4.8 |

**Table 4.17. Maximum heat generation rates that can be removed with a natural convection heat transfer coefficient of 1.0 kW/(m² · °C) for elliptical beam tubes (200 × 100 × 14.1 mm)**

| Maximum aluminum temperature (°C) | Tip (3.5 mm thick) | | | Body (14.1 mm thick) | | |
|---|---|---|---|---|---|---|
| | Surface temperature (°C) | Heat flux (kW/m²) | q‴ (W/g) | Surface temperature (°C) | Heat flux (kW/m²) | q‴ (W/g) |
| 149 | 148 | 97.0 | 10.3 | 144 | 93 | 2.7 |
| 132 | 130 | 79.0 | 8.4 | 130 | 79 | 2.3 |
| 100 | 99 | 50.0 | 5.3 | 95 | 46 | 1.4 |

# 5. LIFT FORCES ON THE INNER CONTROL RODS RESULTING FROM THE UPWARD COOLANT FLOW

## 5.1 CONTROL ROD DESIGNS

The three inner control rods (ICRs) of the ANS reactor are withdrawn upward from the reactor core. They are inserted into the reactor core downwards in the opposite direction of the upward coolant water flow. This upward coolant flow induces upward forces (or lift forces) on the ICRs that need to be quantified. This chapter calculates these upward lift forces over the ICRs under different conditions.

During a scram, the high loads over the ICRs may shear a control rod from the insertion mechanism. Lift forces over a sheared control rod are also calculated. It is important to reduce these lift forces as much as possible. In the case of a sheared control rod, the lift forces should be smaller than the weight of the sheared control rods to avoid the detached control rods being dragged upwards and away from the core by the coolant flow. One of the design requirements of the ICRs is that the control rods must drop by gravity into the core under any circumstances.

All these calculations have been performed for the two-element core using highly enriched uranium with 93% enrichment. However, three different designs of the ICRs have been considered. The first design employs hafnium as the absorber material, surrounded by Inconel cladding with an intervening gap for cooling and with an aluminum guide tube. There are eight spacers between the hafnium and the Inconel cladding. The second design also employs hafnium as the absorber, surrounded by titanium cladding and with a Zircaloy guide tube. There are 12 spacers between the hafnium and the titanium cladding but only at the entrance and at the exit of the hafnium/titanium annulus. This second design resolves thermal problems of the first design at the Inconel/aluminum junction but does not reduce the lift forces. A third proposed design consists of modifications to the annulus of the second design, reducing the number of spacers to eight and providing constant annulus area without the abrupt area changes of the second design. This design successfully reduces the lift forces to values below the weight for a sheared control rod.

## 5.2 LIFT FORCES OVER THE INNER CONTROL RODS OF THE FIRST DESIGN

### 5.2.1 Geometry and Initial Conditions

The following are the geometry and initial conditions of the first design:

| | |
|---|---|
| Inside diameter of the central hole region where the three control rods are located, mm | 190 |
| Outside diameter (cladding) of one control rod, mm | 71 |
| Inconel inside diameter, mm | 65 |
| Hafnium outside diameter (inside diameter of the annulus between the Inconel and the hafnium), mm | 54.86 |
| Hafnium inside diameter, mm | 46.228 |
| Control rod inside length (with coolant flow), m | 1.5 |
| Control rod outside length, fully withdrawn, m | 2.7 |
| Coolant velocity (outside and inside the control rod), m/s | 6 |
| Maximum velocity of the control rods during insertion, m/s | 6 |

| | |
|---|---|
| Distance control rods are withdrawn when maximum velocity occurs, m | 0.6 |
| Total travel distance, m | 1.3 |
| Total length (including drive tube), m | 4.3 |
| Drive tube thickness, mm | 8 |
| Total accelerated mass of a control rod, kg | 36.15 |
| Temperature of the coolant, °C | 45 |

Eight spacers are assumed between the hafnium and the Inconel tube. These spacers are part of the hafnium. Each spacer is assumed to cover an angle of 12.86°. The eight spacers cover 2/7 of the open annulus between the Inconel and the hafnium. The spacers are assumed to be in perfect contact with the inside surface of the cladding. Therefore, the outside diameter of hafnium, including the spacers, is assumed to be 65 mm. (Actually, this diameter is only 64 mm, and there is a gap of 1 mm between the spacers and the cladding).

There are also two sets of rollers that keep the control rods in position without touching the walls of the central hole. The first one is always in contact with the control rods. The second one is in contact with the control rods only when the control rods are withdrawn. Each roller set has three rollers in contact with each control rod. The first set of rollers also yields a significant pressure drop to the coolant flow to force coolant into the cladding/absorber annulus.

It is also assumed that there is a plate (orifice) at the exit of the channel surrounded by hafnium to equalize the pressure drop through this channel with the pressure drop through the annulus formed by hafnium and Inconel.

Figures 5.1 through 5.5 show the geometrical dimensions and configuration of the ICRs.

### 5.2.2 Calculation of Lift Forces

The total lift forces are the summation of shear forces resulting from friction over the lateral walls of the rods and of forces resulting from pressure differentials. Two terms are included for the pressure differential forces. The first term is the contribution from the static pressure differential resulting from the height of the water column above the different points of the control rod. This term is in fact the "buoyancy force." The "other $\Delta P$ forces" include forces resulting from pressure differentials (excluding the static $\Delta P$), as pressures at the bottom of the rods are higher than at the top because of the flow.

Two calculations have been completed. The first calculation is for the control rods fully withdrawn under steady-state conditions. The second calculation is for the dynamic situation when the control rods are being inserted at a velocity of 6 m/s with 0.6 m inserted (half of the way in). Table 5.1 summarizes the results of these two calculations.

These calculations indicate that the buoyancy forces are significant, that the total forces can be as high as 2 *g*, and that the largest contribution to the total forces are from the "other $\Delta P$ forces." However, the largest uncertainty in the calculations is also in these "other $\Delta P$ forces" because some of the forces acting on the different portions of the control rod, aluminum carrier, and insertion mechanism are not well defined. These forces depend on the flows circulating among the different regions of the control rod piston, which are dependent on the detailed design of these regions (holes that connect the regions, etc.). All of these details are not yet completely defined. The pressures used in this calculation are best-estimate values. However, large uncertainties still remain. Therefore, these pressures (and the corresponding $\Delta P$ forces) need be revised when the final design data are available.

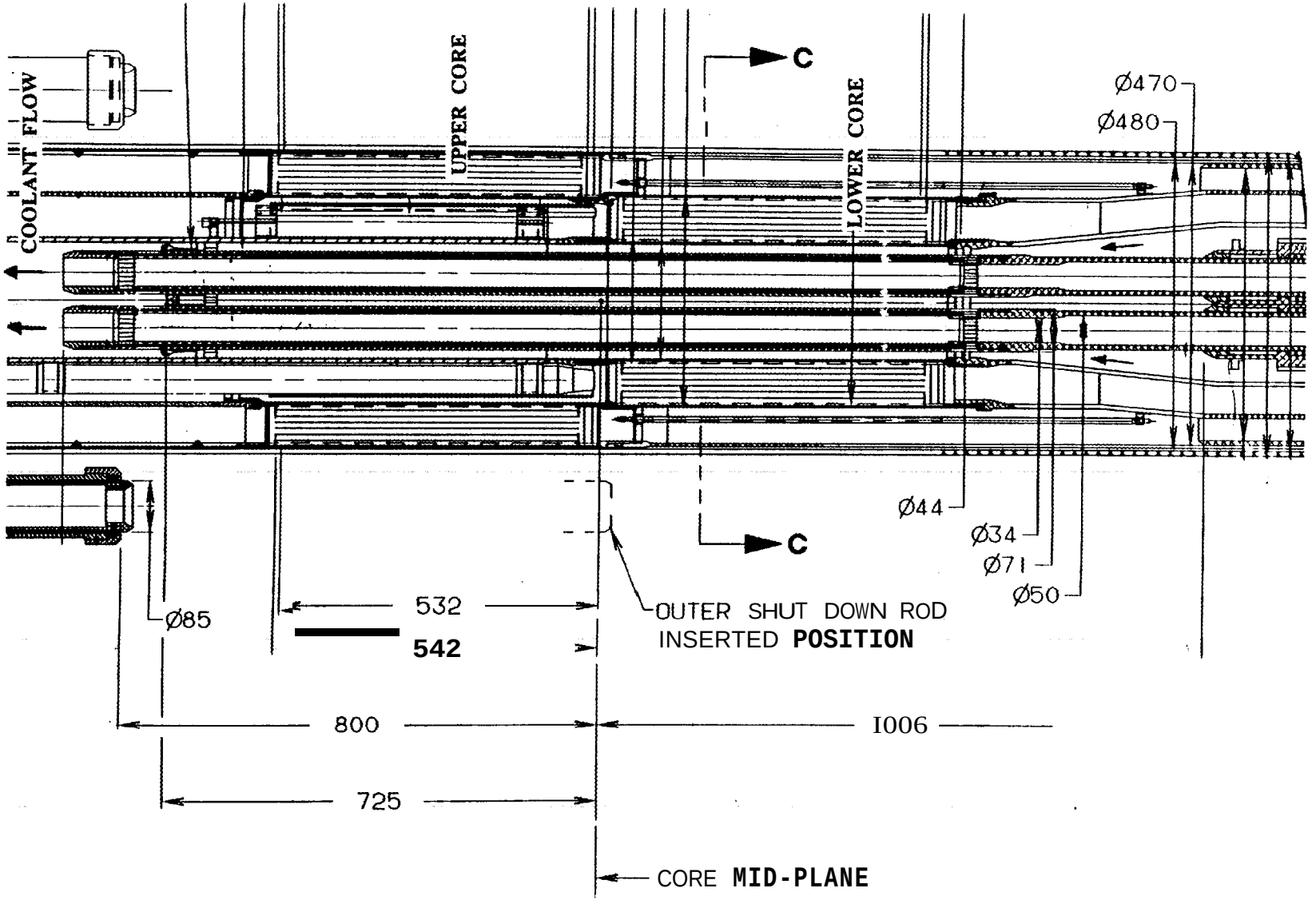


**Fig. 5.1. Top of the inner control rods (first design).**

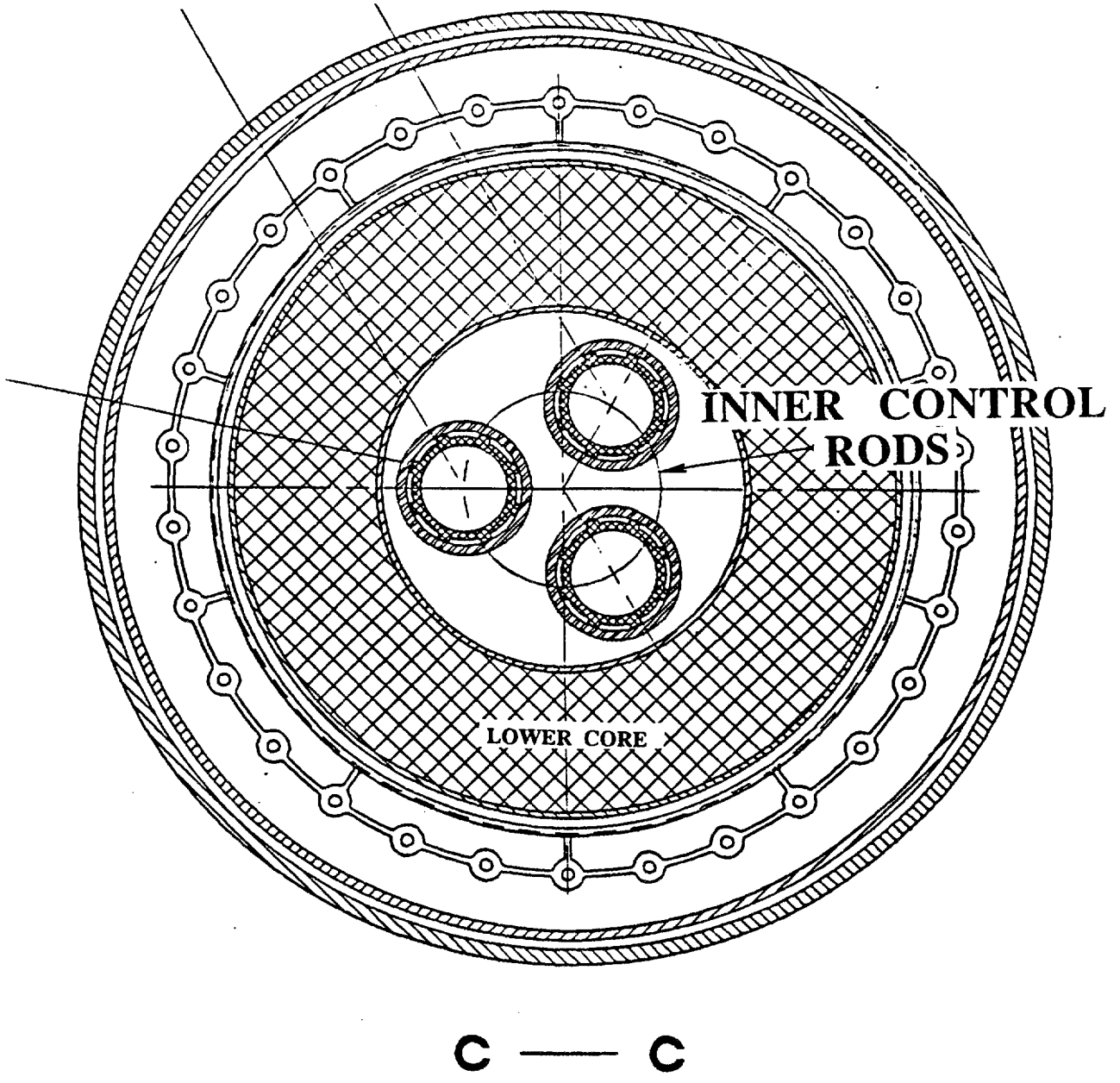


**Fig. 5.2. Horizontal cross section of the inner control rods (first design).**

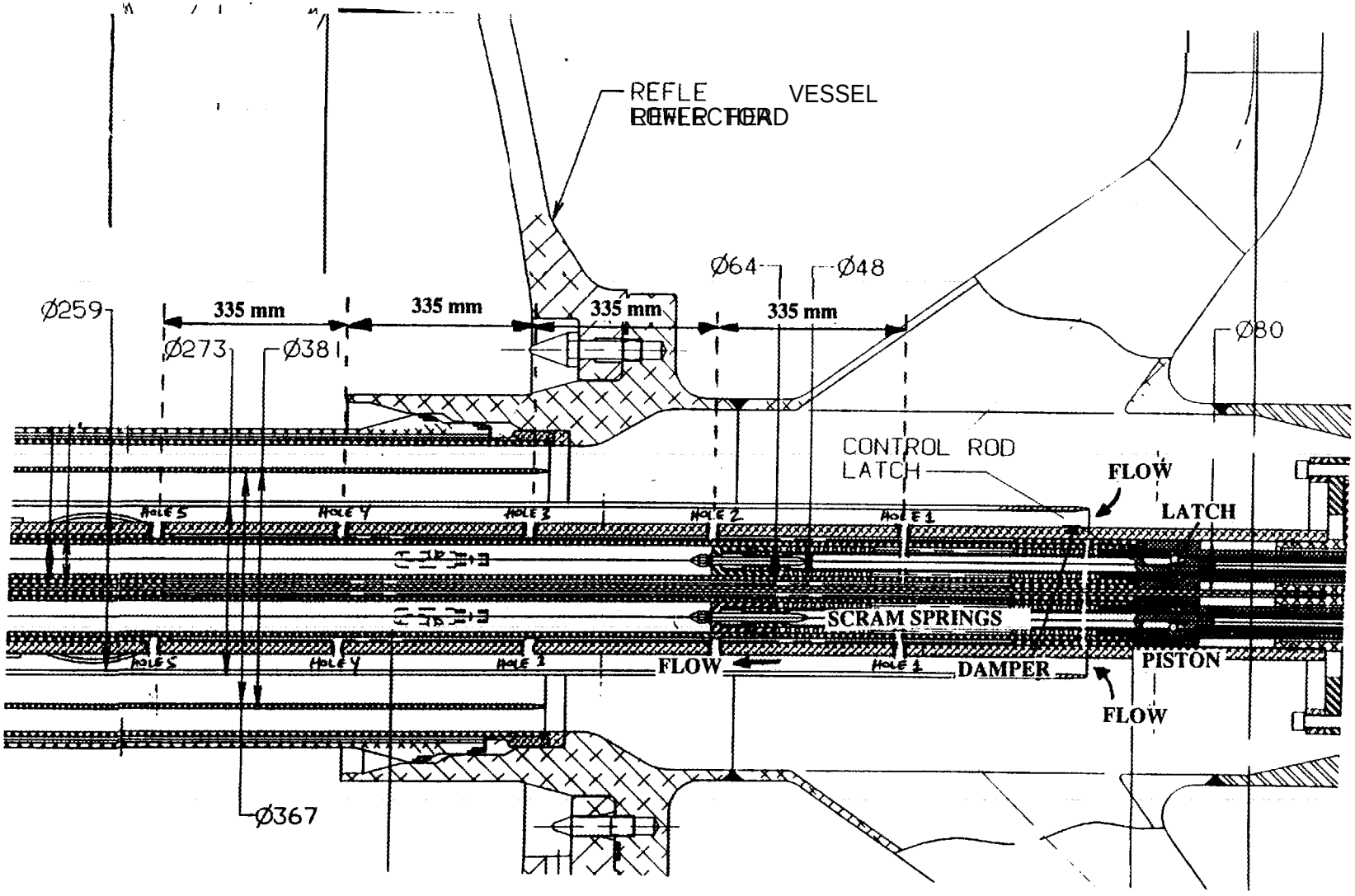


**Fig. 5.3. Middle portion of the inner control rods (first design).**

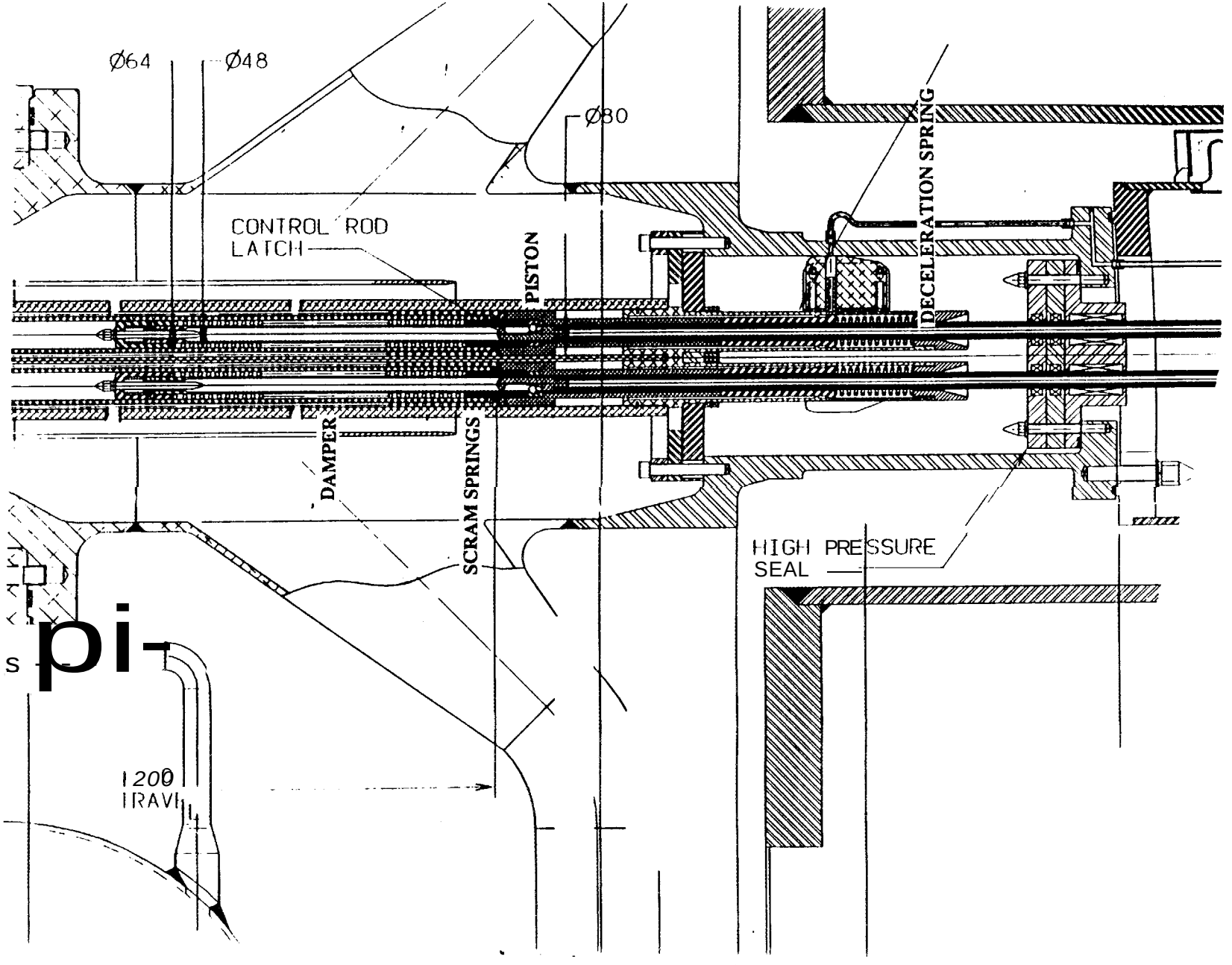


**Fig. 5.4. Bottom of the inner control rods (first design).**

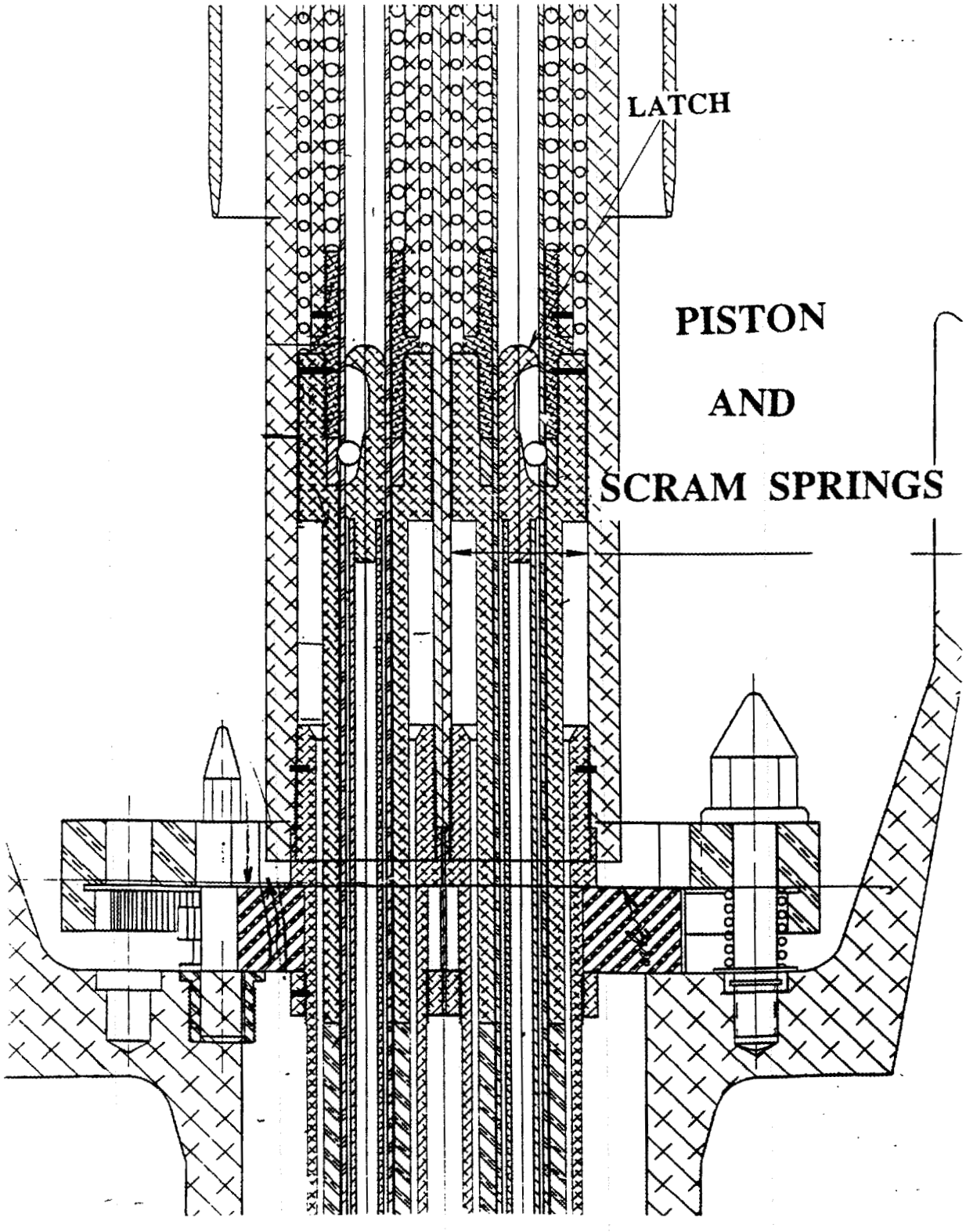


**Fig. 5.5. Latch, piston, and scram springs, inner control rods (first design).**

**Table 5.1. Forces acting on the control rods, in Newtons**

| | Fully withdrawn | Inserted at 6 m/s to 0.6 m |
|---|---|---|
| Shear forces | 142 | 292 |
| Buoyancy forces | 86 | 86 |
| Other ΔP forces | 318 | 329 |
| TOTALS | 546 = 1.54 *g* | 707 = 2 *g* |

### 5.2.3 Recommended Changes for the First Design of the Inner Control Rods to Reduce Lift Forces

Several potential design modifications to the inner control rods have been examined to minimize the upward forces produced by the surrounding coolant flow. It is important to reduce these forces because they are in the direction opposite to the spring forces that insert the control rods into the core (downward) during a scram. These potential modifications reduce the lift forces on the control rods and are therefore beneficial from this point of view. However, these potential modifications may have a negative impact on other areas (structural, neutronics, thermal, etc.) that have not been considered here. Therefore, before these suggested modifications can be approved as design changes, they need to be examined in a global context and their overall impact fully evaluated. Pending this overall evaluation, the following modifications are recommended to reduce the forces on the control rods:

1. The orifice plate at the entrance of the central hole region (25% ΔP plate) should be relocated upstream (see Fig. 5.6, previous orifice 1). This orifice plate produces a very large pressure differential between the entrance and the exit of the control rods coolant channel (central hole region) resulting in large forces on the control rods (as high as three times the weight of the control rods' mass). Therefore, relocation of this orifice to a position before the base of the ICRs will eliminate these large pressure differentials. All the calculations here assume that this orifice is relocated.
2. The orifice plate inside the control rod at the top of the hafnium before the exit from the annulus should be eliminated (see Fig. 5.7, previous orifice 2). This orifice plate could produce undesirable effects during a scram because of the water trapped between the plate and the locking mechanism. Also, vacuum is produced behind this orifice plate during a rapid insertion of the control rods. The desired pressure drop for the flow inside the control rod will be obtained by orificing the entrance to the drive tube (Al carrier) as described in point 5 below.
3. The orifice plate inside the control rod upstream of the hafnium (Hf) should also be eliminated (see Fig. 5.7, previous orifice 3). Free passage of coolant between the inside of the drive tube (Al carrier) and the inside of the control rod is allowed. Therefore, coolant will enter at the base of the drive tube (Al carrier) and will flow inside the drive tube length and inside the control rod length. Before this coolant exits the control rod, it will mix with the coolant from the Hf/cladding annulus. The coolant enters this annulus from outside the control rod. The coolant flow required to produce a velocity of 6 m/s inside the Hf is 11.06 kg/s. The flow through the Hf/cladding annulus (to keep also a velocity of 6 m/s) is 4.68 kg/s. Therefore, after both flows mix, the total flow exiting the control rod is 15.74 kg/s. The velocities of this flow inside the drive tube and inside

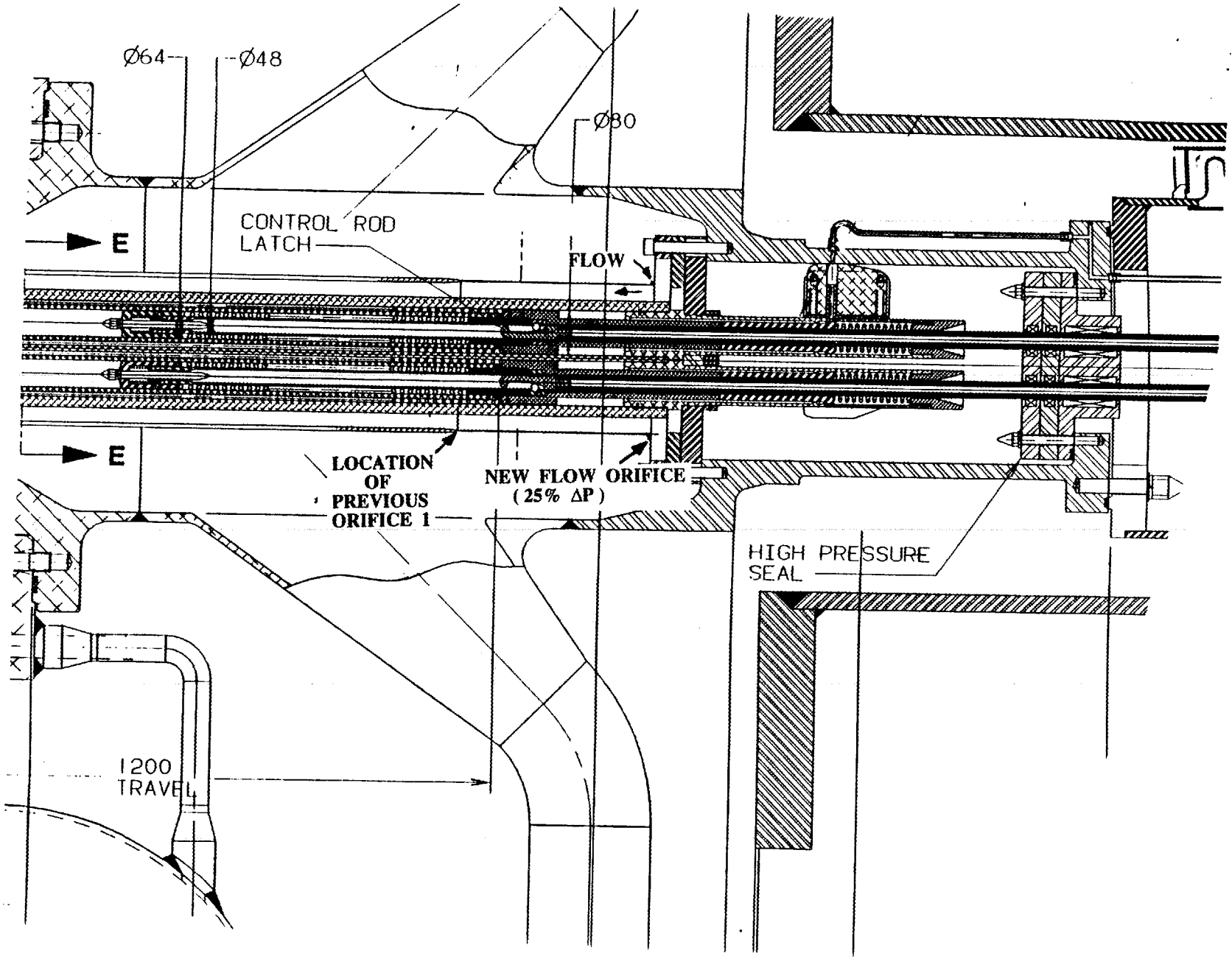


**Fig. 5.6. Inlet orifice (orifice 1) location.**

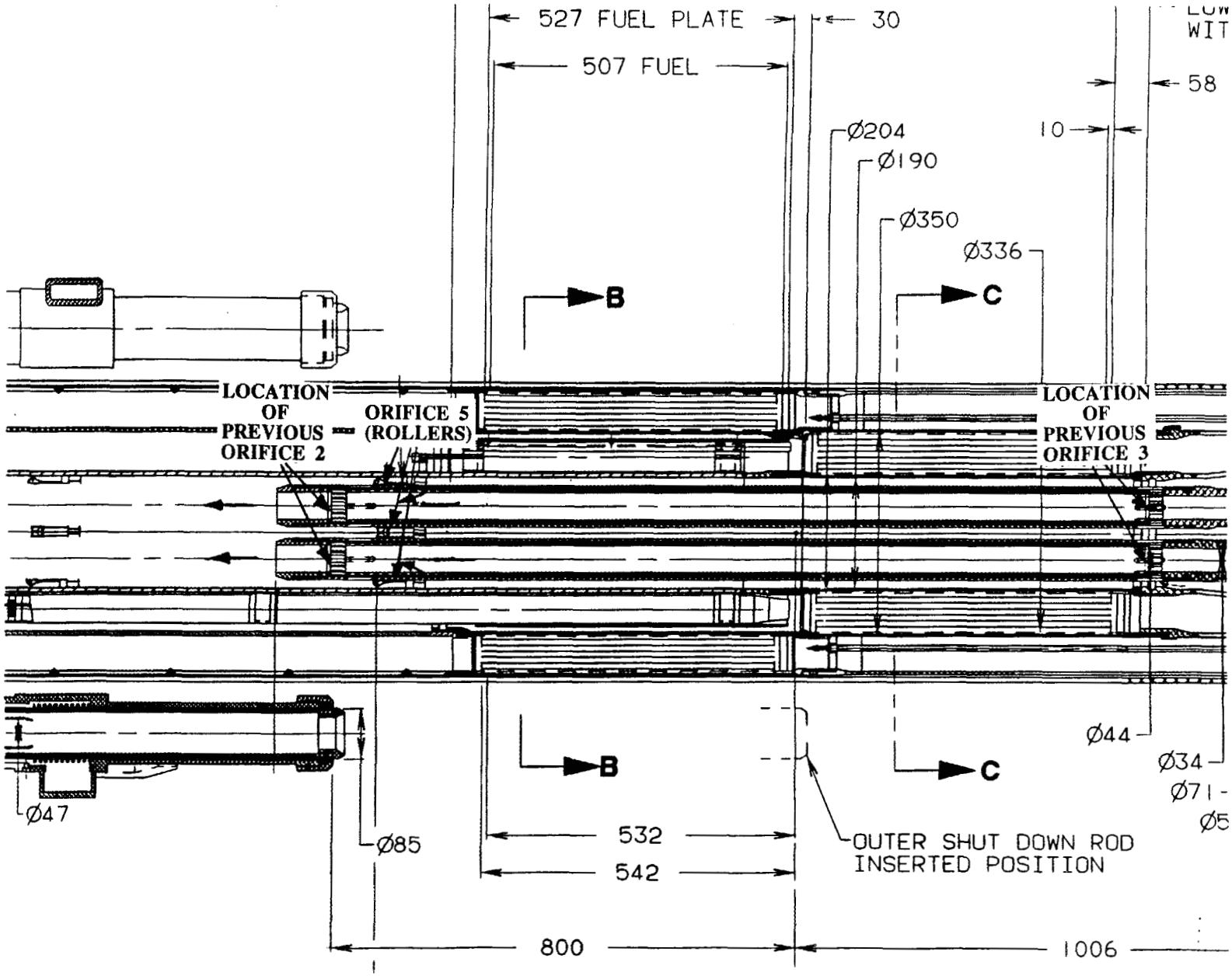


**Fig. 5.7. Location of orifices 2, 3, and 5.**

the control rod are 5.565 m/s for the drive tube, with a diameter of 48 mm; 8.02 m/s for the constriction between the drive tube and the control rod, with a diameter of 40 mm; 6 m/s (as required) for the hafnium channel, with a diameter of 46.2 mm; and finally 8.54 m/s after this flow mixes with the flow from the annulus.

4. Perforations on the lateral walls of the guide tube, drive tube (Al carrier), and drive shaft are needed to allow coolant flow to enter inside the drive tube. It is proposed to have two to four perforations on the drive shaft wall, two to four perforations on the drive tube wall spaced 335 mm apart (see Fig. 5.8), and five perforations along the guide tube length also spaced 335 mm apart (Figs. 5.6 and 5.8). The open area of these perforations should be large enough to ensure a moderate velocity for the coolant at all times. These perforations could be slits cut along the length of the tubes to reduce structural impact and minimize the interaction of the coolant with the springs. For the drive shaft wall, these perforations could be 64 mm long and 4 mm wide. For the drive tube and guide tube walls, these perforations could be 68 mm long by 8 mm wide. There are other possible solutions using different number of perforations at different locations. This proposed solution has the following advantages:
   a. minimum interference of the coolant flow with the springs, i.e., shorter travel distance for coolant along the spring annuli;
   b. minimum resistance during the first 700 mm of travel of a scram; and
   c. increasing resistance during the last 500 mm of travel after scram (damper effect). Consequently, the control rods will be decelerated to a near zero velocity when they contact the deceleration spring.
5. An orifice for the flow entering the drive tube (Al carrier) is required. This orifice could be located in the locking mechanism guide pin (Fig. 5.8, orifice 4). The total pressure drop through this orifice for a flow of 11.06 kg/s should be 68 kPa.
6. The annulus between the cladding and the Hf produces a high $\Delta P$ that affects the magnitude of the pressure differentials over the control rod. Furthermore, there are eight spacers between the cladding and the Hf that can yield thermal problems because of lack of cooling. Modifications to this annulus to reduce the $\Delta P$ and to improve cooling are warranted.
7. The first set of rollers should yield a pressure drop of 72.2 kPa for a coolant mass flow rate of 108.56 kg/s (Fig. 5.7, orifice 5). This orifice plate is required to equalize pressures through all of the parallel channels of the control rod system and to force coolant flow into the annulus.
8. The mass flow rates required for a velocity of 6 m/s inside the Hf, inside the Hf/cladding annulus, and in the outside cladding channel (Fig. 5.9) are as follows:

| | |
|---|---|
| Total mass flow rate before entering or after exiting the control rods | 155.8 kg/s (all control rods) |
| Inside control rod | 11.06 kg/s per control rod |
| Hf/cladding annulus | 4.68 kg/s per control rod |
| Inside control rod after mixing with annulus | 15.74 kg/s per control rod |
| Outside cladding channel | 108.56 kg/s (all control rods) |

### 5.2.4 Recalculation of Lift Forces for the Modified Design

These proposed modifications significantly reduce previously calculated values of the total forces over the control rods (Sect. 5.2.2) by greatly reducing the "other $\Delta P$ forces." Because the detailed geometry of the complete control rod system has not yet been finalized, there are still some uncertainties in the calculated pressures required for the calculations of the "other $\Delta P$ forces." The values in Table 5.2 show the total forces calculated using the geometry with the suggested modifications and a coolant velocity of 6 m/s.

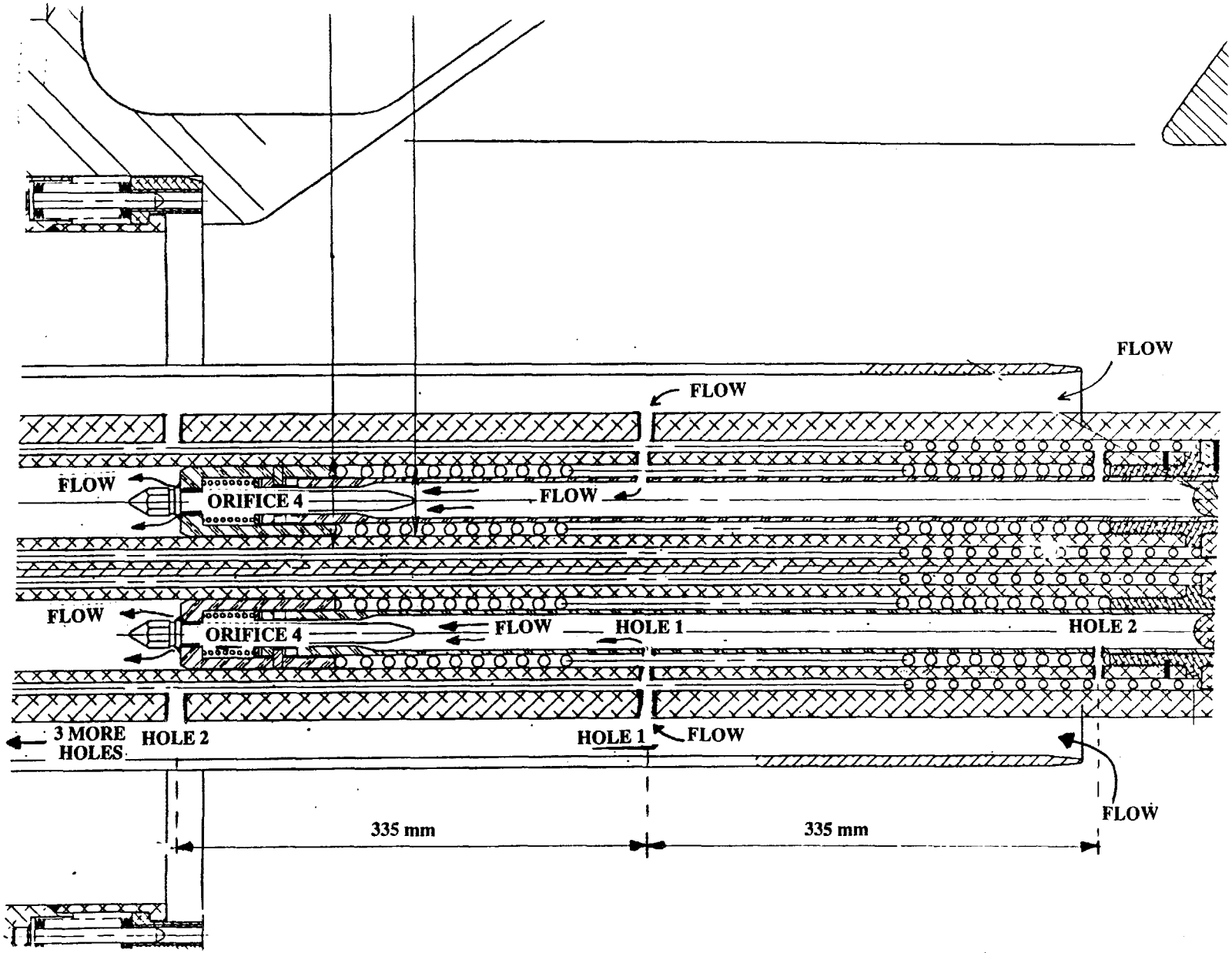


**Fig. 5.8. Location of orifice 4.**

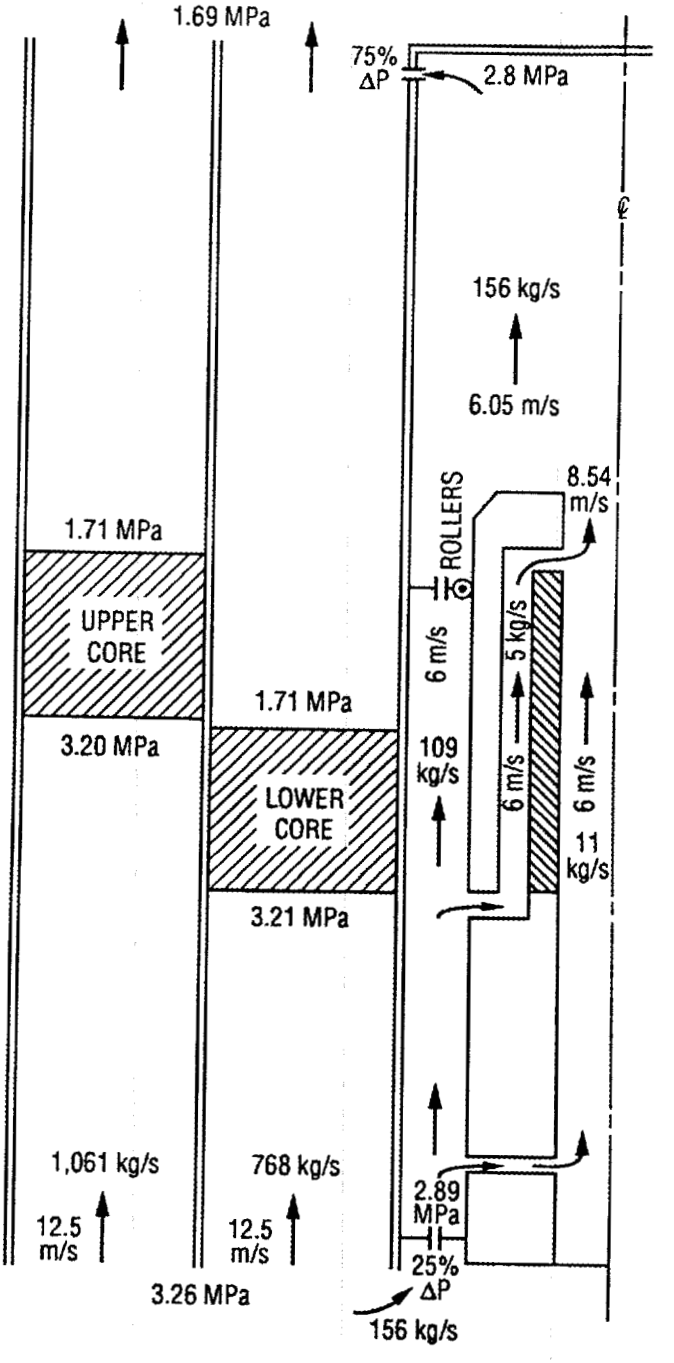


**Fig. 5.9. Flows and pressures in the core and in the inner control rods.**

**Table 5.2. Recalculated lift forces acting on the control rods, in Newtons**

| | Fully withdrawn (steady-state) | Fully inserted (steady-state) | Inserted at 6 m/s to 0.6 m |
|---|---|---|---|
| Shear forces | 130.8 | 104.8 | 284.1 |
| Buoyancy forces | 86.4 | 86.4 | 86.4 |
| Other ΔP forces | 187.0 | 191.0 | 216.0 |
| TOTALS | 404.2 = 1.14 *g* | 382.2 = 1.1 *g* | 586.5 = 1.65 *g* |

These lift forces are reduced when compared to the values calculated in Sect. 5.2.2, but they are still larger than the weight.

The ΔP through the outside channel of the ICRs is ~90 kPa (including the rollers). Figure 5.9 shows the flow distribution and pressure in the core elements and in the ICRs.

### 5.2.5 Total Forces Acting During a Scram over the Inner Control Rods

During a scram, the ICRs are inserted downward (against the flow, but aided by gravity). The forces acting on the ICRs during a scram are the ICRs' weight (downward), two sets of scram springs (both downward, Fig. 5.4), and the coolant lift forces (upward). The upward lift forces have three different contributions: shear forces resulting from friction of the coolant over the ICR's lateral walls, buoyancy forces, and pressure differential forces. Also, near the end of the ICR's travel, there is a damper (Fig. 5.4) that reduces the velocity of the ICRs (upward force) and a linear deceleration spring (upward force) that absorbs the ICR's energy at the end of the travel. The damper force is a function of ICR travel distance and speed. The damper is designed to minimize ICR deceleration forces. The present calculations include all these forces. It was assumed that the coolant flows upward at a velocity of 6 m/s. This velocity may need to be reduced to eliminate the possibility of ejection of sheared control rods. During the scram, as the ICRs move downward, the relative velocity between the coolant and the ICRs will be as high as 11 m/s, and this relative velocity is used to compute the shear forces acting on the rod. The nonlinear system equations were programmed using the Advanced Continuous Simulation Language,[18] and the time history response was solved to get the rod response to the input forces.

Calculations have been performed for scrams with the ICRs fully withdrawn, half withdrawn, and withdrawn only 5 mm. Calculations have also been performed for scrams with no coolant flow present, an abnormal situation that must be considered in the design. Results for the scram starting from the fully withdrawn position are presented in Figs. 5.10–5.12. The calculated acceleration of the ICRs during the scram is shown in Fig. 5.10 as a function of displacement. Distance 0 corresponds to the ICRs fully withdrawn at the beginning of the scram. Distance 1.2 m corresponds to the ICRs fully inserted and latched. During the first 0.12 m of displacement, both sets of springs are acting on the ICRs. After that, only one set is active and the acceleration curve changes slope. At about 0.6 m of displacement, the damper starts acting, and the acceleration changes from positive to negative (upward). The ICRs bounce up and down around the fully inserted position because of the interaction with the deceleration spring. Figure 5.10 shows that, with coolant flow, the maximum positive acceleration (downward) is 4.7 *g* at the beginning of the scram because of the two sets of springs. The minimum acceleration is –2.7 *g* (upward) at the end of the travel because of the combined effect of the damper, the deceleration spring, and the lift forces. Zero acceleration occurs at about 0.85 m of

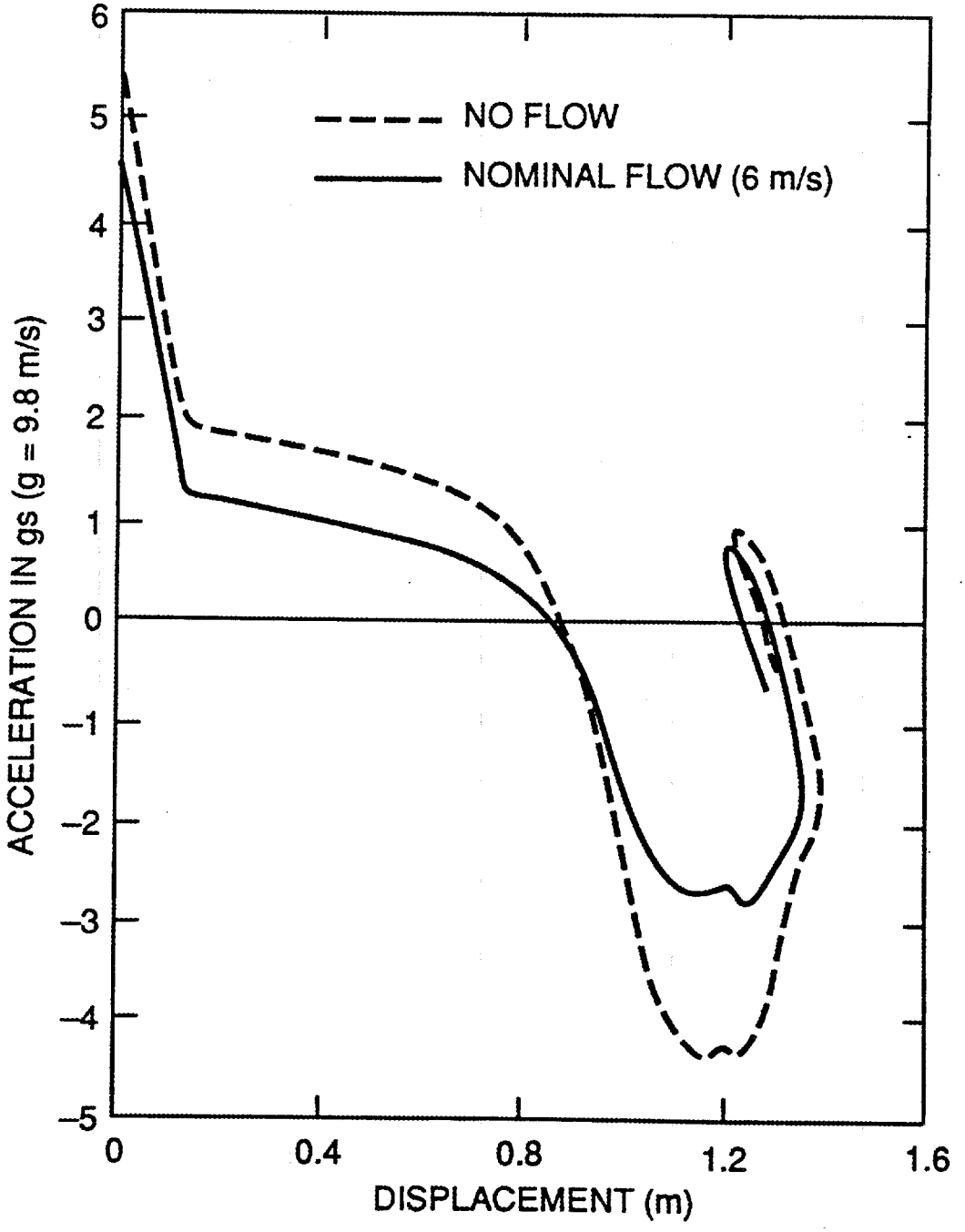


**Fig. 5.10. Acceleration as a function of displacement for the inner control rods after scram.**

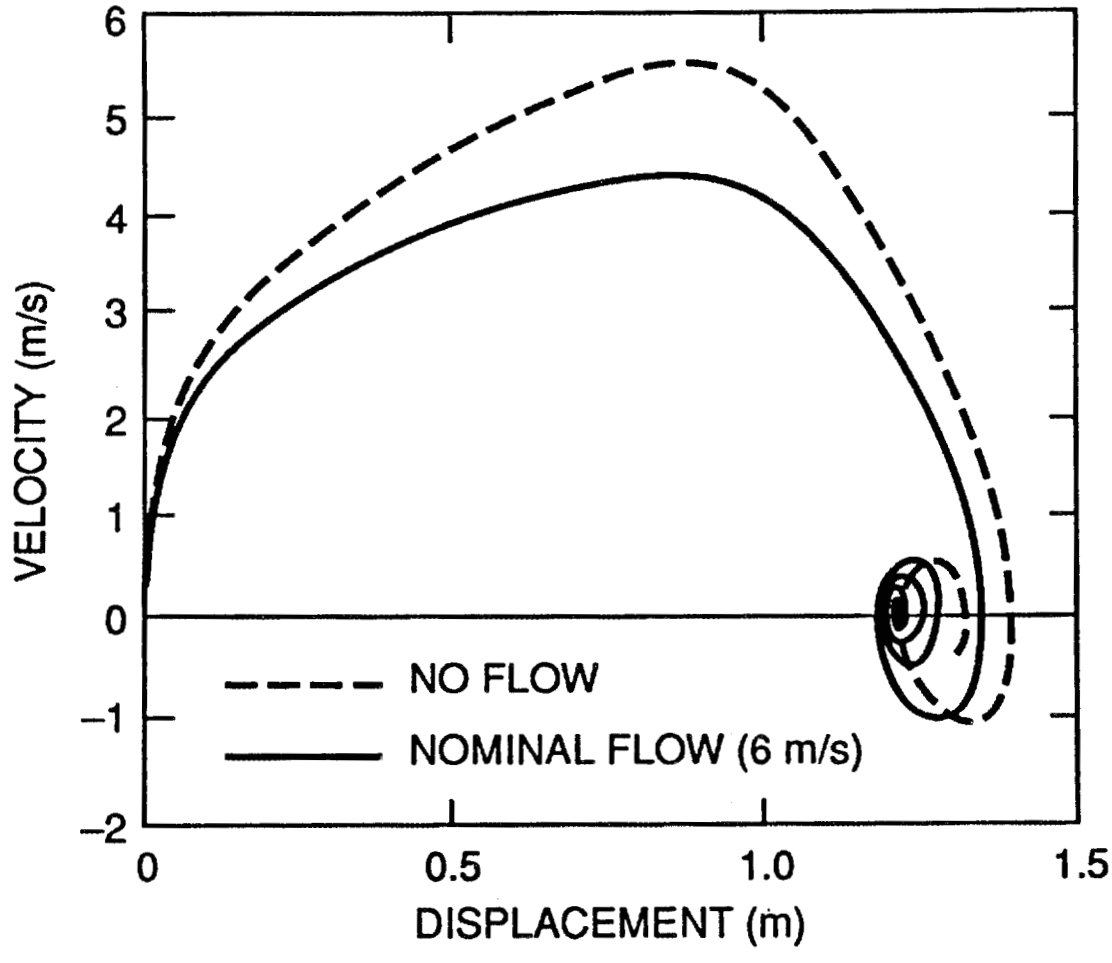


**Fig. 5.11. Velocity as a function of displacement for the inner control rods after scram.**

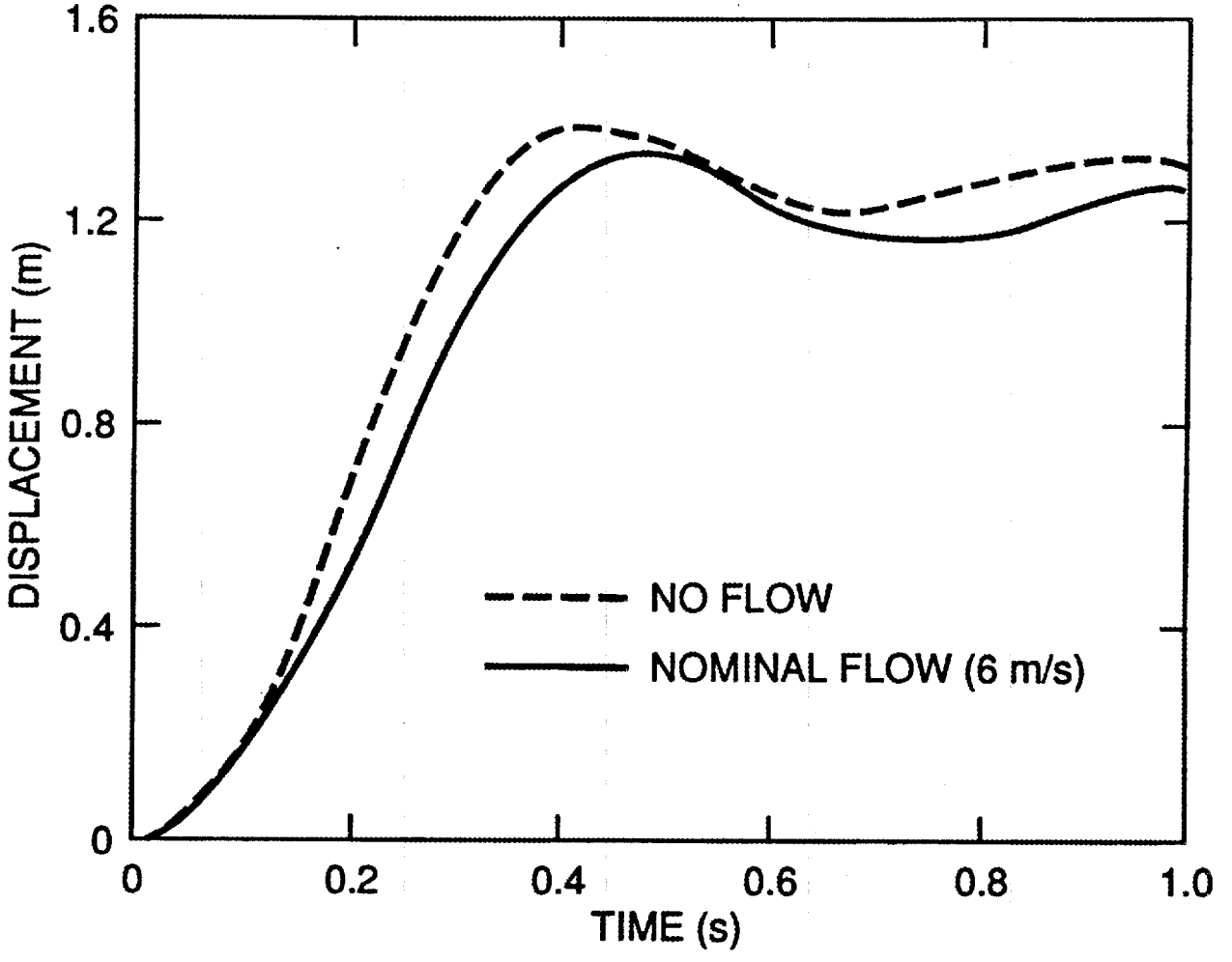


**Fig. 5.12. Displacement as a function of time for the inner control rods after scram.**

travel when the forces over the ICRs change from tension (downward) to compression (upward). Without coolant flow, the forces over the ICRs are larger, with an acceleration of 5.3 *g* at scram initiation and –4.3 *g* near the end of the travel.

Figure 5.11 shows the calculated ICR velocity. The maximum velocity with coolant flow is 4.2 m/s (downward) at about 0.9 m of travel (from fully withdrawn). With no coolant flow, the maximum velocity is 5.5 m/s.

Finally, Fig. 5.12 shows the calculated ICR displacement as a function of time. In the first 100 ms, the ICRs are inserted about 0.2 m, introducing over $1 of negative reactivity into the core in accordance with ICR design requirements. The ICRs reach the fully inserted position 375 ms after scram under flow conditions and in less time without flow. As noted previously, the ICRs bounce up and down around the fully inserted position because of the deceleration spring at the base.

To reduce the loads on the ICRs during the scram, the forces (or the accelerations) over the ICRs should be reduced as much as possible within ICR design requirements. If the nominal coolant velocity is reduced to avoid ejection of sheared control rods, the ICRs' springs could be smaller, reducing the risk of control rod failure. The ICRs are more likely to fail under compression (with negative accelerations) than under tension (with positive accelerations).

To summarize, the current ICR rod design of the ANS reactor would result in scram accelerations of 5.3 to –4.3 *g* and scram velocities up to 5.5 m/s. Additional work was underway at project termination to reduce these accelerations (within design requirements) and to minimize the likelihood of control rod failure.

### 5.2.6 Lift Forces over a Sheared Control Rod

Lift forces have been evaluated for one control rod sheared from the insertion mechanism. Two different cases have been studied. For the first case, the control rod is assumed to be sheared at the bottom of the drive tube next to the piston (Fig. 5.13). Under these conditions, the sheared control rod is free to move out of the guide tube, as the locking mechanism and the springs are actuating over the piston that is now detached from the control rod. For this case, the mass loss is 3.6 kg, and the remaining accelerating mass of the sheared control rod is 36.15 – 3.6 = 32.55 kg, with a weight of 319 N. The total length of the sheared control rod is 3.874 m. For the second case, the control rod is assumed to be sheared at the neck connecting the Inconel to the guide tube (top of the guide tube, Fig. 5.14). The accelerating mass of the sheared control rod is now 24 kg, with a weight of 235.2 N. The total length of the sheared control rod is now 1.625 m. These two cases cover the most probable locations for one control rod getting sheared off during or after a scram.

These calculations indicate that in both cases, the resulting lift forces can drag the sheared control rod upwards. Several solutions to this problem have been explored.

#### 5.2.6.1 Calculations

All of these calculations assumed a coolant velocity of 6 m/s inside and outside the top portion of the control rod (that is, outside the Inconel, inside the hafnium, and in the annulus between the Inconel and the hafnium).

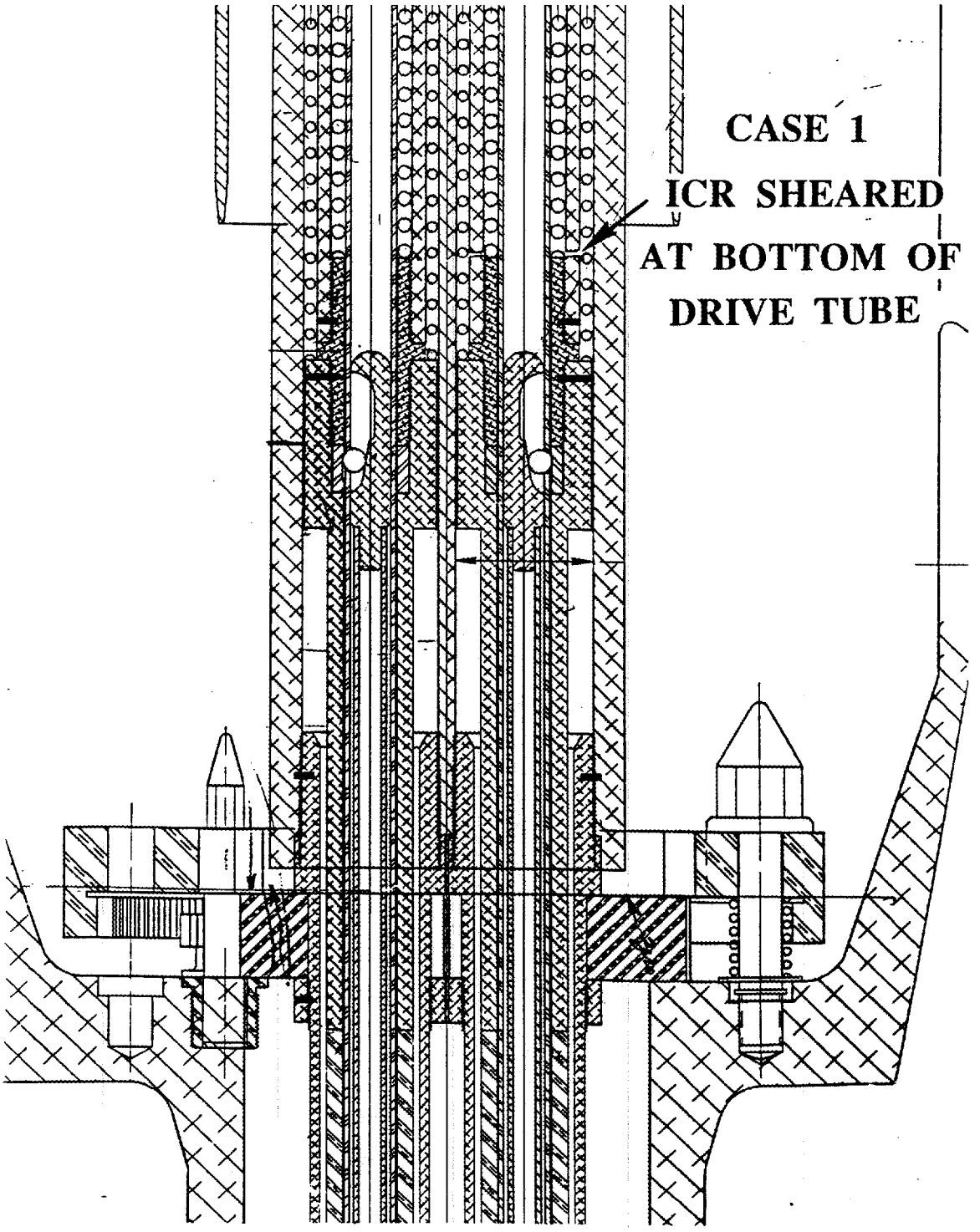


**Fig. 5.13. Inner control rod sheared at the bottom of the drive tube.**

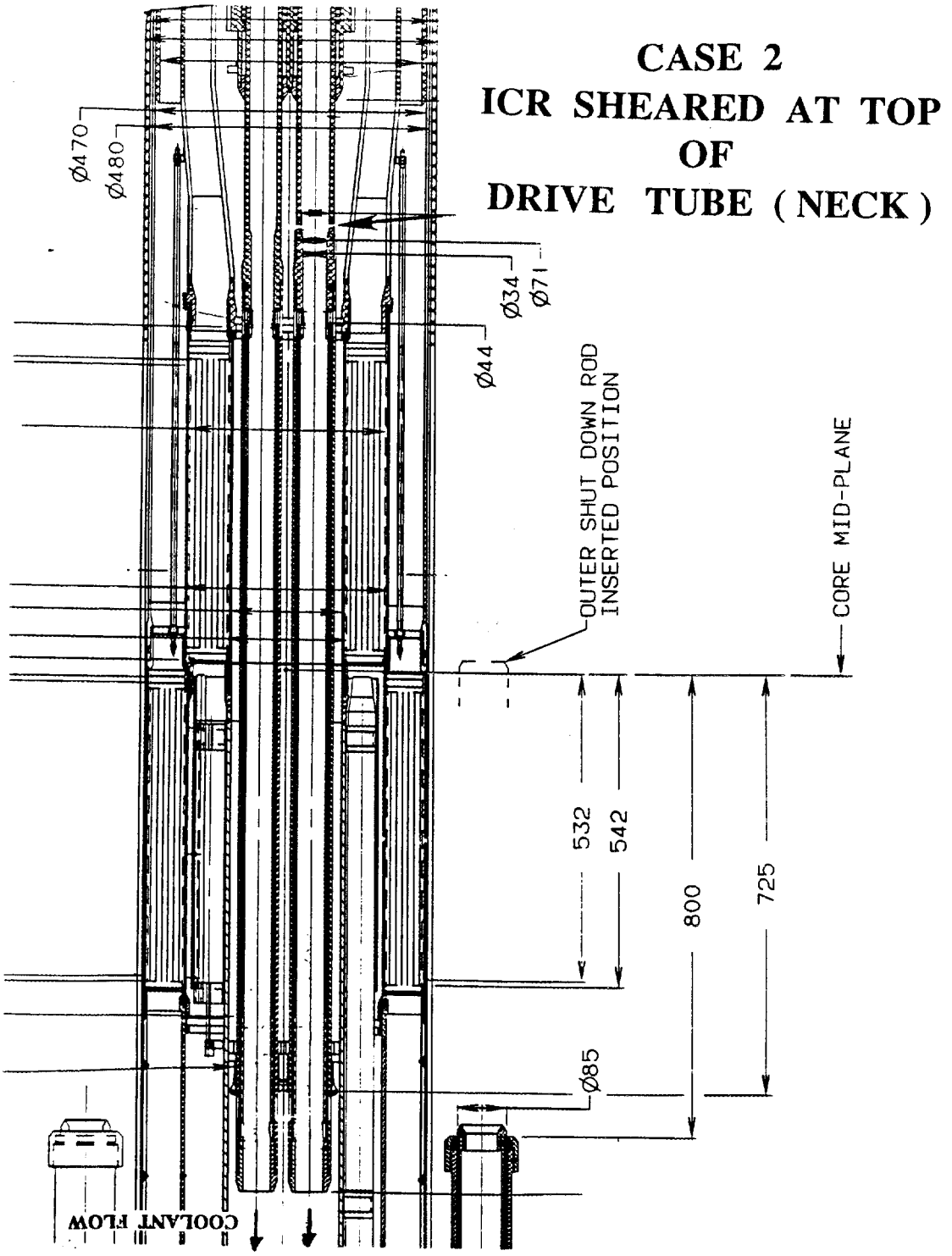


**Fig. 5.14. Inner control rod sheared at the top of the drive tube.**

**Case 1: Control rod sheared at the base of the guide tube (from the fully inserted position)**

| | |
|---|---|
| Shear forces: | |
| Inside channel | 33.3 |
| Annulus | 54.3 |
| Outside | 27.8 |
| Buoyancy forces | 74.8 |
| Other ΔP forces | 187.0 |
| TOTAL | 377.2 N / 319 N = 1.18 *g* |

The total forces for this case are slightly (18%) larger than the weight of the control rod. Therefore, the sheared control rod will move slowly upwards in the direction of the flow away from the core (the control rod is ejected). Because the control rod surface is in contact with the rollers at the top and with other solid parts at the bottom (springs, guide tube), a friction force against the control rod motion will prevent the control rod from moving fast. However, as the control rod is dragged upwards, a longer portion of the drive tube gets exposed to the coolant flow (as the drive tube comes out of the guide tube) resulting in increased shear forces. Consequently, as the control rod is dragged upwards, the lifting force increases.

**Case 2: Control rod sheared at the neck Inconel/guide tube**

The second case assumed that the control rod is sheared at the neck connecting the control rod to the drive tube. In this case, the total mass of the sheared control rod is 24 kg, with a weight of 235.2 N. This case is more complex to study because it results in flow redistribution. Before the control rod is sheared, the ΔP from the hypothetical point of shear to the control rod exit is 80.4 kPa outside the control rod (because of the roller plate ΔP) and only 12 kPa inside the control rod. It is assumed that the flow velocity is 6 m/s in the intact geometry, both inside and outside the control rod. After the control rod is sheared, a larger flow will go inside the control rod (because of the lower ΔP) until ΔPs outside and inside the control rod equalize. This also results in a smaller flow through the annulus (with a smaller ΔP) than before the control rod was sheared. Overall, the larger flow into the control rod results in larger shear forces. The resulting flow inside the control rod is 2.6 times the flow before the control rod sheared off. This high flow will take some time to be established. The following summarizes the calculation of lift forces for this case:

a. Calculation using the existing flows before flow redistribution occurs:

| | |
|---|---|
| Shear forces: | |
| Inside channel (at 6 m/s) | 19.2 |
| Annulus (at 6 m/s) | 54.3 |
| Outside (at 6 m/s) | 23.8 |
| Buoyancy forces | 40.8 |
| Other ΔP forces (using pressures before CR sheared) | 175.3 |
| TOTAL | 313.4 N / 235.2 N = 1.33 *g* |

Because the total forces for this case are 1.33 times the weight of the sheared control rod, they will lift and eject it.

b. Calculation using the high flow inside the control rod after flow redistribution:

| | |
|---|---|
| Shear forces: | |
| Inside channel (at 15.6 m/s) | 130.1 N |
| Annulus (at 5 m/s) | 40.7 N |
| Outside (at 6 m/s) | 23.8 N |
| Buoyancy forces | 40.8 N |
| Other ΔP forces | 188.5 N |
| TOTAL | 423.9 N / 235.2 N = 1.8 *g* |

Therefore, in this case, the lift forces start at 1.33 *g* and increase to 1.8 *g* after the flow redistribution occurs. The calculated forces for this case are significantly larger than for case 1.

Once this portion of the control rod (1.625 m long) starts moving upward, it may get off center and lodge against the walls of the central hole region or against the second set of rollers. If the sheared control rod keeps centered and moving, once it clears the first set of rollers, the ΔP across the length of the sheared control rod will decrease considerably, and the resulting forces will be less than its weight. Consequently, without lift forces, the sheared control rod will stop moving upward and will start moving downward (because of its weight) until it contacts the first set of rollers again.

### 5.2.6.2 Possible Solutions

Since ejection of a sheared control rod is an undesirable event, several solutions have been investigated. In principle, lift forces can be eliminated either by increasing the mass of the control rod or by reducing the total forces over the control rod.

Increasing the mass of the control rod may not be the best alternative because a larger mass has a negative impact on other design aspects (scram acceleration and deceleration, etc.). Since case 2 is more severe than case 1, solutions for case 2 have been investigated. To eliminate the lift for case 2, the mass of the control rod needs to be increased 1.8 times, keeping the total forces over the control rod constant. However, mass increases result in volume increases that also increase the buoyancy forces. Therefore, a total mass larger than 1.8 times the initial 24 kg will be required. It has been estimated that about 1.95 times the initial mass is required to equalize the weight to the total lift forces, including the increased buoyancy force. The total mass of the intact (unsheared) control rod will be 1.95 × 24 kg + 12.15 kg = 46.8 + 12.15 = 58.95 kg, about 63% more than the mass of the unmodified control rod (36.15 kg).

The second alternative to reduce the lift forces can be accomplished by reducing the ΔP through the control rod. This can be accomplished two different ways: by reducing the flow velocity or by opening narrow passages (like the annulus of the control rod). Reducing the flow velocity will reduce the shear forces and the ΔP forces (it will not affect the buoyancy forces). To solve the worst case (case 2b), the flow velocity under intact conditions needs to be reduced from 6 to only 4.27 m/s everywhere in the control rod (this low velocity may not be sufficient to cool the control rod of this design). With this reduced velocity, the total forces after the control rod is sheared are equal to the weight of the sheared control rod (without changing the mass). After the control rod is sheared, the velocity outside the control rod will remain the same (4.27 m/s), the velocity inside the hafnium will increase to 11.1 m/s, and the velocity inside the annulus will decrease to 3.7 m/s because of flow redistribution. Case 2b could also be resolved using a combination of different velocities at different points of the control rod. High velocities in some areas would be offset by low velocities in other areas.

Another possibility to eliminate the lift forces is to reduce the ΔP through the annulus between the hafnium and the Inconel. The current design yields a ΔP of 76.4 kPa through the annulus at a flow

velocity of 6 m/s. To compensate for this ΔP, the roller orifice plate requires a ΔP of 72.2 kPa. If the ΔP through the annulus were reduced by half to 38.2 kPa (this large reduction may be difficult to obtain) and the same flow velocities of 6 m/s were kept, the ΔP through the roller orifice plate would be reduced to 34 kPa. After the control rod sheared at the neck, the total forces would be 259 N (1.1 *g*), still slightly higher than the weight of the control rod. A larger ΔP reduction would be necessary to eliminate completely the lift forces without changing masses or velocities.

Imposing other downward forces (like a spring) at appropriate points could also eliminate lifting of the sheared control rod. Perhaps the best solution to eliminate this problem is a combination of several or all the affecting variables: opening the annulus passage, reducing flow velocities, imposing other downward forces, and increasing the control rod mass. This first design also has cooling problems at the junction of the aluminum and the Inconel. A revision of this design was deemed necessary.

## 5.3 SECOND DESIGN OF THE INNER CONTROL RODS

### 5.3.1 Geometry of the Second ICR Design

To solve the problems encountered with the previous design of the inner control rods, namely, thermal problems at the junction of the inconel and aluminum and coolant lift forces larger than the weight, a new design of the ICRs was developed. The new design uses different materials than the previous one to solve the thermal problem. The new design junction uses titanium and Zircaloy, both materials with higher maximum temperature limits than aluminum. The new materials result in a heavier control rod (~48.5 kg) than the previous design (~36.15 kg). This increase is beneficial with respect to lift forces because the heavier control rod can take larger lifting forces without being lifted. The new design uses titanium instead of Inconel for the control rod cladding, and Zircaloy instead of aluminum for the control rod drive tube. The neutron-absorbing material continues to be hafnium. There are 12 ribs in between the titanium cladding and the hafnium absorber in the annulus cooling channel (Fig. 5.15). These ribs are made of Zircaloy and are located only at the entrance and the exit of the annulus channel (Fig. 5.16). The flow area of the annulus channel is larger now (811.12 $mm^2$) than in the previous design (710.77 $mm^2$). This larger flow area will produce a lower pressure drop and smaller lift forces. However, the rib areas at the entrance and the exit of this annulus have a flow area of only 331 $mm^2$. These constrictions (and expansions) will yield significant pressure losses that will result in large lift forces. This effect is studied in detail in the present calculations. The remaining dimensions of the new ICR design are unchanged or slightly modified with respect to the previous design. Figure 5.17 shows the top of the ICRs with this design.

### 5.3.2 Lift Forces over a Sheared Control Rod

Since the worst case is that a control rod is sheared at the neck connecting the cladding to the drive tube (case 2 of Sect. 5.2.6), this case has been analyzed here.

The sheared control rod studied here has a total length of 1.597 m and a total mass of 21.197 kg. By comparison, the same case studied with the previous design was 1.625 m long with a mass of 24 kg. Therefore, the sheared control rod of the new design is lighter than in the previous design. Two different factors contributed to the mass difference. First, the sheared control rod of the new design is a little shorter than in the previous design because of the "neck" is now located a little (28 mm) higher than in the previous design. Second, this portion of the control rod is lighter because a lighter material, titanium, is used instead of Inconel for the cladding. The complete control rod of the new design is heavier because of the Zircaloy in the drive tube (which is not part of the sheared control rod) instead of aluminum as in the previous design.

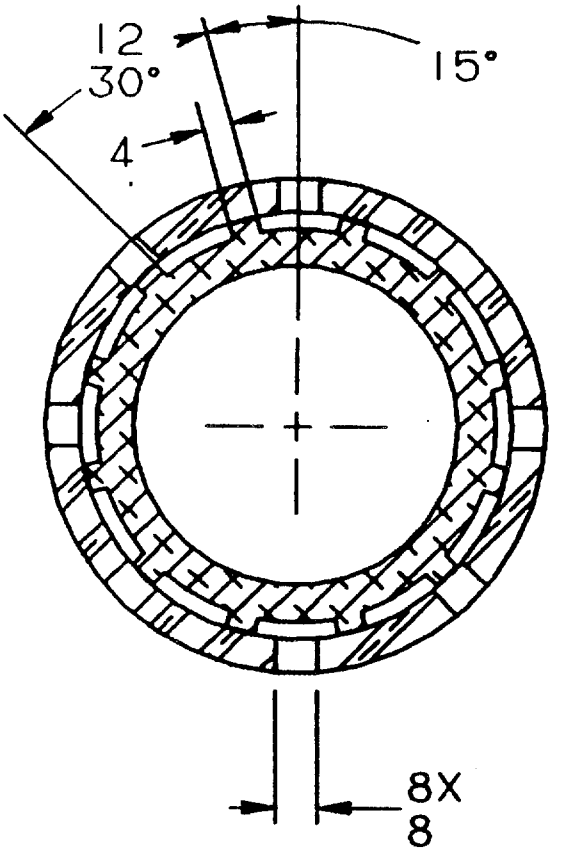


**Fig. 5.15. Ribs between the titanium cladding and the absorber (second design).**

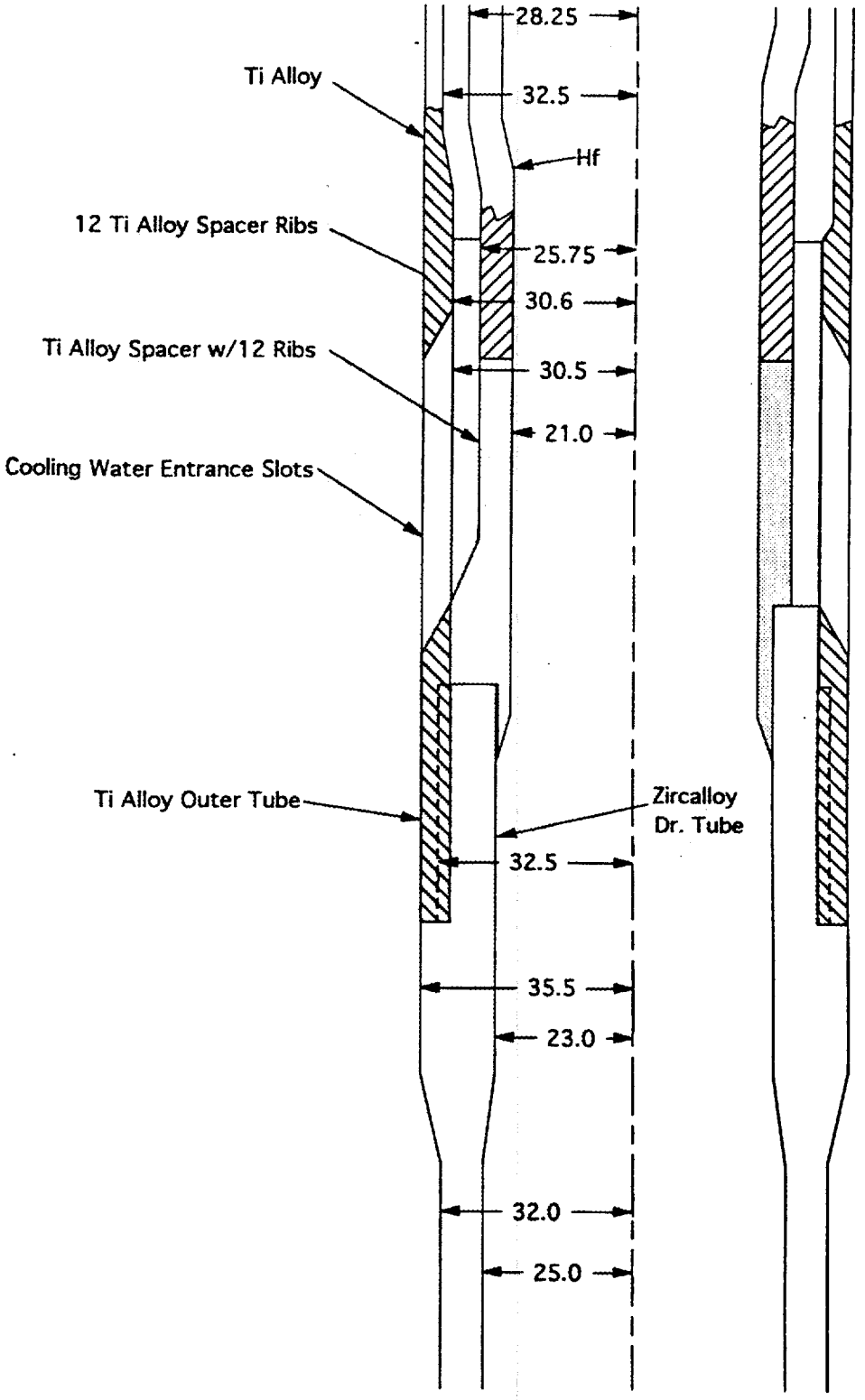


**Fig. 5.16. Titanium outer tube/Zircaloy drive tube with enlarged opening at ribs (second design).**

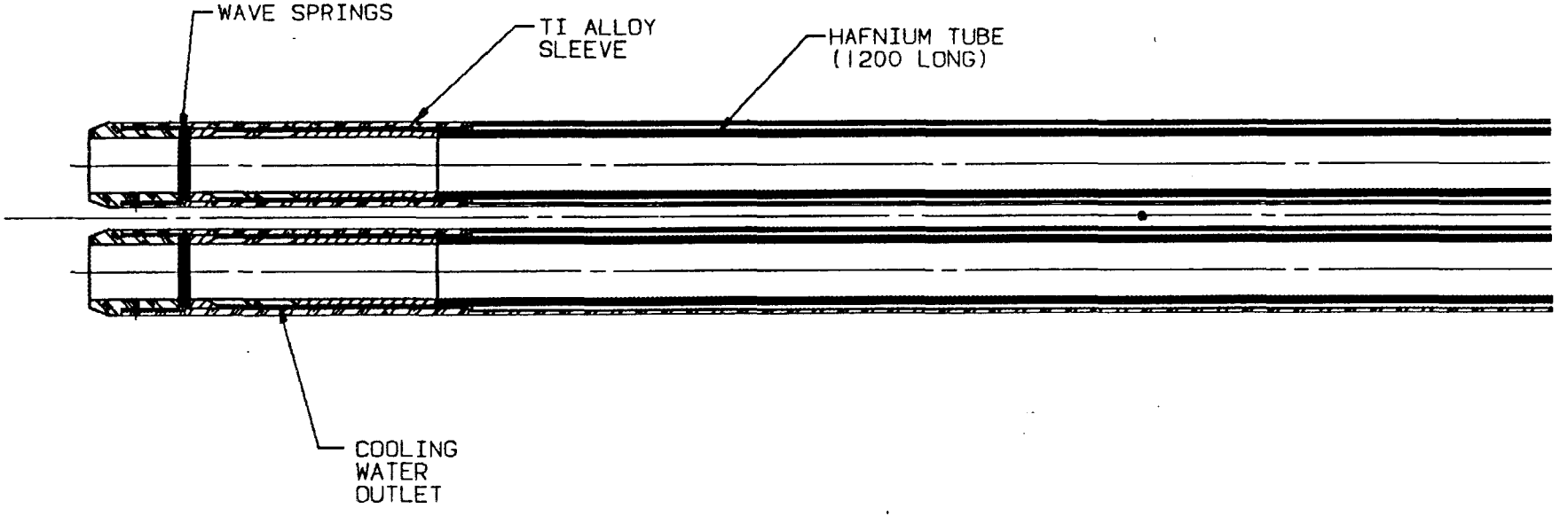


**Fig. 5.17. Top of the inner control rods (second design).**

Two different coolant velocities (4 and 6 m/s) were considered, but only the 4-m/s case was studied. This case resulted in very large lift forces (larger than the sheared control rod weight) and consequently, the 6-m/s case with even larger lift forces will be worse. It is believed that the new materials of the ICR can be cooled adequately with a coolant velocity of only 4 m/s. These velocities were assumed to be constant outside the cladding, inside the cladding/hafnium annulus portion without the ribs, and inside the hafnium cylinder. Outside these regions, the velocities will be different. For the 4-m/s case, the coolant velocity is 4.6 m/s before reaching the slots into the annulus, 9.8 m/s inside the ribbed portions of the annulus, and 6 m/s inside the control rod, after mixing with the flow inside the hafnium cylinder. After leaving the control rod, the coolant flow velocity is only 3.37 m/s.

For the 6-m/s case, the coolant velocities are, before entering the annulus slots, 6.9 m/s; in the annulus ribs, 14.7 m/s; inside the control rod, 8.9 m/s; and after leaving the control rod, 5.1 m/s. The velocity inside the ribbed portion of the annulus is more than twice the velocity in the open portion of the annulus.

For the 4-m/s case, the pressure drops before flow redistribution occurs are as follows:

| | |
|---|---|
| $\Delta P$ annulus friction: | |
| Open area at a 4 m/s | 23.6 |
| Friction, ribbed area at 9.8 m/s | 14.2 |
| Form losses (contractions and expansions) | 60.7 |
| $\Delta P$ annulus, TOTAL | 98.5 kPa |
| | |
| $\Delta P$ inside control rod: | |
| Friction at 4 m/s | 3.9 |
| Friction at 6 m/s | 1.1 |
| $\Delta P$ inside control rod, TOTAL | 5.0 kPa |
| | |
| $\Delta P$ outside control rod: | |
| Friction at 4 m/s | 3.4 |
| Friction at 4.6 m/s | 0.4 |
| $\Delta P$ outside control rod, total friction | 3.8 |
| $\Delta P$ rollers: 98.5 + 1.1 – 3.4 | 96.2 |
| $\Delta P$ outside control rod, TOTAL | 100.0 kPa |

These calculations indicate that the form losses in the annulus are almost twice the friction losses. This large $\Delta P$ in the annulus needs a large $\Delta P$ through the rollers outside the control rods.

After the control rod is sheared off, flow redistribution occurs. It is assumed that the flow outside the control rod remains unchanged, with a total $\Delta P$ of 100.0 kPa. The flow inside the control rod will increase considerably in order to equalize the $\Delta P$ inside (which was only 5.0 kPa) to the 100.0 kPa outside. Therefore, the pressure drops after flow redistribution are as follows:

| | |
|---|---|
| $\Delta P$ outside control rod (unchanged) | 100.0 |
| | |
| $\Delta P$ inside control rod: | |
| Region at 17 m/s | 77.2 |
| Region at 18.2 m/s | 22.8 |
| $\Delta P$ inside control rod, TOTAL | 100.0 kPa |

| | |
|---|---|
| ΔP annulus | |
| Friction open area at 2.4 m/s | 18.5 |
| Friction ribbed area at 6.0 m/s | 11.1 |
| Form losses | 47.6 |
| ΔP annulus, TOTAL | 77.2 kPa |

After flow redistribution, the velocity inside the control rod increases from 4 to 17 m/s, and inside the annulus (open area) decreases from 4 to 2.4 m/s. Form losses at the entrance and at the exit of the control rod were not considered. With form losses, the resulting velocities inside the control rod will be less than the values calculated here.

The total lift forces over the control rod are:

| | |
|---|---|
| Shear forces: | |
| Outside | 11.0 |
| Annulus | 18.7 |
| Inside (conservative value, without form losses) | 166.2 |
| Buoyancy forces | 28.1 |
| Other ΔP forces | 229.7 |
| TOTAL | 453.7 N = 2.18 *g* |

The weight of the sheared control rod (with a mass of 21.197 kg) is 207.7 N. Therefore, the lift forces are 2.18 times the weight of the control rod.

The new design of the control rods result in larger lift forces than the previous design, primarily because of the large ΔP form losses through the contractions and expansions of the annulus. The ribbed area has an open flow area of only 331 $mm^2$, with the rest of the annulus open flow area of 811 $mm^2$, about 2.45 times larger. These large flow area changes need to be eliminated. Otherwise, coolant velocities inside the annulus need to be significantly reduced to reduce the lift forces to values below the weight of the control rod.

### 5.3.3 Recommended Design Changes for the Annulus of the Second Design of the Inner Control Rods to Avoid Lifting

Lift forces acting on a sheared inner control rod of the second design (titanium-Zircaloy with constrictions in the annulus) were calculated in Sect. 5.3.2. The sheared control rod is 1.597 m long with a mass of 21.197 kg (weight of 207.7 N) and results in lift forces equivalent to 2.18 *g* for a coolant velocity of 4 m/s.

If the annulus in the new control rod design is not modified, lifting of a rod sheared at the neck can be eliminated if the total ΔP through the annulus is reduced to about 43 kPa. This low ΔP requires a velocity through the open area of the annulus (unribbed) of only 2.64 m/s. The velocity through the ribbed portion of the annulus is 6.5 m/s. The velocities outside the cladding and inside the hafnium remain at 4 m/s. It should be noted that when the ΔP through the annulus is reduced, the ΔP through the rollers needs to be reduced also. Otherwise, a velocity smaller than the desired 4 m/s will result at other points of the control rods. Consequently, changes in the ΔP through the annulus result in changes in the ΔP through the rollers.

If the velocity inside the annulus must be maintained at 4 m/s because of thermal limitations, the design of the annulus needs to be modified to eliminate lifting of the control rod. For a coolant velocity of 4 m/s in the three cooling channels, lift forces over the sheared control rod are equal to its weight if the pressure drop inside the annulus is 45 kPa with a *constant* annulus open area of 700 $mm^2$

(i.e., no contractions or expansions). Pressure drops smaller than 45 kPa will result in lower lifting forces. The total length of the annulus is 1499 mm.

Several design solutions for these conditions can be found. The condition of

$$\Delta P \text{ annulus} = f\,(L/D_H)\,(v^2\,\rho)/2 \leq 45 \text{ kPa} \tag{9}$$

with $L$ = 1499 mm, $v$ = 4 m/s, $\rho$ = 1098 kg/m$^3$, results in

$$f/D_H \leq 0.004272 \quad . \tag{10}$$

Since f is a function of the Reynolds number,

$$Re = D_H\,\rho v/\mu = 6231\,D_H \quad , \tag{11}$$

Eqs. (10) and (11) can be solved simultaneously for

$$D_H \geq 5.5 \text{ mm} \quad . \tag{12}$$

The $\Delta P$ through the rollers needs to be calculated for each case to balance $\Delta P$s through the annulus and outside the control rods. The $\Delta P$ through the rollers is given by the following equation:

$$\Delta P \text{ rollers} = \Delta P \text{ annulus} + \Delta P \text{ inside the ICR after the annulus} - \Delta P \text{ outside after the annulus.} \tag{13}$$

Therefore, using an annulus open flow area of 700 mm$^2$ and a coolant velocity of 4 m/s, lifting of the sheared control can be avoided for $D_H \geq 5.5$ mm. Using the new design inner and outer diameters of the annulus of 56.5 and 65 mm, respectively, a flow area of 700 mm$^2$ can be obtained with four ribs along the complete length of the annulus, each rib 6 mm wide at the base, equivalent to an angle of 12.33°. The resulting $D_H$ is 7.7 mm, larger than the value of 5.5 mm of Eq. (12).

Another alternative is to use six ribs, each 4 mm wide at the base, equivalent to an angle of 8.22°. This alternative results in $D_H$ = 7.36 and will also result in lift forces less than the weight of the rod.

Another possibility is to use eight ribs, each 4 mm wide at the base, equivalent to an angle of 8.22°. The resulting flow area is 663 mm$^2$ and $D_H$ = 6.98. Figure 5.18 shows these ribs in the annulus. This is the third design of the ICRs.

## 5.4 CALCULATIONS FOR THE THIRD DESIGN OF THE INNER CONTROL RODS

### 5.4.1 Lift Forces over the ICRs of the Third Design

Detailed calculations were performed for the last alternative considered in Sect. 5.3.3 using eight ribs, the third design of the ICRs. The other two cases also discussed, with four ribs, $D_H$ = 7.7, and six ribs, $D_H$ = 7.36 mm, should provide lower lift forces than this case.

The total $\Delta P$ through the annulus of the third design with eight ribs is 31.693 kPa (less than 45 kPa) for a coolant velocity of 4 m/s. The pressure drops before flow redistribution occurs are as follows:

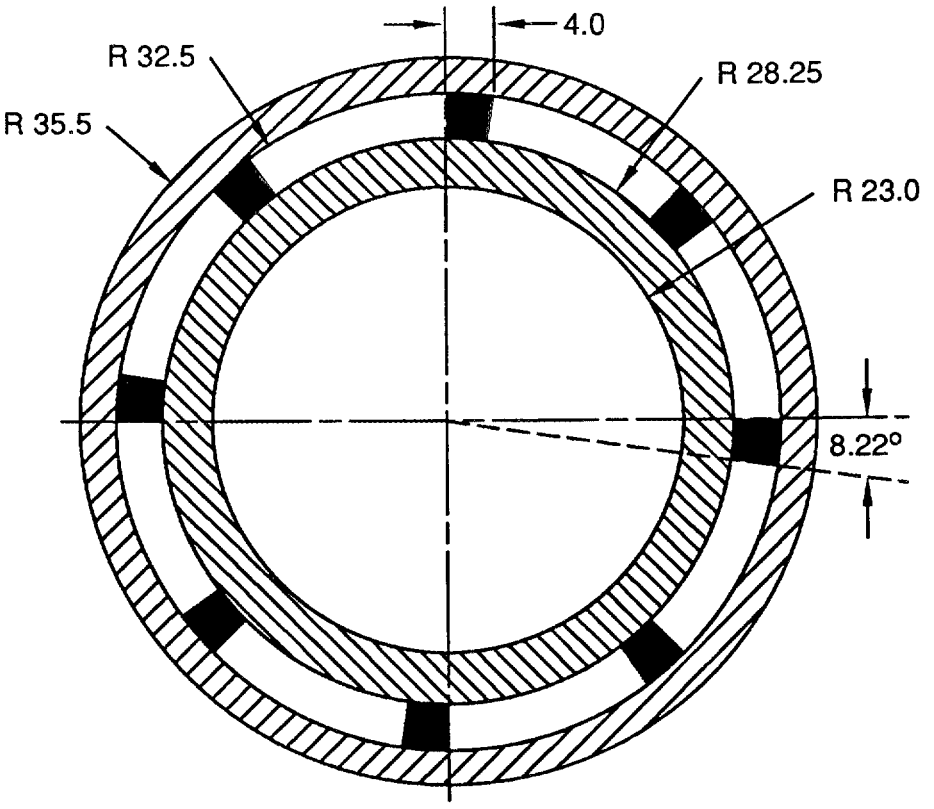


**Fig. 5.18. Eight-rib design (third design).**

| | |
|---|---|
| ΔP annulus at 4 m/s | 31.7 kPa |
| ΔP inside control rod: | |
| At 4 m/s | 3.9 |
| At 5.596 m/s (top) | 1.0 |
| | 4.9 kPa |
| ΔP outside control rod: | |
| At 4.5 m/s (before annulus) | 0.3 |
| At 4 m/s | 3.4 |
| Rollers = 31.7 + 1.0 – 3.4 = | 29.3 |
| TOTAL | 33.0 kPa |

After flow redistribution, the pressure drops are as follows:

| | |
|---|---|
| ΔP annulus at 3.93 m/s | 30.5 kPa |
| ΔP inside control rod: | |
| Entrance | 5.9 |
| Flow at 6.8 m/s | 10.3 |
| Flow at 8.4 m/s | 2.2 |
| Exit | 14.6 |
| TOTAL | 33.0 kPa |
| ΔP outside control rod | 33.0 kPa (unchanged) |

The total lift forces are as follows:

| | |
|---|---|
| Shear forces: | |
| Annulus | 20.2 |
| Inside control rod | 20.8 |
| Outside control rod | 11.0 |
| Buoyancy forces | 28.1 |
| Other ΔP forces | 75.9 |
| TOTAL | 156.0 N / 207.7 N = 0.75 *g* |

The total lift forces are only 75% the weight of the sheared control rod.

Because the lifting forces over the control rod sheared at the neck resulted in the worst case of past analyses, it is expected that other cases (control rod sheared at the base of the drive tube or intact control rod) will result in lifting forces that are even lower percentages of the weight than the value calculated here for the worst case.

### 5.4.2 Flow and Pressure Drops Through the Locking Guide Pin Inside the Inner Control Rods

The new third design of the ICRs (Sect 5.3.3) provides open flow areas between the locking guide pin and the disconnect and between the disconnect and the drive tube. These flow areas are shown in Fig. 5.19. The coolant flowing through these areas will cool the locking guide pin and the disconnect as well as the inside of the drive tube and the neutron-absorbing material (hafnium). The coolant will enter this region from outside the guide tube through holes in the walls of the guide tube, drive tube, and drive shaft (Fig. 5.20). The purpose of this calculation is to evaluate the flow that these open flow areas allow into the control rod.

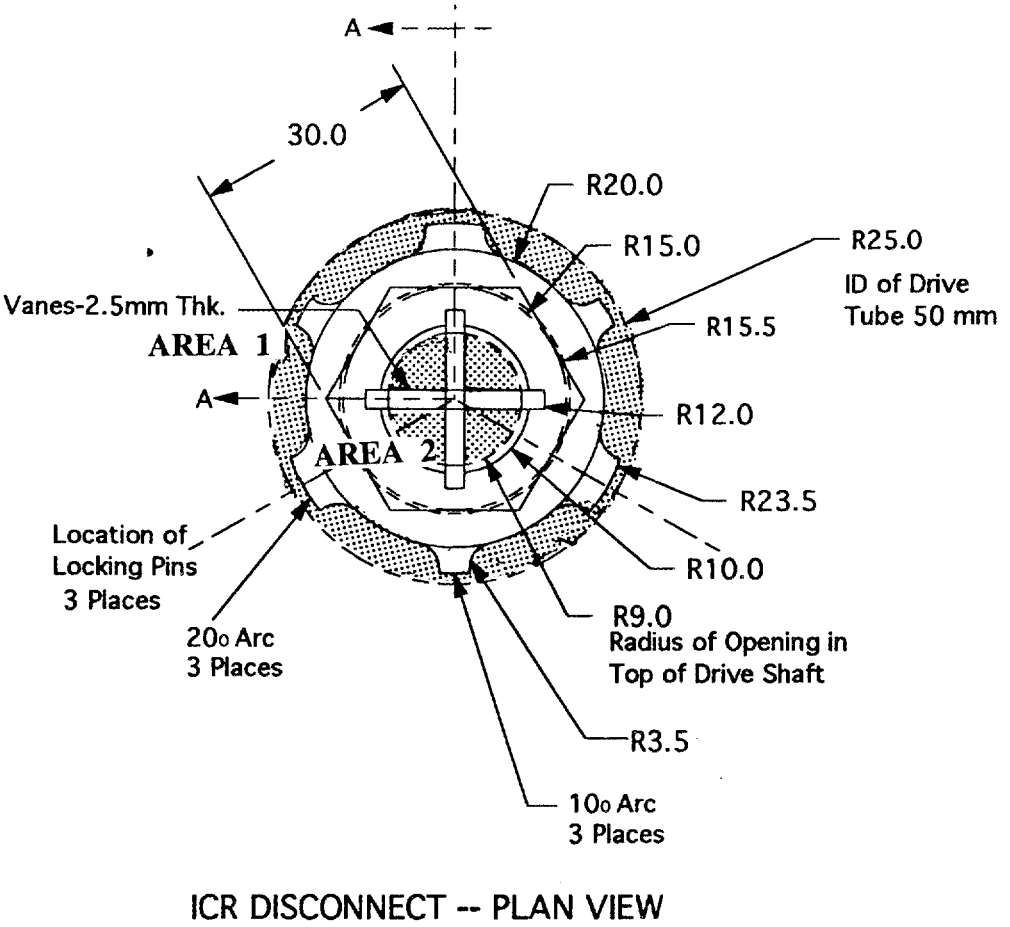


**Fig. 5.19. Flow areas through the disconnect mechanism (third design).**

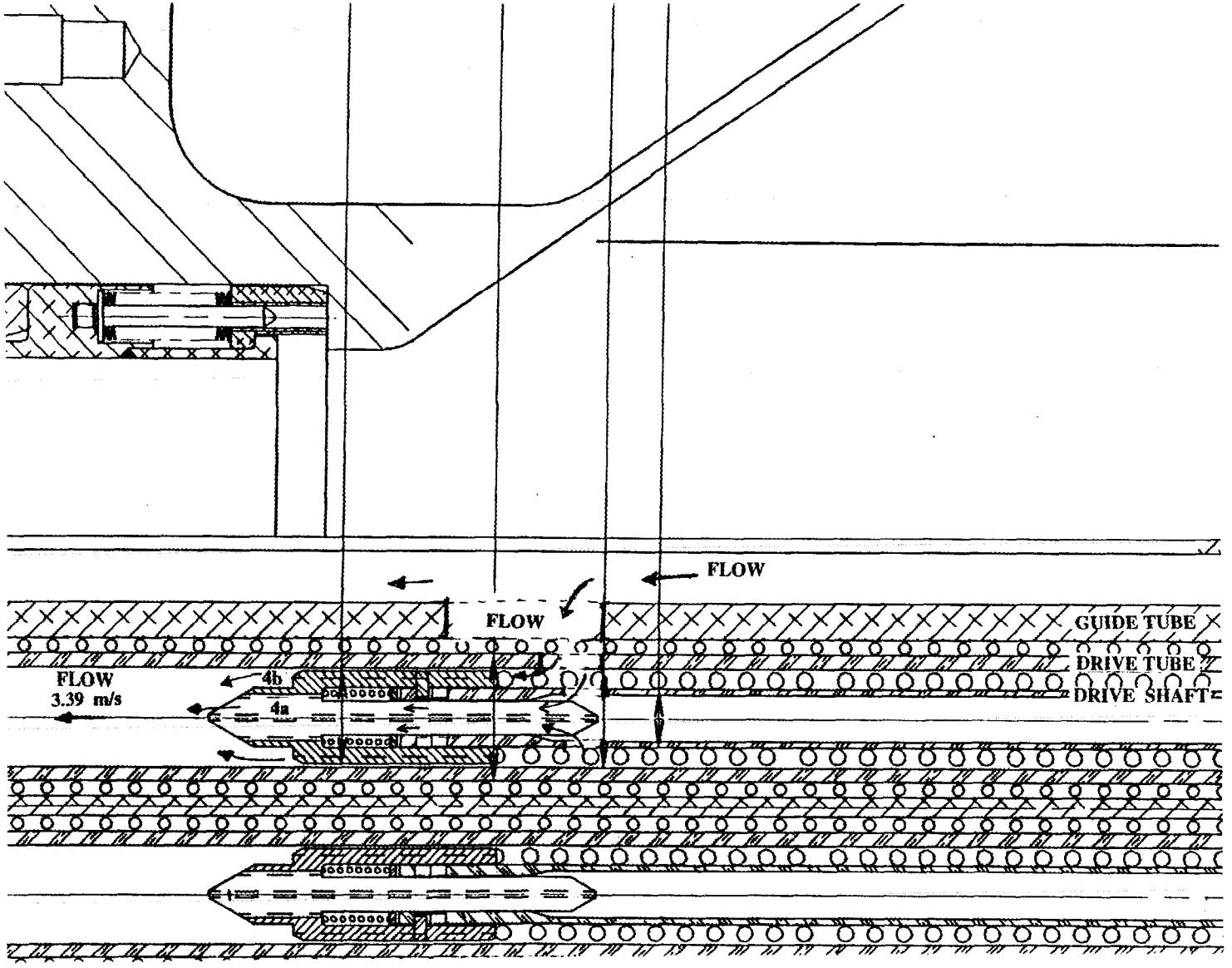


Fig. 5.20. Flow into the inner control rods and entrance orifices through guide tube, drive tube, and drive shaft (third design).

Pressure drops have been estimated for a coolant flow velocity of 4 m/s inside the hafnium (which has an inside diameter of 46 mm, equivalent to an open flow area of 1661.9 $mm^2$). This velocity corresponds to a volumetric flow rate of $6.65 \times 10^{-3}$ $m^3/s$, or a mass flow rate of 7.3 kg/s using a density of the heavy water of 1098 $kg/m^3$ at 45°C. A velocity of 4 m/s was also used to calculate the pressure drop outside the control rods. The pressure drop outside the control rods is strongly dependent on the ΔP through the rollers, which in turn is dependent on the ΔP through the cladding/hafnium annulus. Comparing the ΔP through the inside of the control rods with the ΔP outside determines the flow that can go inside the control rod. If the ΔP inside the control rod is smaller than the ΔP outside, a larger flow than the one used in calculating the ΔP can go inside the control rod. On the other hand, if the ΔP inside is larger than the ΔP outside, a smaller flow will go into the control rod.

The open flow area between the disconnect and the guide tube has been calculated to be 458.14 $mm^2$. The open flow area between the disconnect and the locking guide pin has been calculated to be 170.72 $mm^2$ (Fig. 5.19). The total combined flow area that allows coolant into the control rod is therefore 628.86 $mm^2$. This small area requires a coolant velocity of 10.57 m/s in order to supply coolant at 4 m/s velocity inside the hafnium portion of the control rod.

Given the complexity of the geometry and the flow patterns through this region, simplifications were used to calculate pressure drops. Table 5.3 summarizes these calculations.

**Table 5.3. Calculated pressure drops in the inner control rods**

| Inside portion of control rod | Velocity (m/s) | Area ($mm^2$) | Diameter (mm) | Length (mm) | ΔP (kPa) |
|---|---|---|---|---|---|
| 1. Exit after annulus (top) | 5.6 | 1662 | 46 | 200 | 1.0 |
| 2. Inside hafnium | 4 | 1662 | 46 | 1400 | 3.9 |
| 3. Inside drive tube | 3.4 | 1964 | 50 | 2610 | 4.9 |
| 4a. Inside disconnect | 5.8 | 170.7 | 5.32 | 193 | 30.5 |
| 4b. Outside disconnect | 12.7 | 458.1 | 5.5 | 105 | 30.5 |
| 5. Entrance and orifices (estimated) | <10.6 | >628.9 | | | ~30.0 |
| TOTAL ΔP | | | | | 70.3 |

These calculations indicate that the total ΔP from the entrance into the guide tube orifices to the exit of the control rod is 70.3 kPa. Paths 4a and 4b are parallel, with both flows discharging inside the drive tube (Fig. 5.20), and only one path ΔP needs to be added in Table 5.3. To allow the flow to enter into the drive tube, holes or slits need to be perforated through the walls of the guide tube, the drive tube, and the drive shaft (Fig. 5.20). For the drive shaft with a 3-mm-thick wall, a possibility is to perforate three slits 3 mm wide and 19.61 mm long. These three slits have a combined flow area of 170.7 $mm^2$, the same flow area as inside the disconnect. Other options that provide the same flow area are also acceptable. The structural effect of these slits or orifices must be evaluated.

For the drive tube with a 7-mm-thick wall, a possibility is to perforate three slits 6 mm wide and 36 mm long. These three slits have a combined flow area of 628.9 $mm^2$, required to supply coolant flow inside the drive tube at a velocity of 10.6 m/s. Other possibilities providing the same or larger flow areas are also acceptable. The structural effect of these slits also needs to be evaluated.

Finally, perforations are also required through the 18-mm-thick wall of the guide tube. These perforations are required to supply coolant inside the drive tube and to allow coolant to enter and exit the volume between the guide tube and the drive tube during the first 600 mm of travel of the control

rods after being scrammed from the fully withdrawn position. The last 600 mm of travel do not have perforations to provide a dampening effect to the control rod motion. The perforations through the guide tubes should allow at least 628.9 $mm^2$ of flow area. Since perforations are required along half of the guide tube length to allow free exit and entry of coolant during a scram, the flow area of these perforations will be considerably larger than the minimum required. The flow area of 628.9 $mm^2$ can be achieved with only one slit 8 mm wide and 80.32 mm long. Several slits along the guide tube are needed to allow free fluid circulation during a scram. Given the thickness of this wall (18 mm), no structural problems are expected from these perforations.

Table 5.4 shows the calculation of the total pressure drop outside of the control rod.

**Table 5.4. Calculated pressure drops outside the control rod**

| Outside portion of control rod | Velocity (m/s) | Area ($mm^2$) | Diameter (mm) | Length (mm) | ΔP (kPa) |
|---|---|---|---|---|---|
| 1. Bottom | 4.1 | 18,702 | 62.335 | 2,845 | 4.5 |
| 2. Neck at annulus entrance | 4.6 | 16,475 | 52.05 | 110 | 0.4 |
| 3. Top after annulus entrance | 4.0 | 16,475 | 52.05 | 1,447 | 3.4 |
| 4. Rollers (desirable ΔP) | | | | | <43.0 |
| TOTAL ΔP | | | | | 51.3 |

The ΔP through the rollers used in this calculation (43 kPa) is the desirable value required to avoid a sheared control rod being lifted by the coolant flow (Sect. 5.3.3). However, it has been calculated that the pressure drop through the rollers of the second design of the control rod needs to be about 96.2 kPa (Sect. 5.3.2). If this larger value is used, the total ΔP outside the control rods will be 104.5 kPa, larger than the ΔP estimated through inside the control rods (70.3 kPa). Consequently, because both pressures need to be equal, the inside pressure will increase to 104.5 kPa by allowing a larger flow (with a velocity larger than 4 m/s inside the hafnium) through the control rod. If the desirable ΔP through the rollers (43 kPa) is used the total ΔP outside the control rod is 51.3 kPa, a value smaller than the estimated ΔP inside the control rods (70.3 kPa), but not very different. The ΔP inside the control rods will be equal to the ΔP outside the control rods if a velocity of ~3.45 m/s instead of 4 m/s is used inside the hafnium. The 3.45-m/s velocity may be sufficient to cool the inside of the control rods. Therefore, based on these results, it appears that the new design of the inner control rods can provide sufficient coolant flow inside the control rods even if a ΔP through the rollers of only 43 kPa is used. Higher ΔP through the rollers will result in higher velocities inside the control rods.

Given the uncertainties in the calculation of the ΔP inside the control rods (i.e., the complexity of the flow passages and the lack of final definition of the flow orifices through the walls and of the design of the cladding/hafnium annulus), these results may have significant errors. A more detailed calculation is recommended once the geometry of the control rods is completely defined (including the perforations and the annulus) and the minimum flow coolant requirements are calculated.

## 6. REFERENCES


1. G. L. Yoder et al., *Steady-State Thermal-Hydraulic Design Analysis of the Advanced Neutron Source Reactor*, ORNL/TM-12398, Martin Marietta Energy Systems, Inc., Oak Ridge Natl. Lab., May 1994.

2. M. S. Siman-Tov et al., *Thermal Hydraulic Correlations and Experimental Database for the Advanced Neutron Source Reactor—Closing Report,* ORNL/TM-13081, Lockheed Martin Energy Systems, Inc., Oak Ridge Natl. Lab., August 1995.

3. G. E. Giles, *Advanced Neutron Source Reactor Thermal Analysis of Fuel Plate Defects,* ORNL/TM-13072, Lockheed Martin Energy Systems, Inc., Oak Ridge Natl. Lab., August 1995.

4. P. E. Blumenfeld, *Fuel Loading and Homogeneity Analysis of HFIR Fuel Plates Loaded with Uranium Silicide Fuel,* ORNL/TM-13066, Lockheed Martin Energy Systems, Inc., Oak Ridge Natl. Lab., August 1995.

5. M. Siman-Tov et al.,"Thermal Hydraulic Correlations for the Advanced Neutron Source Reactor Fuel Element Design and Analysis," pp. 63–78 in *Nuclear Reactor Thermal-Hydraulics,* ed Y. A. Hassan and L. E. Hochreiter, American Society of Mechanical Engineers, New York, 1991.

6. F. J. Peretz et al., *Conceptual Design Summary*, ORNL/TM-12184, Martin Marietta Energy Systems, Inc., Oak Ridge Natl. Lab., September 1992.

7. G. L. Hofman, "Some Recent Observations on the Radiation Behavior of Uranium Silicide Dispersion Fuel," *Proceedings of the 1988 International Meeting on Reduced Enrichment for Research Reactors,* ANL/RERTR/TM-13 CONF-8809221, Argonne National Laboratory, Chicago, September 1988.

8. R. E. Pawel et al., "The Corrosion of 6061 Aluminum under Heat Transfer Conditions in the ANS Corrosion Test Loop," *Oxid. Metals* **36**(1/2), 175 (1991).

9. D. P. Bozarth, Science Applications International Corp., memorandum to D. L. Selby, Martin Marietta Energy Systems, Inc., "Transmittal of SAMPLE Code and Initial Results for ANS Statistical Thermal-Hydraulic Analysis," July 10, 1991.

10. D. G. Morris et al., *Description of TASHA: Thermal Analysis of Steady-State Heat Transfer for ANS,* ORNL/TM-13082, Lockheed Martin Energy Systems, Inc., Oak Ridge Natl. Lab., September 1995.

11. Irwin Miller and John E. Freund, *Probability and Statistics for Engineers,* 2d ed., Prentice-Hall, Inc., Englewood, N. J., 1977, pp. 36–40.

12. *Monthly Progress Report for January 1992,* Attachment 2, ORNL/ANS/INT-5/V46, Martin Marietta Energy Systems, Inc., Oak Ridge Natl. Lab., February 1992.

13. *Monthly Progress Report for February 1993,* Attachment 2, ORNL/ANS/INT-5/V59, Martin Marietta Energy Systems, Inc., Oak Ridge Natl. Lab., March 1993.

14. C. A. Wemple, *Detailed Heat Load Calculations for the Conceptual Design of the Advanced Neutron Source Reactor,* ORNL/M-3207, Martin Marietta Energy Systems, Inc., Oak Ridge Natl. Lab., December 1993.

15. Frank Kreith, *Principles of Heat Transfer,* 3d ed., Intex Educational Publishers, New York, 1973.

16. F. W. Dittus and L. M. K. Boelter, *University of California (Berkeley) Publications in Engineering,* Vol. 2, 1930, p. 443.

17. *Monthly Progress Report for March 1993,* Attachment 2, ORNL/ANS/INT-5/V60, Martin Marietta Energy Systems, Inc., Oak Ridge Natl. Lab., April 1993.

18. *Advanced Continuous Simulation Language (ACSL) Reference Manual,* Ed. 10.0, Mitchell and Gauthier Associates, Inc., Concord, Mass., 1991.

## INTERNAL DISTRIBUTION

1. B. R. Appleton
2–6. J. H. Campbell
7–11. J. J. Carbajo
12. N. C. J. Chen
13. D. Cook
14. J. A. Crabtree
15. W. G. Craddick
16. J. R. Dixon
17. G. Farquharson
18. D. K. Felde
19. R. M. Harrington
20. R. L. Johnson
21. J. A. March-Leuba
22. M. T. McFee
23–27. D. G. Morris
28. W. R. Nelson
29. J. E. Park
30. R. E. Rothrock
31. D. L. Selby
32. M. Siman-Tov
33. T. K. Stovall
34. R. P. Talyarkhan
35. M. W. Wendel
36. C. D. West
37–41. G. L. Yoder
42. ORNL Patent Office
43–44. Central Research Library, Document Reference Section
45. Y-12 Technical Library
46–47. Laboratory Records Dept.
48. Laboratory Records, RC

## EXTERNAL DISTRIBUTIION

49. J. L. McDuffie, 521 Morrell Rd., Apt E66, Knoxville, TN 37919
50. A. E. Ruggles, University of Tennessee, College of Engineering, Pasqua Nuclear Engineering Building, Knoxville, TN 37966
51. U.S. Department of Energy, ANS Project Office, Oak Ridge Operations Office, FEDC, MS-8218, P.O. Box 2009, Oak Ridge, TN 37831-8218
52–53. Office of Scientific and Technical Information, P.O. Box 63, Oak Ridge, TN 37831